Novel III-Nitride Semiconductors for Solar Hydrogen Production

Jonathan Benton

The University of Sheffield

Department of Electronic and Electrical Engineering

Department of Chemistry

III-V Nitrides Group

Supervisors: Professor Tao Wang and Dr Julia Weinstein

A Thesis submitted for the degree of Doctor of Philosophy

Abstract

III-nitride materials are crucially becoming the most important and promising class of semiconductors for future optoelectronic devices including solid state lighting and solar energy applications. Presently, there are still many challenges in regards to the wide scale uptake of these devices, including low efficiencies and short lifetimes. Despite the ideal properties of InGaN for water splitting, there are still very few reports utilising these semiconductors.

This thesis investigates GaN and InGaN based structures for water splitting. Initially focussing on the fabrication of nanorods via the use of a self-organised nickel mask, where diameter and height of the structures have been optimised. As a result, the surface area of the device increases dramatically leading to an enhancement in photocurrent compared to as-grown planar devices. Alongside this, the fabricated nanostructures allow for an enhancement in electron-hole separation and an increase in the hydrogen generation rate.

The lifetime of the fabricated devices is also discussed. Prolonged exposure of the nanostructured devices results in the degradation and etching of the InGaN material. The addition of a secondary semiconductor material, NiO, acts as a reaction site for photogenerated holes preventing the oxidation and dissolution of InGaN devices in the experimental electrolytes, increasing the device lifetime.

Furthermore, a photoelectrochemical etch technique is implemented to create a porous device structure. The nanoporous network in the structure shortens the required diffusion length of the photogenerated carriers to values close to that of InGaN. An enhancement in photocurrent and hydrogen production has been observed due to the nanoporous structure.

Acknowledgements

I am grateful to a number of people who have provided their support and wisdom throughout the course of this thesis. Firstly my supervisor Professor Tao Wang has been invaluable in his guidance and his expertise. The faith he has had in me personally and the opportunities that I have obtained while under his supervision has helped to shape me into the person I have become. My thanks are also extended to my second supervisor Doctor Julia Weinstein for her interest and encouragement in the progress of my research.

The members of the Sheffield Nitride group both past and present have provided me both with their insights and friendship. My initial thanks go to Doctor Qi Wang and Doctor Jie Bai who trained me in device characterisation and fabrication, effectively allowing this thesis to be possible. Doctor Yipin Gong, Kun Xing, Xiang Yu and Benbo Xu grew samples for this work and performed growth characterisation. Doctor Paul Renwick, Doctor Rick Smith and Modestos Athanasiou have been invaluable office companions providing discussion across a range of subjects, aiding in the development of this work as well as creating an enjoyable working environment. The technical support of Paul Haines and the other members of the technical team have allowed a minimum level of disruption through their skill in the maintenance of equipment.

My friends and family have been a great support over the past 4 years, keeping me motivated and focused. A particular mention goes to my partner Matt without whom life would be a very boring place.

Thank you all for sticking with me in my pursuits.

Publication List

(1) J. Benton, J. Bai & T. Wang

"Utilisation of GaN and InGaN/GaN with Nanoporous Structures for Water Splitting"

Applied Physics Letters, **105**, 223902 (2014)

(2) J. Benton, J. Bai & T. Wang

"Nanoporous GaN for enhanced solar hydrogen production"

Solar Hydrogen and Nanotechnology IX, *SPIE Proceedings*, 91760K, (2014)

(3) J. Benton, J. Bai & T. Wang

"Significantly enhanced performance of an InGaN/GaN nanostructure based photo-electrode for solar power hydrogen generation"

Applied Physics Letters, **103**, 133904 (2013)

(4) J. Benton, J. Bai & T. Wang

"Enhancement in hydrogen generation efficiency using a GaN nanostructure"

Applied Physics Letters, **102**, 173905, (2013)

(5) J. Benton, J. Bai & T. Wang

"Nanoporous GaN for enhanced solar hydrogen production"

Solar Hydrogen and Nanotechnology IX, SPIE Optics & Photonics 2014, *San Diego, United States,* 17th – 21st August 2014 – Oral presentation

(6) J. Benton, J. Bai & T. Wang

"Porous GaN for solar hydrogen production"

UKNC Bristol 2014, Bristol, United Kingdom, 7-8th January 2014 – Oral presentation

(7) J. Benton, J. Bai & T. Wang

"Reduced photoelectrochemical etching of GaN/InGaN structure for solar hydrogen production"

UKNC Sheffield 2013, Sheffield, United Kingdom, 4th July 2013 – Oral presentation

(8) J. Benton, J. Bai & T. Wang

"Enhancement in hydrogen generation efficiency using GaN nanostructure",

7th International Workshop on Nitride Semi-Conductors, Sapporo, Japan, 14-19th October 2012 – Oral presentation

(9) J. Benton, J. Bai & T. Wang

"Photoelectrochemical reaction & hydrogen production of *n*-type GaN"

UKNC Sheffield 2012, Sheffield, United Kingdom, 5th July 2012 – Oral presentation

Contents

NOVEL III-NITRIDE SEMICONDUCTORS FOR SOLAR HYDROGEN PRODUCTION **1**

ABSTRACT **I**

ACKNOWLEDGEMENTS **III**

PUBLICATION LIST **V**

CONTENTS **VII**

LIST OF FIGURES **XI**

LIST OF TABLES **XVII**

INTRODUCTION **- 1 -**

1.1 A Historical Perspective - 1 -
1.2 Climate Change & Hydrogen - 2 -
1.2.1 Solar Hydrogen *- 6 -*
Photoelectrochemical Hydrogen - 7 -
1.3 Issues & Limitations - 8 -
1.4 III-Nitrides - 9 -
Bibliography - 13 -

BACKGROUND **- 19 -**

2.1 Semiconductors - 19 -
2.1.1 Conduction, Mobility and Recombination *- 22 -*
2.1.3 Optical Properties *- 24 -*
2.1.4 Semiconductor-Metal Interface *- 25 -*
2.2 III-Nitride Semiconductors - 26 -
2.2.1 Structural Properties *- 27 -*
2.2.2 Band Gaps *- 28 -*
2.2.3 Growth *- 28 -*
Doping - 30 -
2.2.4 III-nitride Devices *- 31 -*
Quantum Wells - 31 -
Ohmic Contacts - 34 -
2.3 Electrochemistry - 34 -
2.3.2 Mass & Charge Transport *- 37 -*
Electric Double Layer - 39 -
2.3.3 Semiconductor-Electrolyte Interface *- 41 -*
Electron-Transfer Reactions - 43 -
2.4 Photoelectrolysis - 44 -
2.4.1 Efficiencies *- 48 -*
2.4.2 Current Approaches *- 49 -*
Photocorrosion - 51 -

2.4.4 III-Nitrides in Water Splitting - 52 -
BIBLIOGRAPHY - 55 -

EXPERIMENTAL TECHNIQUES - 63 -

3.1 GROWTH - 63 -
3.2 FABRICATION - 64 -
3.2.1 Dry Etch Techniques - 64 -
Reactive-Ion Etching - 65 -
Inductively Coupled Plasma RIE - 66 -
3.2.2 Photolithography - 66 -
3.2.3 Thin Film Deposition - 67 -
Plasma Enhanced Chemical Vapour Deposition - 67 -
Thermal Evaporation - 68 -
E-beam Evaporation - 69 -
Sputter Deposition - 69 -
3.2.5 Rapid Thermal Annealing - 69 -
3.3 CHARACTERISATION - 70 -
3.3.1 Photoluminescence - 70 -
3.3.2 Scanning Electron Microscopy - 71 -
3.3.3 Atomic Force Microscopy - 71 -
3.4 PHOTOELECTROCHEMICAL TECHNIQUES - 72 -
3.4.1 PEC Cell - 72 -
3.4.2 Step Voltage Testing - 73 -
3.4.3 Reliability Testing - 74 -
Hydrogen Monitoring - 74 -
3.4.4 Incident Photon Conversion Efficiency - 74 -
3.4.5 Accuracy and Error - 75 -
BIBLIOGRAPHY - 76 -

GAN NANOSTRUCTURES FOR ENHANCED SOLAR HYDROGEN PRODUCTION - 77 -

4.1 BACKGROUND - 77 -
4.1.1 Nanostructures for Solar Hydrogen - 77 -
4.1.2 GaN Nanorods - 79 -
GaN Nanostructures in Water Splitting - 80 -
4.2 AS-GROWN GAN DEVICES - 80 -
4.2.1 Fabrication - 80 -
4.2.2 Device Characterisation - 81 -
Atomic Force Microscopy (AFM) - 82 -
Hall Measurements - 83 -
4.2.3 Solar Hydrogen Performance - 84 -
Preliminary Measurements - 84 -
Electrolytes - 87 -
4.2.4 Summary - 89 -
4.3 GAN NANOSTRUCTURED DEVICES - 89 -

4.3.1 Fabrication - 89 -
4.3.2 Characterisation of Nanostructures - 91 -
Nanorod Diameter - 92 -
Nanorod Height - 95 -
4.3.3 Solar Hydrogen Performance - 95 -
Nanorod Diameter - 96 -
Height Optimisation - 97 -
4.3.4 Summary - 99 -
4.4 InGaN/GaN in Water Splitting - 99 -
4.4.1 Fabrication of InGaN/GaN MQW Devices - 99 -
4.4.2 Characterisation - 100 -
4.4.3 Solar Hydrogen Performance - 101 -
4.4.4 Summary - 104 -
4.5 Conclusions - 104 -
Bibliography - 105 -

NIO NANOPARTICLES ON GAN NANORODS FOR REDUCED ETCHING - 109 -

5.1 Cocatalysts in Water Splitting - 109 -
5.1.1 Cocatalysts on GaN - 112 -
5.2 GaN/InGaN Devices - 112 -
5.2.1 Fabrication - 113 -
5.2.2 Characterisation - 115 -
5.2.3 Step Photocurrent Measurements - 117 -
5.2.4 Steady State Measurements - 119 -
5.3 Conclusions - 126 -
Bibliography - 127 -

NANOPOROUS GAN FOR ENHANCED PHOTOELECTROCHEMICAL ACTIVITY - 129 -

6.1 Porous Semiconductors in Water Splitting - 129 -
6.2 History of Porous GaN & InGaN - 130 -
6.2.1 Etching Process - 132 -
6.2.2 Etched GaN/InGaN in Water Splitting - 133 -
6.3 Nanoporous GaN - 134 -
6.3.1 Fabrication - 134 -
Planar Porous GaN - 134 -
Porous Nanostructure GaN - 135 -
6.3.2 Characterisation - 136 -
Photoluminescence - 136 -
SEM Measurements - 139 -
6.3.3 Solar Hydrogen Performance - 143 -
Hydrogen Generation - 146 -
Incident Photon Conversion Efficiency - 147 -
6.3.4 Summary - 148 -
6.4 NiO Nanoparticles on Nanoporous GaN - 149 -

6.4.1 Fabrication - 149 -
6.4.2 Characterisation - 150 -
6.4.3 Solar Hydrogen Performance - 150 -
6.4.4 Summary - 151 -
6.5 NANOPOROUS INGAN/GAN MQW - 152 -
6.5.1 Fabrication - 152 -
6.5.2 Characterisation - 153 -
6.5.3 Solar Hydrogen Performance - 155 -
Hydrogen Measurements - 155 -
Incident Photon Conversion Efficiency - 156 -
6.5.4 Summary - 157 -
6.6 CONCLUSIONS - 157 -
BIBLIOGRAPHY - 159 -
CONCLUSION - 163 -
7.1 OVERVIEW - 163 -
7.2 FUTURE RESEARCH - 166 -
7.2.1 InGaN bulk films - 167 -
7.2.2 Intermediate Bands - 167 -
7.2.3 Device Properties - 168 -
7.2.4 Summary - 168 -
BIBLIOGRAPHY - 169 -

List of Figures

FIGURE 1-1 – CHANGES IN GLOBAL POPULATION AND OIL PRODUCTION 1950-2010. POPULATION DATA FROM WORLD POPULATION PROSPECTS, UNITED NATIONS DEPARTMENT OF ECONOMIC AND SOCIAL AFFAIRS, 2011.[8] OIL DATA FROM WORLD OIL PRODUCTION 1950-2009, EARTH POLICY INSTITUTE, 2011. - 2 -

FIGURE 1-2 – CHANGES IN WORLD PRIMARY ENERGY SUPPLY 1971-2010 IN KILO TONS OF OIL EQUIVALENT. DATA SOURCE INTERNATIONAL ENERGY AGENCY (IEA) VIA UK DATA SERVICE - 3 -

FIGURE 1-3 – CHANGES IN TRANSPORT CO_2 EMISSIONS FROM 1971 TO 2011 AS A PROPORTION OF TOTAL GLOBAL CO_2. DATA SOURCE INTERNATIONAL ENERGY AGENCY (IEA) VIA UK DATA SERVICE - 4 -

FIGURE 1-4 - BASIC SCHEMATIC OF PHOTOELECTROCHEMICAL CELL UNDER OPERATION - 7 -

FIGURE 1-5 – NUMBER OF PUBLICATIONS (WEB OF KNOWLEDGE) AND DEVELOPMENT OF GAN SINCE 1969 - 10 -

FIGURE 1-6 - PLOT OF BAND GAP OF $In_xGa_{1-x}N$ AT VARIOUS INDIUM COMPOSITIONS[74] ALONGSIDE INTENSITY OF SOLAR ENERGY - 11 -

FIGURE 2-1 – ILLUSTRATION OF METAL, SEMICONDUCTOR AND INSULATOR BAND STRUCTURES - 20 -

FIGURE 2-2 – REPRESENTATION OF DIRECT AND INDIRECT BAND STRUCTURES ON ENERGY-MOMENTUM DIAGRAMS - 21 -

FIGURE 2-4 – RADIATIVE RECOMBINATION MECHANISMS IN SEMICONDUCTORS[7] - 24 -

FIGURE 2-5 – SCHEMATIC REPRESENTATION OF METAL-SEMICONDUCTOR (*N*-TYPE) BAND STRUCTURES WHEN SEPARATED AND IN INTIMATE OHMIC CONTACT - 26 -

FIGURE 2-6 – ATOMIC STRUCTURES OF DIFFERENT CRYSTAL STRUCTURES (A) *ZINC BLENDE* (B) *WURTZITE* (C) *ROCK SALT* - 27 -

FIGURE 2-7 – (A) SIMPLE MODEL OF OPTICAL ABSORPTION IN QUANTUM WELLS (B) DENSITY OF STATES FOR A BULK (DASHED) AND QUANTUM WELL SEMICONDUCTOR - 32 -

FIGURE 2-8 – EFFECT OF POLARIZATION ON QUANTUM WELL BAND DIAGRAMS (A) POLAR C-PLANE GAN (B) NONPOLAR M-PLANE GAN[44] - 33 -

FIGURE 2-9 – ILLUSTRATION OF OXIDATION AND REDUCTION REACTIONS OCCURRING AT ELECTRODE-ELECTROLYTE INTERFACE - 36 -

FIGURE 2-10 – GENERAL REACTION PATHWAY AND MASS TRANSPORT BETWEEN BULK SOLUTION AND SURFACE REGION OF ELECTRODE. ADAPTED FROM BARD & FAULKNER, 2001.[55] - 38 -

FIGURE 2-11 – REPRESENTATION OF DIFFERENT DOUBLE LAYER MODELS PLUS ELECTROSTATIC POTENTIAL (Φ) DIAGRAMS VERSUS DISTANCE FROM ELECTRODE (X) OF EACH MODEL (A) HELMHOLTZ (B) GOUY-CHAPMAN (C) STERN MODELS - 40 -

FIGURE 2-12 – BAND STRUCTURES OF *N*-TYPE SEMICONDUCTORS IN ELECTROLYTE SOLUTION (A) EQUIVALENT FERMI LEVEL AND REDOX POTENTIALS (B) SEMICONDUCTOR FERMI LEVEL < REDOX POTENTIAL (C) SEMICONDUCTOR FERMI LEVEL > REDOX POTENTIAL (D) SEMICONDUCTOR FERMI LEVEL >> REDOX POTENTIAL - 42 -

FIGURE 2-13 – ELECTRON-TRANSFER REACTIONS FOR *N*-TYPE SEMICONDUCTOR WITH REDOX ELECTROLYTE (A) OVERLAP AT CONDUCTION BAND (B) VALENCE BAND OVERLAP (C) CONJUGATION OF SURFACE STATES & REDOX LEVEL - 44 -

FIGURE 2-14 – ENERGY DIAGRAMS OF WATER SPLITTING BASED ON (I) TYPE I SYSTEM USING A SINGLE SEMICONDUCTOR AND EXCITATION AND (II) TYPE II IN WHICH A TWO-STEP EXCITATION OF TWO SEMICONDUCTORS (Z-SCHEME) - 46 -
FIGURE 2-15 – SCHEMATIC OF *N*-TYPE PHOTOANODE UNDER OPERATION FROM IRRADIATION SOURCE - 47 -
FIGURE 2-16 – BAND POSITIONS OF VARIOUS SEMICONDUCTORS UTILISED FOR SOLAR HYDROGEN PRODUCTION - 50 -
FIGURE 2-17 – TIMELINE OF DEVELOPMENTS IN III-NITRIDES FOR WATER SPLITTING. ONLY FIRST OR SIGNIFICANT REPORTS MENTIONED AND LISTED IN PUBLICATION ORDER - 52 -
FIGURE 3-1 – SCHEMATIC ILLUSTRATION OF REACTION PROCESS IN A METAL ORGANIC CHEMICAL VAPOUR DEPOSITION (MOCVD) REACTOR FOR THE GROWTH OF GAN - 64 -
FIGURE 3-2 – SCHEMATIC OF PHOTOLUMINESCENCE EXPERIMENTAL SET-UP - 70 -
FIGURE 3-3 - PHOTOGRAPH OF PHOTOELECTROCHEMICAL CELL UTILISED IN MAJORITY OF TESTING - 72 -
FIGURE 3-4 - SCHEMATIC OF EXPERIMENTAL SET-UP - 73 -
FIGURE 4-1 – VARIATION IN CHARGE COLLECTION IN DIFFERENT SEMICONDUCTOR STRUCTURES. L_H: HOLE DIFFUSION LENGTH; L_E: ELECTRON DIFFUSION LENGTH. ADAPTED FROM OSTERLOH (2013)[2] - 78 -
FIGURE 4-2 – ROOM TEMPERATURE PHOTOLUMINESCENCE OF SILICON DOPED GAN (INSET) SCHEMATIC OF DONOR-ACCEPTOR RECOMBINATION MODEL IN *N*-GAN - 82 -
FIGURE 4-3 – AFM SCAN OF *N*-TYPE GAN WAFER (A) 100 μM^2 SURFACE PROFILE (B) 3D TOPOGRAPHY OF 4 μM^2 SCAN - 83 -
FIGURE 4-4 - VARIATION IN CURRENT DENSITY WITH CARRIER CONCENTRATION OF DIFFERENT SAMPLES AT 0 V BIAS IN 1 M HCL UNDER 150 W XE LAMP ILLUMINATION, BLACK SQUARES INDICATE SAMPLES FROM SAME TEST RUN, RED CIRCLES ARE LITERATURE VALUES OF VARIOUS TESTS. SHADED AREA INDICATES CARRIER CONCENTRATION OF DEVICES USED IN THIS WORK. ADAPTED FROM ONO *ET AL.*. 2007[36] - 84 -
FIGURE 4-5 – DARK AND LIGHT PHOTOCURRENT MEASUREMENTS OF AS-GROWN *N*- AND *P*-TYPE GAN DEVICES IN A 1 M HCL ELECTROLYTE SOLUTION. ILLUMINATION INTENSTIY WAS 100 MW CM-2. - 85 -
FIGURE 4-6 – PHOTOELECTROCHEMICAL WATER SPLITTING OF 0.5 M HCL WITH *N*-GAN ELECTRODE UNDER ~500 MW CM^{-2} AND 0.8 V APPLIED BIAS (A) PHOTOCURRENT DENSITY (B) THEORETICAL AND ACTUAL HYDROGEN PRODUCTION - 86 -
FIGURE 4-7 – PHOTOCURRENT DENSITIES OF *N*-GAN WITH DIFFERENT ELECTROLYTES UNDER 100 MW CM^{-2} AM1.5 XE LAMP ILLUMINATION - 87 -
FIGURE 4-8 – SCHEMATIC OF NANOROD FABRICATION VIA USE OF SELF-ORGANISED NICKEL NANOPARTICLES - 90 -
FIGURE 4-9 – SEM IMAGES OF NANOROD FABRICATION (A) NICKEL NANOISLAND MASK (B) ETCHED SILICON DIOXIDE MASK (C) PLAN VIEW OF FABRICATED NANORODS (D) TILTED IMAGE OF FINISHED NANORODS - 91 -
FIGURE 4-10 – RELATIONSHIP BETWEEN NICKEL THICKNESS AND NANOROD DIAMETER (INSET) VARIATION IN NANOROD DENSITY PER CM^2 - 92 -
FIGURE 4-11 - DEVIATION OF NANOROD DIAMETERS WITH DIFFERENT NICKEL FILM THICKNESSES - 93 -
FIGURE 4-12 - SEM INDICATING NANOROD SIZE AND DENSITY OF VARIOUS NICKEL MASK THICKNESSES (A) 4 NM (B) 6 NM (C) 8 NM (D) 10 NM (E) 15 NM (F) 20 NM - 94 -

FIGURE 4-13 - NORMALIZED ROOM TEMPERATURE PL OF DIFFERENT DIAMETER NANORODS - 95 -
FIGURE 4-14 – (A) VARIATION OF NANOROD HEIGHT WITH ETCH TIME (B) SEM OF 1.5 MINUTE ICP ETCH (C) SEM OF 10 MINUTE ICP ETCH - 95 -
FIGURE 4-15 - PHOTOCURRENT VALUES FOR DIFFERENT NANOROD DIAMETERS CAUSED BY VARYING NICKEL THICKNESS - 96 -
FIGURE 4-16 – VARIATION IN ETCH DEPTH OF GAN NANORODS - 98 -
FIGURE 4-17 – CHANGES IN ABSORBED FLUX OF DIFFERENT NANORODS (A) 150 NM NANORODS (B) 1000 NM NANORODS - 99 -
FIGURE 4-18 – STRUCTURE OF INGAN/GAN MQW WAFER - 100 -
FIGURE 4-19 – CHARACTERISATION OF INGAN/GAN MQW SAMPLES (A) NORMALISED ROOM TEMPERATURE PL MEASUREMENTS OF AS-GROWN AND NANOROD DEVICES (B) SEM IMAGE OF FABRICATED NANORODS - 101 -
FIGURE 4-20 – PHOTOCURRENT OF AS-GROWN AND NANOROD PHOTOELECTRODES AS A FUNCTION OF BIAS UNDER 100 MW CM^{-2} ILLUMINATION AND "DARK" CONDITIONS - 102 -
FIGURE 4-21 – PHOTOELECTROCHEMICAL MEASUREMENTS UNDER 400 MW CM^{-2} ILLUMINATION AND 0.8 V BIAS (A) PHOTOCURRENTS OF THE AS-GROWN AND NANOROD SAMPLE AS A FUNCTION OF TIME (B) OBTAINED AND THEORETICAL HYDROGEN MEASUREMENTS AS A FUNCTION OF TIME - 103 -
FIGURE 5-1 – ILLUSTRATION OF HYDROGEN AND OXYGEN EVOLUTION ON A CORE/SHELL STRUCTURE ON A BULK PHOTOELECTRODE MATERIAL. ADAPTED FROM MAEDA, 2010.[2] - 110 -
FIGURE 5-2 - BAND STRUCTURES OF WIDE BAND GAP SEMICONDUCTOR (I) AND COCATALYST (II) - 111 -
FIGURE 5-3 – RELATIVE CONDUCTION AND VALENCE BAND POSITIONS OF NIO AND GAN BASED SEMICONDUCTORS - 113 -
FIGURE 5-4 – EXAMPLES OF NIO FABRICATION (A) AFTER NICKEL DEPOSITION (B) AFTER ANNEALING - 114 -
FIGURE 5-5 – SEM IMAGES OF INGAN/GAN MQW WITH AND WITHOUT NIO. INSETS DISPLAY PLAN VIEW OF NANORODS. (A) FROM WAFER A (B) FROM WAFER A W/NIO (C) FROM WAFER B (D) FROM WAFER B W/NIO (E) FROM WAFER C (F) FROM AFER C W/NIO - 115 -
FIGURE 5-6 – ROOM TEMPERATURE PHOTOLUMINESCENCE OF INGAN/GAN MQW WAFERS WITH AND WITHOUT NIO - 116 -
FIGURE 5-7 – PHOTOCURRENT MEASUREMENTS AT 100 MW CM-2 IRRADIATION IN A 1 M NAOH ELECTROLYTE AT BIASES FROM -1 TO 2 V (A) PLANAR *N*-TYPE GAN (B) INGAN/GAN NANO STRUCTURE FROM WAFER A (C) INGAN/GAN NANOSTRUCTURE FROM WAFER B (D) INGAN/GAN NANOSTRUCTURE FROM WAFER C - 118 -
FIGURE 5-8 – SCHEMATIC OF THE BAND DIAGRAMS AND ILLUMINATION MECHANISM OCCURRING IN GAN/NIO STRUCTURE WHEN NIO NANOARTICLES OR GAN ARE ILLUMINATED - 119 -
FIGURE 5-9 – STEADY STATE PHOTOCURRENT MEASUREMENTS OF THE DEVICE FABRICATED FROM WAFER B WITH AND WITHOUT NIO. PERFORMANCE ENHANCEMENT OVER THE DEVICE WITHOUT NIO NANOPARTICLES AS A REFERENCE SAMPLE OVER TIME ALSO ILLUSTRATED. - 120 -
FIGURE 5-10 – SEM IMAGES OF NANORODS OVER TIME AFTER PHOTOCURRENT MEASUREMENTS. LEFT HAND SIDE: REFERENCE NANORODS, RIGHT HAND SIDE: NANORODS WITH NIO (A)-(D) DEVICES FROM WAFER B AT 15 MINUTES, 50 MINUTES, 105 MINUTES AND 180 MINUTES (E) DEVICES FROM WAFER A AT 180 MINUTES (F) DEVICES FROM WAFER C AT 180 MINUTES - 121 -

FIGURE 5-11 – ANALYSIS PROCESS WHEN USING IMAGEJ (A) INITIAL LOADING OF THE IMAGE (B) BINARY CONVERSION OF THE IMAGE (C) DETAILED ANALYSIS OF EACH PARTICLE - 123 -
FIGURE 5-12 – NANOROD COVERAGE OF ALL SIX DEVICES WITH AND WITHOUT NIO BASED ON IMAGEJ ANALYSIS OF TOP-DOWN SEMS, REPRESENTATIVE ERRORS ARE ILLUSTRATED FOR DEVICES FROM WAFER B - 124 -
FIGURE 5-13 – DISTRIBUTION OF NANOROD SIZES FOR (A) WAFER B AND (B) WAFER B W/NIO - 125 -
FIGURE 6-1 - AFM IMAGE OF EARLY POROUS GAN LAYER, INSET IMAGE DISPLAYS AN ENLARGED SINGLE PIT, GREYSCALE OF IMAGE CORRESPONDS TO HEIGHT VARIATION OF 150 NM. ADAPTED FROM (MYNBAEVA, 2000)[21] AND PERMISSION OBTAINED FROM COPYRIGHT HOLDER © AIP PUBLISHING - 131 -
FIGURE 6-2 – NORMALISED ROOM TEMPERATURE PL SPECTRA OF NANO POROUS STRUCTURES FABRICATED FROM A PLANAR AS-GROWN WAFER - 137 -
FIGURE 6-3 – ROOM TEMPERATURE PL FOR NANOPOROUS NANOROD SAMPLES H-M. THE AS-GROWN SAMPLE A HAS BEEN INCLUDED AS A REFERENCE. - 138 -
FIGURE 6-4 – SEM IMAGES OF POROUS GAN SAMPLES. (A) TYPICAL CROSS SECTION OF POROUS SAMPLES OBTAINED FROM SAMPLE C. (B)-(G) TOP DOWN SEM IMAGES OF SAMPLES B-G RESPECTIVELY - 140 -
FIGURE 6-5 – SEM IMAGES OF POROUS NANOROD SAMPLES. (A) REFERENCE NANOROD SAMPLE (B)-(E) POROUS NANOROD SAMPLES I-L - 142 -
FIGURE 6-6 – PHOTOCURRENT AS A FUNCTION OF BIAS UNDER DARK AND ILLUMINATED CONDITIONS FOR (A) THE SAMPLES FABRICATED UNDER DIFFERENCE KOH CONCENTRATIONS; AND (B) THE SAMPLES FABRICATED UNDER DIFFERENT VOLTAGES SUPPLIED - 144 -
FIGURE 6-7 – PHOTOCURRENT AS A FUNCTION OF BIAS FOR THE REFERENCE AS GROWN DEVICE (SAMPLE A), REFERENCE NANOROD DEVICE(SAMPLE H) AND POROUS NANOROD DEVICES (SAMPLES I-L) - 145 -
FIGURE 6-8 – MEASURED (POINTS) AND THEORETICAL (SOLID LINE) HYDROGEN VALUES FOR POROUS SAMPLES AT 0.8 V BIAS IN HCL UNDER 500 MW CM^{-2} ILLUMINATION FOR AS-GROWN GAN (A), POROUS GAN (D), NANOROD GAN (H) POROUS NANOROD GAN (K) - 147 -
FIGURE 6-9 – INCIDENT PHOTON CONVERSION EFFICIENCY (IPCE) AS A FUNCTION OF WAVELENGTH FOR (A) GAN BASED NANOPOROUS STRUCTURES AND (B) THE POROUS NANOROD STRUCTURES - 148 -
FIGURE 6-10 – SEM IMAGES OF (A) NANOPOROUS SAMPLE (B) NANOPOROUS SAMPLE WITH NIO NANOPARTICLES - 150 -
FIGURE 6-11 – PHOTOCURRENT MEASUREMENTS UNDER ONE SUN ILLUMINATION IN 1 M HCL (A) PHOTOCURRENT AS A FUNCTION OF VOLTAGE FOR POROUS AND POROUS W/ NIO (B) PHOTOCURRENT VERSUS TIME FOR THE POROUS NIO SAMPLE AT 0.8 V BIAS - 151 -
FIGURE 6-12 – ROOM TEMPERATURE PL MEASUREMENTS OF INGAN/GAN MQW DEVICES. A = PLANAR REFERENCE B = POROUS PLANAR C = NANOROD REFERENCE D = POROUS NANOROD - 153 -
FIGURE 6-13 – SEM IMAGES OF POROUS INGAN/GAN MQW STRUCTURES (A) & (B) POROUS INGAN/GAN, SAMPLE B (C) REFERENCE INGAN/GAN NANORODS, SAMPLE C (D) & (E) POROUS INGAN/GAN NANORODS, SAMPLE D - 154 -
FIGURE 6-14 – PHOTOCURRENT MEASUREMENTS AS A FUNCTION OF BIAS FOR INGAN/GAN MQW SAMPLES IN 1M HCL AND 1 SUN ILLUMINATION - 155 -

FIGURE 6-15 – HYDROGEN GENERATION MEASUREMENTS OF REFERENCE INGAN/GAN SAMPLE (A) AND POROUS INGAN/GAN SAMPLE (B) IN 1 M HCL AT 0.8 V AND 500 MW CM^{-2} XE LAMP ILLUMINATION. LINES INDICATE THEORETICAL MAXIMUM - 156 -
FIGURE 6-16 – INCIDENT PHOTON CONVERSION EFFICIENCY OF INGAN/GAN REFERENCE SAMPLES A AND C AND POROUS INGAN/GAN DEVICES SAMPLES B AND D - 157 -

List of Tables

TABLE 4-1 - REDUCTION HALF REACTIONS AND POTENTIALS OF 1 MOL DM^{-3} SOLUTION UNDER 1 ATM PRESSURE ..... - 88 -
TABLE 6-1 – FABRICATION CONDITIONS OF PLANAR POROUS STRUCTURES..... - 135 -
TABLE 6-2 – FABRICATION CONDITIONS OF NANOROD POROUS STRUCTURES..... - 135 -
TABLE 6-3 – FABRICATION CONDITIONS AND PORE SIZES OF INGAN/GAN MQW SAMPLES. A IS PLANAR SAMPLE, B IS POROUS PLANAR SAMPLE, C REFERENCE NANOROD SAMPLE AND D POROUS NANOROD SAMPLE..... - 153 -

Chapter 1

Introduction

Climate change is becoming an increasingly significant area of interest for global Governments and scientists. Research into new energy technologies is prevalent. Solar energy is naturally abundant and III-nitride materials have the capability to harness the majority of visible energy in both solar cells and solar hydrogen technologies.

1.1 A Historical Perspective

Undoubtedly humanity has shaped the environment we live in, just as the natural environment has shaped the development of humanity.[1] Over the course of our history, the impact we have had on the surrounding landscape has changed significantly. This has evolved from first harnessing fire, through to the modern age where we are now capable of a tapping oil reserves in some of the harshest conditions in the world, the Arctic.[2] Since the advent of industrialisation in 1760 our potential to effect change has risen dramatically.[3] Humanity has flourished, the environment however has suffered. Deforestation, biodiversity and climatic changes are just a few of the issues currently being faced.[4] These are not issues for Earth's survival, they are however important factors in determining the future of humanity.[5]

Societal changes and increases in the availability of energy have resulted in significant increases in the global population (Figure 1-1).[6] Along with the rising numbers of people, global oil production has also increased at a similar rate (Figure 1-1). As a result of the increased population and the expanding global economy, humanity has never had a more significant role in shaping the future of Earth's ecosystems. Land use, biodiversity and animal populations are all to some extent under mankind's dominion.[7] With dominion comes a responsibility to manage and presently, humanity has been an underperforming caretaker. Sustainable development and green technology are essential aspects for the future of humanity while restoring aspects of the natural environment to preindustrial standards.

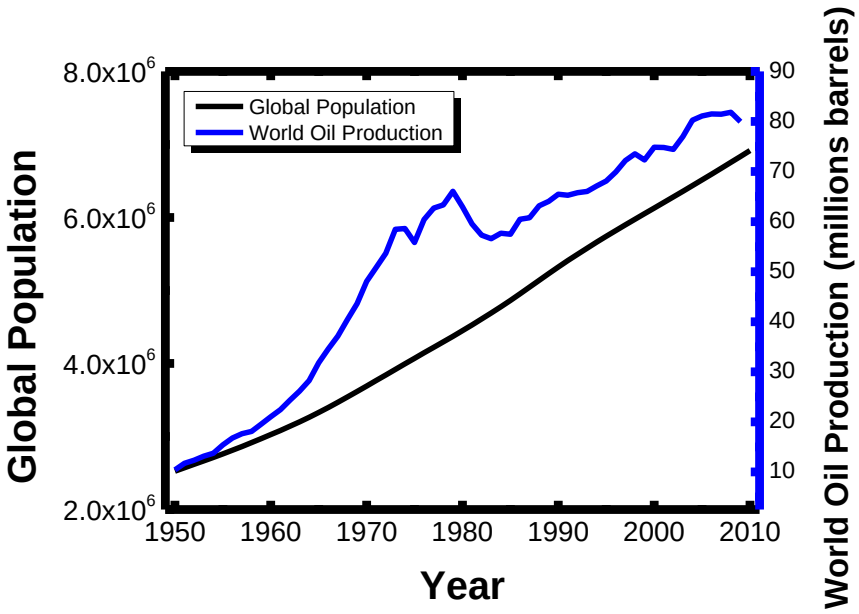

Figure 1-1 – Changes in global population and oil production 1950-2010. Population data from World Population Prospects, United Nations Department of Economic and Social Affairs, 2011.[8] Oil data from World Oil Production 1950-2009, Earth Policy Institute, 2011.

1.2 Climate Change & Hydrogen

It is now widely accepted that human actions have played a role in climate change.[9] The natural greenhouse cycle that increases the surface temperature of the Earth has been significantly affected by anthropogenic emissions of greenhouse gases (GHG – carbon dioxide, water vapour, methane, nitrous oxide, ozone, CFCs), resulting in temperature rises of

between 0.3 and 0.6 °C over the past 100 years. Sea levels have also been altered, leading to changes in land masses and climatic conditions. It is predicted that under current business as usual practices, by the end of the 21st century, sea levels could be 0.59 m higher than their current level.[9] With 10 % of the global population living at an elevation level of 10 m or less there is potential for devastating effects to society. Coastal areas in Africa and South East Asia are particularly vulnerable as well as the island nations in the Pacific and Indian Ocean.[10] Anthropogenic emissions of carbon dioxide have contributed to the 40 % increase in atmospheric levels compared to 1750, leading to the warmer climate and sea level changes.[11] Without intervention, global temperatures are expected to increase by at least 2 °C, the defined tolerable level,[12] by the end of the 21st century. Achieving this target requires a unified multi-faceted approach, one aspect of which is the current global energy mix.[13]

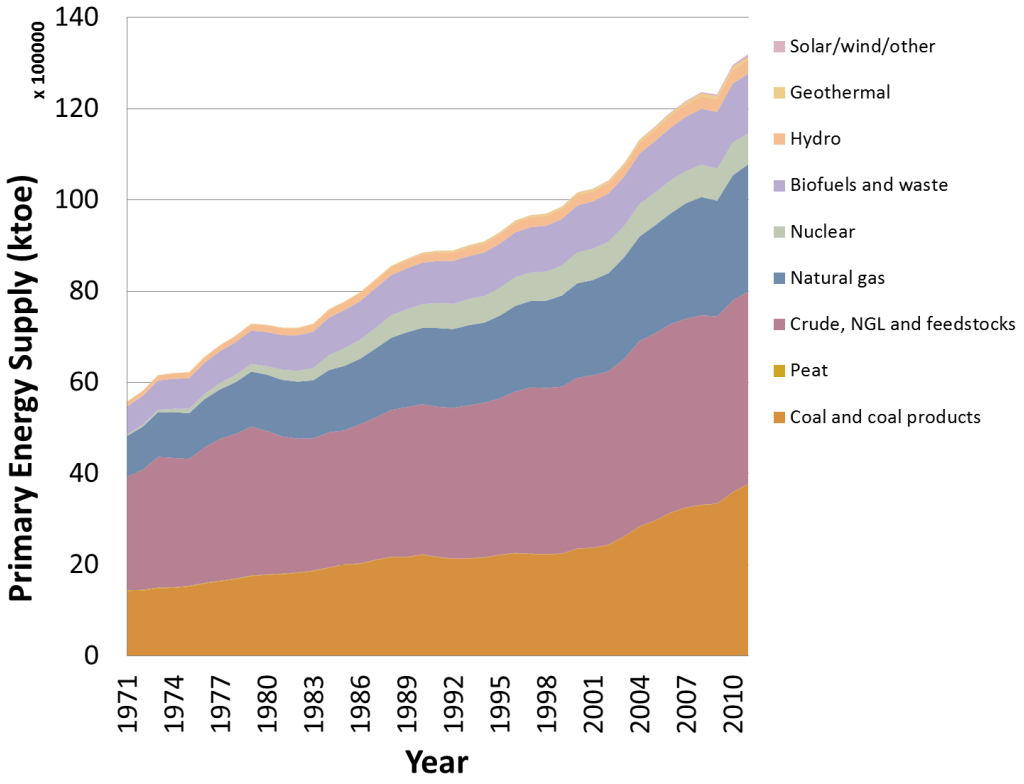

Figure 1-2 – Changes in world primary energy supply 1971-2010 in kilo tons of oil equivalent. Data source International Energy Agency (IEA) via UK Data service

Since the industrial revolution and the refining of oil in the 19th century there has continued to be a significant increase in energy production. This

has risen from ~94 million tons of oil equivalent (Mtoe) in 1860[14] to ~13,113 Mtoe in 2011. Despite reductions in energy intensity[15] global supply continues to increase (Figure 1-2). Accounting for 99 % of global carbon emissions, as well as being major contributors for other GHGs, there is a requirement to move away from conventional fossil based fuels. Presently, global uptake of renewable energy is estimated to account for 19 % of final energy consumption, in which traditional biofuel and biomass products account for 10 %.[16] Despite over a six fold increase in renewable power capacity since 2004 and a tripling of countries setting policy targets, fossil fuel usage continues to increase (Figure 1-2).

The global effort to reduce GHG emissions is improving with renewable fuel accounting for a greater proportion of new capacity in China and the EU-27 in 2013.[16] Efficiency improvements,[17] policy changes[18] and new technology[19] are helping to reduce carbon intensity across a variety of sectors. Despite these changes, global emissions continue to increase, specifically in upper middle income economic countries, which overtook high income countries for the first time in 2010.[20] A significant change is therefore required in order to prevent the continual increase in carbon emissions. An area of considerable interest is the transport sector. Accounting for over 20 % of global emissions (Figure 1-3), the decarbonisation of transport can play a vital role in reaching the target CO_2 emission goals.

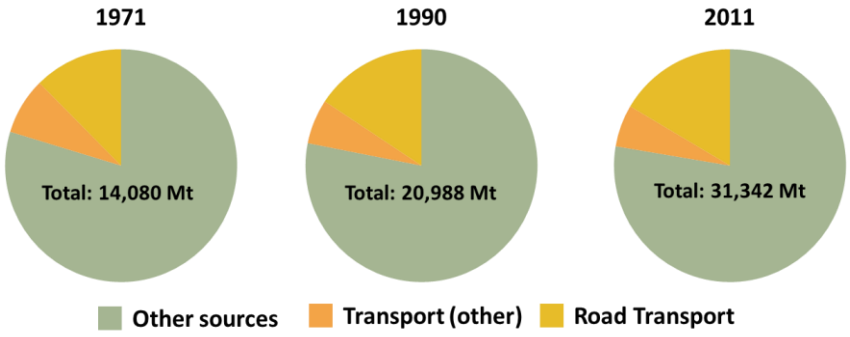

Figure 1-3 – Changes in Transport CO_2 emissions from 1971 to 2011 as a proportion of total global CO_2. Data source International Energy Agency (IEA) via UK Data Service

Since 1971 (Figure 1-3), the role of road transport has risen from 1,108 Mt CO_2 in 1971 to 5,172 Mt CO_2 in 2011. There are a number of potential

options to achieve transport decarbonisation. In road vehicles, biofuels, electrification and the use of hydrogen are all being considered.[21] There is much discussion regarding the viability and potential of each fuel to replace conventional sources in vehicles[22,23] however electric and hydrogen based fuels have the benefit of zero emission at use, unlike biofuels. Electric vehicles (EV) are significantly further progressed than their hydrogen counterparts with a number of vehicles available for consumer purchase. However, EV still face many challenges.[24] The current carbon intensity of the electricity market, the driving range of the vehicles themselves and consumer attitudes towards the vehicles can be a limit to their widespread uptake.[25]

The energy density of hydrogen is such that the range of hydrogen vehicles can be closer to conventional vehicles, with new vehicles from Toyota and Hondo offering a 300 mile range, close to the 320 miles required for US drivers.[26] It has been postulated that climate change in its entirety is the greatest pressure on mankind to adapt and alter societal behaviours[27] and therefore hydrogen vehicles offer a clean alternative that reduces the requirement for mass social change. This is not to say hydrogen vehicles are issue free. Production costs and safety requirements[28] in regards to the infrastructure are still required to be overcome to ensure the uptake, however pilot projects and commercial interest are pushing the technology forward to become cost competitive.[26,29,30]

A major component of any secondary energy carrier, such as electricity and hydrogen, is the source.[31] Hydrogen is a commercially produced commodity and with that, the knowledge surrounding production techniques, efficiencies and handling is mature. This is a beneficial aspect of a future hydrogen based transport system. However, current production methods of hydrogen are energy and carbon intensive.[32] Along with current techniques, if hydrogen is to become a major fuel source for road transportation, global production is required to significantly increase in order to continue to meet the demands of current business requirements. Renewable production of hydrogen arises in a few forms as a potential alternative to meet the increased demand while ensuring the cycle remains

carbon free. Clean hydrogen production can come from the use of renewable electricity generation (wind/solar/wave) combined with a conventional electrolyser or various solar techniques.[33] As enough solar energy reaches the Earth in 1 hour to meet global yearly power requirements, solar hydrogen is an area of significant potential.[34]

1.2.1 Solar Hydrogen

Solar technologies have developed considerably with solar photovoltaics achieving efficiencies greater than 38 % under standard terrestrial conditions.[35] There is also a great deal of potential for the wide scale application of solar energy to provide more than current global electricity requirements.[36] In regards to implementing solar energy for hydrogen production there a few pathways available, (i) solar photovoltaic and electrolyser (ii) concentrated solar thermal and electrolyser (iii) thermo-chemical (iv) biological processes and (v) photoelectrochemical (PEC).

Systems that combine an energy generation step with an electrolyser such as (i) and (ii) rely on the efficiency of the initial generation step and that of the electrolyser. With typical commercial electrolysers performing at efficiencies of 73 %,[37] even with the optimum solar cell a performance of around 27 % is achievable, whereas for typical commercial silicon-PV it is approximately 10 %. As it is technologically viable, it is definitely a promising option. Currently there are issues surrounding land requirements and the total cost of systems. Concentrated solar arrays can be utilised across all solar devices leading to potential performance enhancements.[38] However direct photolysis is not a viable option, with temperatures of 4000 °C required, higher than those typically achieved with concentrated systems.[33]

Due to the high temperatures required for direct photolysis, multi-step thermo-chemical cycles have been investigated to reduce the required temperature. These offer a promising route with potential efficiencies of 70 % achievable. The main focus has been via the use of metal oxide cycles, in which ZnO is favourable due to a completion temperature of ~2000 °C.[38] The process operates via the decomposition of the metal oxide before the

formation of ZnO via the introduction of H_2O into the system, generating hydrogen. The technological challenges facing the redox couples during the process are of concern in order to produce a commercially viable system.[33]

Biological processes have received a considerable degree of interest[39] and can work via photosynthesis or photo-fermentation. Photolytic production with green algae or cyanobacteria is a direct process in which the algae convert water molecules into hydrogen and oxygen during photosynthesis. Although theoretical efficiencies of 80 % have been postulated,[40,41] this is unlikely due to the nature of the algae to self-assemble and current values are less than 1 %. Photo-fermentation produces hydrogen using light energy and organic acids. Algal based processes currently suffer from low efficiencies and the requirements of specialised bioreactors to achieve improved production rates.[32]

The above technologies all suffer from a range of issues including cost, area requirements, feasibility and overall efficiencies.[42] An alternative technology that offers long term promise is photoelectrochemical production of hydrogen in which an efficiency of over 12 % has been achieved.[43]

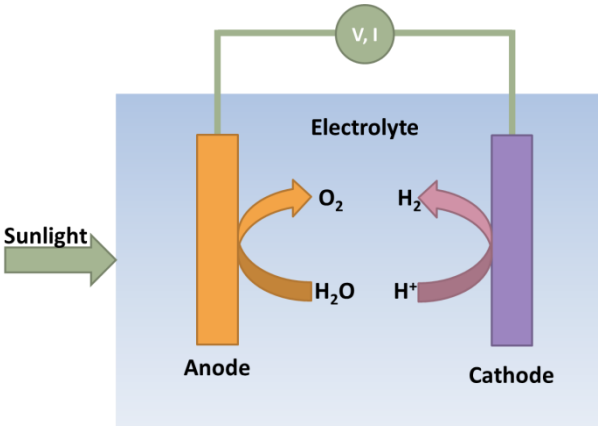

Figure 1-4 - Basic schematic of photoelectrochemical cell under operation

Photoelectrochemical Hydrogen

Photoelectrochemical production of hydrogen is a form of direct photolysis in which water is split into the hydrogen and oxygen constituents via the use of a semiconductor material and sunlight. At room temperature, water splitting requires 1.23 V to form oxygen and hydrogen to overcome the

reaction potentials. Due to surface interactions and losses within the system this typically increases to between 1.6 and 1.8 V. Solar energy can be sufficiently utilised for this process, as by converting the required energy into a wavelength results in a value of ~690 nm, meaning almost the entire visible spectra has sufficient energy to split water.

The process was first reported in 1972 by Fujishima and Honda,[44] using a TiO_2 electrode. Typically semiconductor materials similar to those used in photovoltaic applications have been investigated.[43] The process can occur via the use of a single semiconductor and metal electrode or two semiconductor electrodes. The basic principle occurs when sunlight is absorbed via the semiconductor material and unlike generating electricity as in photovoltaic cells, splits the electrolyte solution into hydrogen and oxygen (Figure 1-4). This process will be thoroughly described in Chapter 2.

In comparison to other production methods described, PEC has the potential for wide-scale application due to the use of ambient temperatures, relatively simple infrastructure and large energy resource. With an efficiency of just 10 %, it is thought that around 0.1 % of US land mass would be required to power the entire US fleet.[43] Alongside these benefits, unlike algal systems, there is the potential for compact systems, allowing small scale production for domestic use as a vehicle fuel or energy store.[45] Furthermore, the potential of PEC systems is not limited solely to hydrogen production, with developments of pollutant and CO_2 treatment systems also being investigated.[46,47]

1.3 Issues & Limitations

In order for photoelectrochemical hydrogen to succeed there are a number of requirements that have to be satisfied. First, the semiconductor material in use is required to have the correct band alignment to effectively split water. Additionally the overall absorption efficiency is required to be at least 80 % and it has to be able to withstand the chemical solutions implemented over an adequate working timescale.[42] Although over 40 years since the initial discovery the progress is still far from ideal. Due to the total

available materials numbering over 2 million,[43] progress in search of the ideal candidates has been limited. Advances in material design techniques have allowed a greater variety of materials to be screened, increasing the rate at which advances are made.[48,49]

Aside from process specific issues, the practicality of the material also has to be considered. Requirements with regards to commercialisation are a necessary issue in order to obtain a cost efficient device.[50] If hydrogen is to be widely utilised, production capacity is required to significantly increase.[51,52] Any material implemented within a solar production route is required to have sufficient capacity for wide-scale device production. III-nitride materials have the potential to satisfy a number of these concerns.

1.4 III-Nitrides

The history of III-nitride based semiconductor materials originates from the early 20th century with the discovery of both AlN and InN within the space of three years.[53,54] GaN was not reported until 1932,[55] however it was not until the 1990s, with the fabrication of a blue GaN light-emitting diode (LED), that their potential began to be realised.[56] Despite discovery in 1932, single crystal GaN proved difficult to obtain and it was not until 1969 that it was successfully grown via hydride vapour phase epitaxy (HVPE).[57] The challenge of growing high quality GaN resulted in a limited research focus, demonstrated by the research plateau between the 70 and 80's (Figure 1-5).

Invention of the low-temperature buffer techniques in 1986[58] resulted in a significant increase the quality of the material being grown. The technique works via the insertion of a thin nucleation layer of aluminium/gallium nitride grown at a low temperature (LT). Grown directly on foreign substrates (sapphire), GaN grows via three-dimensional islands which all have slight misalignments with each other resulting in poor quality films observed prior to the LT technique. At low temperature, two-dimensional growth dominates resulting in improved optical, electrical and structural characteristics.[59] Shortly after, the technique allowed the growth of *p*-type GaN, previously unobtainable.[60,61] *P*-type GaN is grown via the

addition of magnesium as a dopant, but is required to be activated in order to achieve the necessary properties to be identified as a *p*-type semiconductor.[62]

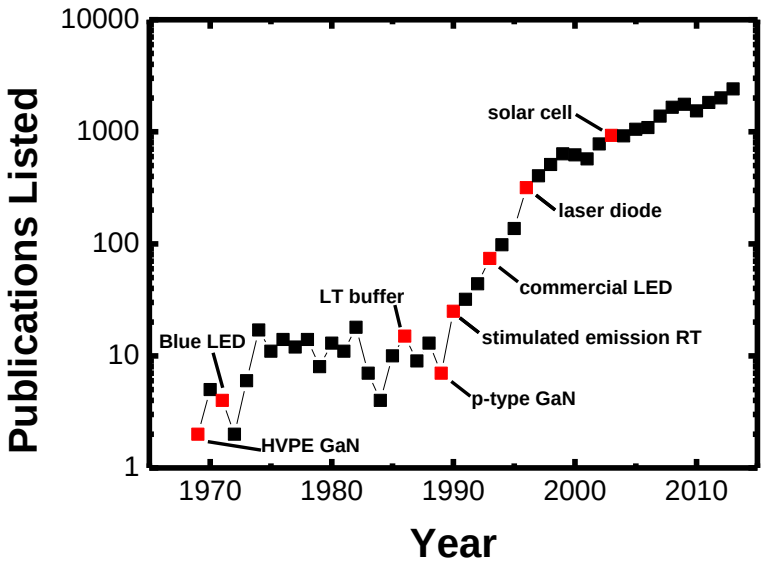

Figure 1-5 – Number of publications (Web Of Knowledge) and development of GaN since 1969

A property of III-nitride materials is their miscible nature. Despite the different material properties, aluminium, indium and gallium nitrides have the ability to form binary and ternary alloys in any composition.[63] As with GaN, early alloys were of low quality[64] and it was not until the incorporation of the LT growth technique that band-to-band emission was observed.[65] Development of both *p*- and *n*- type nitride materials and III-nitride alloys resulted in the first *p*-n junction LED to be developed,[62] leading to the fabrication of high brightness double heterostructure blue LEDs in 1994.[66] The interest in GaN materials has continued to increase with publications increasing in significant numbers over the past two decades (Figure 1-5). This has resulted in III-nitride materials taking a role in the development of Blu-ray technology[67] and in the fabrication of high efficiency LEDs.[68] The contribution of GaN to high brightness white LEDs places them at the forefront of solid-state lighting and energy efficient displays.[69] The constant development has led to an increased understanding of the material properties and reduced costs.

Although the development of III-nitride based technologies for lighting is well-established, there has also been interest in the potential for other optoelectronic devices such as solar technologies.[70] Due to their direct band gaps ranging from ~0.7 eV (InN) to 6.1 eV (AlN) it is possible to form alloys with a band gaps that span the entire solar spectrum (Figure 1-6). It is therefore possible to create devices that have the capability of harnessing significant portions of solar energy. Tuneable band gaps allow the formation of multi-junction devices without requiring the matched lattice properties required if different semiconductor materials are utilised.[71] Based on theoretical calculations, efficiencies in excess of 54 % has been stated for a III-nitride based device.[72] As well as their optical and electronic properties, the chemical properties of the III-nitride group are another reason for the attention they are gathering.[71] Their strong resistance against both chemicals and high-energy radiation has resulted in the potential for space applications.[73]

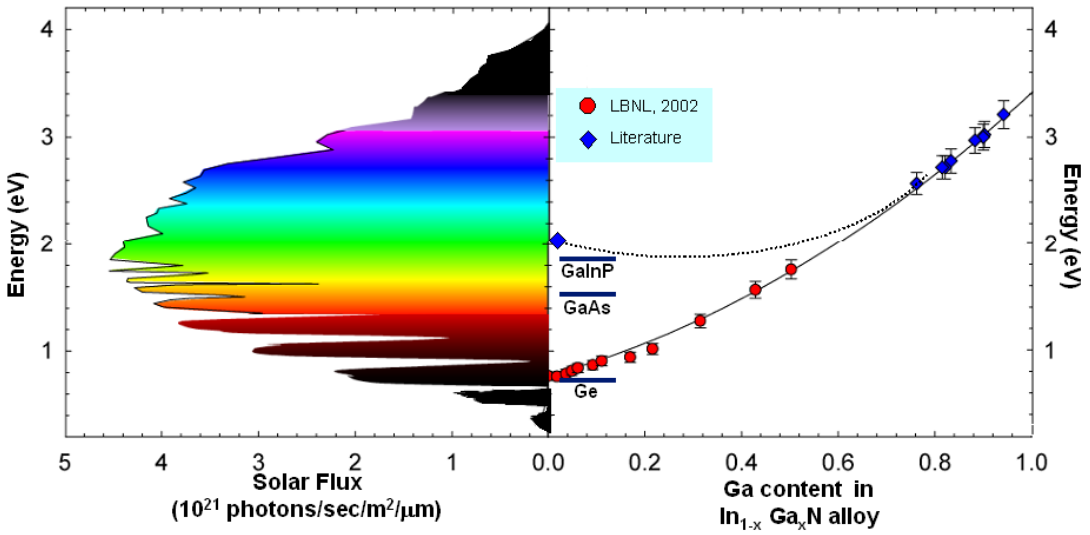

Figure 1-6 - Plot of band gap of $In_xGa_{1-x}N$ at various indium compositions alongside intensity of solar energy[74]

The properties that make III-nitrides suitable for solar photovoltaics also lend themselves to applications in photoelectrochemical water splitting. As stated, the strong chemical resistance of the III-nitrides and their growth substrates[75] mean they are capable of withstanding the solutions required for PEC hydrogen generation. The tuneable nature of the band gap is another

benefit, but not the complete picture. To be discussed further in Chapter 2, water splitting requires specific band positions in order to achieve the overall reaction.[76] GaN has these required band positions,[77,78] as does InGaN alloys up to a indium content of 50 %,[79] allowing a significant portion of sunlight to be absorbed, while effectively transferring energy into the water splitting reaction.

Despite being identified as a potential material for water splitting in 2005,[80] there has only been a limited number of groups investigating III-nitrides for water splitting. Difficulties in the growth of high quality indium gallium nitride[71] mean alternative methods are required to achieve high efficiency devices. The commercial outlook of III-nitrides for a wide variety of applications, mean that economic prospects and quality is continuously progressing. The ideal band positions and tuneable band gaps indicate the strong potential for solar applications. There is therefore a great opportunity to exploit this material for renewable technologies to reduce global carbon emissions.

Bibliography

[1] A.S. Goudie, *The Human Impact on the Natural Environment: Past, Present, and Future*, Seventh (Wiley, Chichester, 2013).

[2] A. Mikkelsen and O. Langhelle, *Arctic Oil and Gas Sustainability At Risk?* (Routledge, Abingdon, 2008).

[3] M. Landon, *Environment, Health And Sustainable Development*, Illustrate (McGraw-Hill Education, New York, 2006).

[4] F. Harris, *Global Environmental Issues*, Second (Wiley, Chichester, 2012).

[5] K.C. Kim and R.D. Weaver, *Biodiversity and Landscapes: A Paradox of Humanity*, Illustrate (Cambridge University Press, Cambridge, 1994).

[6] R. Lee, S. The, E. Perspectives, and N. Autumn, *J. Econ. Perspect.* **17**, 167 (2003).

[7] P.M. Vitousek, H.A. Mooney, J. Lubchenco, and J.M. Melillo, *Science* **277**, 494 (1997).

[8] D. of E. and S.A. United Nations, *World Population Prospects The 2010 Revision* (New York, 2011).

[9] U. Cubasch, D. Wuebbles, D. Chen, M.C. Facchini, D. Frame, N. Mahowald, and J.-G. Winther, in *Clim. Chang. 2013 Phys. Sci. Basis. Contrib. Work. Gr. I to Fifth Assess. Rep. Intergov. Panel Clim. Chang.*, edited by T.F. Stocker, D. Qin, G.-K. Plattner, M. Tignor, S.K. Allen, J. Boschung, A. Nauels, Y. Xia, V. Bex, and P.M. Midgley (Cambridge University Press, Cambridge, 2013), pp. 119–158.

[10] R.J. Nicholls and A. Cazenave, *Science* **328**, 1517 (2010).

[11] D.L. Hartmann, A.M.G.K. Tank, M. Rusticucci, L.V. Alexander, S. Brönnimann, Y. Charabi, F.J. Dentener, E.J. Dlugokencky, D.R. Easterling, A. Kaplan, B.J. Soden, P.W. Thorne, M. Wild, and P.M. Zhai, in *Clim. Chang. 2013 Phys. Sci. Basis. Contrib. Work. Gr. I to Fifth Assess. Rep. Intergov. Panel Clim. Chang.*, edited by T.F. Stocker, D. Qin, G.-K. Plattner, M. Tignor, S.K. Allen, J. Boschung, A. Nauels, Y. Xia, V. Bex, and P.M. Midgley (Cambridge University Press, Cambridge, 2013), pp. 159–254.

[12] M.G.J. den Elzen. and M. Meinshausen, *Meeting the EU 2°C Climate Target: Global and Regional Emission Implications* (AH Bilthoven, 2005), pp. 1–44.

[13] G. Resch, A. Held, T. Faber, C. Panzer, F. Toro, and R. Haas, *Energy Policy* **36**, 4048 (2008).

[14] H.-D. Haustein and E. Neuwirth, *Technol. Forecast. Soc. Change* **22**, 53 (1982).

[15] T.C. Bond, E. Bhardwaj, R. Dong, R. Jogani, S. Jung, C. Roden, D.G. Streets, and N.M. Trautmann, *Global Biogeochem. Cycles* **21**, 1 (2007).

[16] REN21, *Renewables 2014 Global Status Report* (Paris, 2014).

[17] E. Worrell, L. Bernstein, J. Roy, L. Price, and J. Harnisch, *Energy Effic.* **2**, 109 (2008).

[18] H. Bulkeley and K. Kern, *Urban Stud.* **43**, 2237 (2006).

[19] J.D. Figueroa, T. Fout, S. Plasynski, H. McIlvried, and R.D. Srivastava, *Int. J. Greenh. Gas Control* **2**, 9 (2008).

[20] D. Victor, D. Zhou, E.H.M. Ahmed, P.K. Dadhich, J. Olivier, H.-H. Rogner, K. Sheikho, M. Yamaguchi, G. Baiocchi, Y. Mulugetta, and L. Wong, in *Clim. Chang. 2014 Mitig. Clim. Chang. Contrib. Work. Gr. III to Fifth Assess. Rep. Intergov. Panel Clim. Chang.*, edited by A. Grubler and A. Muvundika (Cambridge University Press, Cambridge, 2014), pp. 1–63.

[21] S. Kobayashi, S. Plotkin, and S.K. Ribeiro, *Energy Effic.* **2**, 125 (2009).

[22] C. Winter, *Int. J. Hydrogen Energy* **30**, 1371 (2005).

[23] F.H. Sobrino, C.R. Monroy, and J.L.H. Pérez, *Renew. Sustain. Energy Rev.* **14**, 772 (2010).

[24] S. Steinhilber, P. Wells, and S. Thankappan, *Energy Policy* **60**, 531 (2013).

[25] S. Carley, R.M. Krause, B.W. Lane, and J.D. Graham, *Transp. Res. Part D Transp. Environ.* **18**, 39 (2013).

[26] R.K. Ahluwalia, X. Wang, a Rousseau, and R. Kumar, *J. Power Sources* **130**, 192 (2004).

[27] C. Vlek and L. Steg, *J. Soc. Issues* **63**, 1 (2007).

[28] R. Shinnar, *Technol. Soc.* **25**, 455 (2003).

[29] C. Winter, *Int. J. Hydrogen Energy* **30**, 681 (2005).

[30] M.H. Maack and J.B. Skulason, *J. Clean. Prod.* **14**, 52 (2006).

[31] M. Ball and M. Wietschel, *Int. J. Hydrogen Energy* **34**, 615 (2009).

[32] R. Chaubey, S. Sahu, O.O. James, and S. Maity, *Renew. Sustain. Energy Rev.* **23**, 443 (2013).

[33] T. Abbasi and S. a. Abbasi, *Renew. Sustain. Energy Rev.* **15**, 3034 (2011).

[34] N.S. Lewis and D.G. Nocera, *Proc. Natl. Acad. Sci. U. S. A.* **103**, 15729 (2006).

[35] M.A. Green, K. Emery, Y. Hishikawa, W. Warta, and E.D. Dunlop, *Prog. Photovoltaics Res. Appl.* **22**, 1 (2014).

[36] G.R. Timilsina, L. Kurdgelashvili, and P. a. Narbel, *Renew. Sustain. Energy Rev.* **16**, 449 (2012).

[37] S.K. Mazloomi and N. Sulaiman, *Renew. Sustain. Energy Rev.* **16**, 4257 (2012).

[38] E. Bozoglan, A. Midilli, and A. Hepbasli, *Energy* **46**, 85 (2012).

[39] A. Bahadar and M. Bilal Khan, *Renew. Sustain. Energy Rev.* **27**, 128 (2013).

[40] A. Ley and D. Mauzerall, *Biochim. Biophys. Acta (BBA)-Bioenergetics* **680**, 95 (1982).

[41] V. Shah, N. Garg, and D. Madamwar, *FEMS Microbiol. Lett.* **194**, 71 (2001).

[42] J.D. Holladay, J. Hu, D.L. King, and Y. Wang, *Catal. Today* **139**, 244 (2009).

[43] J. Turner, G. Sverdrup, M.K. Mann, P. Maness, B. Kroposki, M. Ghirardi, R.J. Evans, and D. Blake, *Int. J. Energy Res.* **32**, 379 (2008).

[44] A. Fujishima and K. Honda, *Nature* **238**, 37 (1972).

[45] T. Bak, J. Nowotny, M. Rekas, and C. Sorrell, *Int. J. Hydrogen Energy* **27**, 991 (2002).

[46] Y. Du, Y. Feng, Y. Qu, J. Liu, N. Ren, and H. Liu, *Environ. Sci. Technol.* (2014).

[47] B. Kumar, M. Llorente, J. Froehlich, T. Dang, A. Sathrum, and C.P. Kubiak, *Annu. Rev. Phys. Chem.* **63**, 541 (2012).

[48] K. Kim, P. A. Graf, and W.B. Jones, *J. Comput. Phys.* **208**, 735 (2005).

[49] Z. Chen, T.F. Jaramillo, T.G. Deutsch, A. Kleiman-Shwarsctein, A.J. Forman, N. Gaillard, R. Garland, K. Takanabe, C. Heske, M. Sunkara, E.W. McFarland, K. Domen, E.L. Miller, J. a. Turner, and H.N. Dinh, *J. Mater. Res.* **25**, 3 (2011).

[50] G. Marbán and T. Valdés-Solís, *Int. J. Hydrogen Energy* **32**, 1625 (2007).

[51] S. Blanchette, *Energy Policy* **36**, 522 (2008).

[52] J. Hetland and G. Mulder, *Int. J. Hydrogen Energy* **32**, 736 (2007).

[53] F. Fichter, *Zeitschrift Für Anorg. Chemie* **54**, 322 (1907).

[54] F. Fischer and F. Schröter, *Berichte Der Dtsch. Chem. Gesellschaft* **43**, 1465 (1910).

[55] W.C. Johnson, J.B. Parson, and M.C. Crew, *J. Phys. Chem.* **36**, 2651 (1932).

[56] O. Ambacher, *J. Phys. D. Appl. Phys.* **31**, 2653 (1998).

[57] H.P. Maruska, *Appl. Phys. Lett.* **15**, 327 (1969).

[58] H. Amano, N. Sawaki, I. Akasaki, and Y. Toyoda, *Appl. Phys. Lett.* **48**, 353 (1986).

[59] I. Akasaki, *J. Cryst. Growth* **195**, 248 (1998).

[60] H. Amano, I. Akasaki, T. Kozawa, K. Hiramatsu, N. Sawaki, K. Ikeda, and Y. Ishii, *J. Lumin.* **40-41**, 121 (1988).

[61] H. Amano, *J. Electrochem. Soc.* **137**, 1639 (1990).

[62] H. Amano, M. Kito, K. Hiramatsu, and I. Akasaki, *Jpn. J. Appl. Phys.* **28**, L2112 (1989).

[63] J.I. Pankove, *Mater. Sci. Eng. B* **61-62**, 305 (1999).

[64] N. Yoshimoto, T. Matsuoka, T. Sasaki, and a. Katsui, *Appl. Phys. Lett.* **59**, 2251 (1991).

[65] S. Nakamura and T. Mukai, *Jpn. J. Appl. Phys.* **31**, L1457 (1992).

[66] S. Nakamura, T. Mukai, and M. Senoh, *Appl. Phys. Lett.* **64**, 1687 (1994).

[67] H. Amano, *Jpn. J. Appl. Phys.* **52**, 050001 (2013).

[68] S. Nakamura and M.R. Krames, *Proc. IEEE* **101**, 2211 (2013).

[69] S.P. DenBaars, D. Feezell, K. Kelchner, S. Pimputkar, C.-C. Pan, C.-C. Yen, S. Tanaka, Y. Zhao, N. Pfaff, R. Farrell, M. Iza, S. Keller, U. Mishra, J.S. Speck, and S. Nakamura, *Acta Mater.* **61**, 945 (2013).

[70] K. Tanabe, *Energies* **2**, 504 (2009).

[71] J. Wu, *J. Appl. Phys.* **106**, 011101 (2009).

[72] A. D. Vos, "*Endoreversible Thermodynamics of Solar Energy Conversion*" (Oxford University Press, 1992), p. 90.

[73] J. Wu, W. Walukiewicz, K.M. Yu, W. Shan, J.W. Ager, E.E. Haller, H. Lu, W.J. Schaff, W.K. Metzger, and S. Kurtz, *J. Appl. Phys.* **94**, 6477 (2003).

[74] W. Walukiewicz, *Future Prospects of Semiconductor Materials for Solar and Photoelectrochemical Cells*, LBNL Workshop, March 28-29, Berkeley, California, USA (2005).

[75] S. Strite and H. Morkoç, *J. Vac. Sci. Technol. B Microelectron. Nanom. Struct.* **10**, 1237 (1992).

[76] T. Hisatomi, J. Kubota, and K. Domen, *Chem. Soc. Rev.* (2014).

[77] J.W. Ager III, J. Wu, K.M. Yu, R.E. Jones, S.X. Li, W. Walukiewicz, E.E. Haller, H. Lu, and W.J. Schaff, in *Fourth Int. Conf. Solid State Light.*, edited by I.T. Ferguson, N. Narendran, S.P. DenBaars, and J.C. Carrano (2004), pp. 308–315.

[78] I.M. Huygens, K. Strubbe, and W.P. Gomes, *J. Electrochem. Soc.* **147**, 1797 (2000).

[79] P.G. Moses and C.G. Van de Walle, *Appl. Phys. Lett.* **96**, 021908 (2010).

[80] K. Fujii, T. Karasawa, and K. Ohkawa, *Jpn. J. Appl. Phys.* **44**, L543 (2005).

Chapter 2

Background

A general theory of the various areas of science are presented from basic semiconductor physics through to a focus of photoelectrochemical water splitting. It serves as an introduction into each research topic with more specific information provided in the subsequent result chapters.

2.1 Semiconductors

Semiconductors are a class of materials whose electrical conductivity is between metals and insulators and can be composed of atomic elements, inorganic compounds, such as GaAs, or organic materials. The resistivity of semiconductors is at a value between 10^{4} and 10^{-10} Ωcm[1]. Inorganic semiconductors are typically bonded via covalent bonds. The covalent nature arises due to a sharing of electrons, either between heterogeneous (GaN, Fe_2O_3) or homogeneous (Si, Ge, C) species. Elements are comprised of electrons, neutrons and protons. While the protons and neutrons reside in the nucleus, the electrons form discrete energy bands around the nucleus, known as orbitals. Each orbital can hold a maximum number of degenerate electrons specific to the orbital type. In increasing energy the orbitals are the s (2), p (6), d (10), f (14), g (18) and h (22) with the number of electrons identified in parenthesis. No currently discovered element has ground state

electrons in the g or h orbitals. For the majority of semiconductor materials, it is the s, p and d orbitals that are of concern. The energetically favourable state for atoms is to have a completely filled outer orbital. Taking silicon as an example, there are a total of 14 electrons within atomic silicon. These electrons sit in the 1s (2), 2s (2), 2p (6), 3s (2) and 3p (2) orbitals. From this it is clear that the 3p orbital contains only 2 of the required 6 electrons. In order to satisfy a filled orbital, 4 further electrons are required. This occurs via the formation of covalent bonds in which atomic silicon shares electrons with other silicon atoms, in order to have a total of 8 electrons in the outer orbital. The nature of the bonding across the semiconductor material class varies to some degree. The extent of covalent (shared electrons) and ionic (donor/acceptor electrons) bonding changes across the group which ultimately alters the material properties.[2]

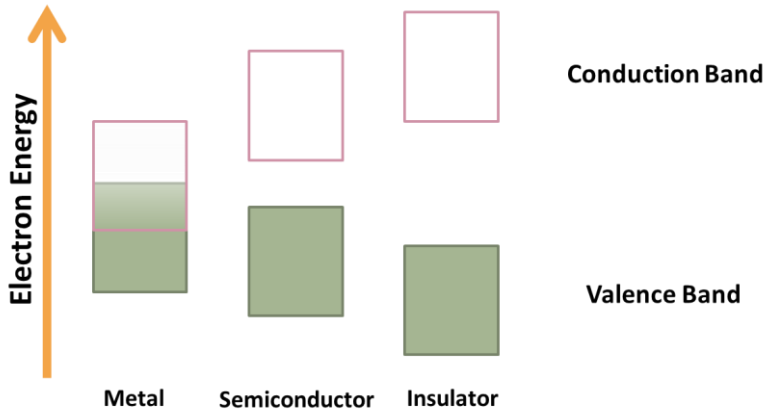

Figure 2-1 – Illustration of metal, semiconductor and insulator band structures

Due to the Pauli Exclusion Principle, it is only possible to have a maximum of two electrons (of opposite spin) with the same discrete energy level in a system. Therefore, when *n* atoms are brought together, *n* energy bands are formed. The formed energy states are allowed positions for the electrons to exist. Between these positions lie forbidden regions in which electrons are not allowed to occupy. The conduction of semiconductors is derived from the formation of these energy bands. At 0 K, electrons are in the first allowed energy band, the valence band, while no electrons are present in the conduction band, similar to that of an insulator (Figure 2-1). In

contrast, in a metal, the empty conduction band overlaps the valence band and therefore in a sense, there is one partially filled band (Figure 2-1). In order for conduction to occur, a band can neither be completely filled or empty. Therefore, generally speaking, metals have the ability to conduct at any temperature as a result of the available allowed energy states. Unlike insulators, in which the gap between the bands is sufficiently large to prevent promotion, an input of energy to a semiconductor will excite electrons from the valence band to the conduction band. The difference between the valence and conduction band is known as the band gap, which is a fundamental parameter to describe semiconductors.

The band gap of a semiconductor material can either be direct or indirect (Figure 2-2). In direct band gap semiconductors, both the valence band maximum and the conduction band minimum are at the same momentum. For indirect gap semiconductors, the conduction minimum is at a different momentum value (Figure 2-2),[3] where the recombination of electrons and holes will only take place via another kind of particle (phonons). The nature of a semiconductor, whether direct or indirect, results in interesting properties in regards to recombination and ultimately its applications.

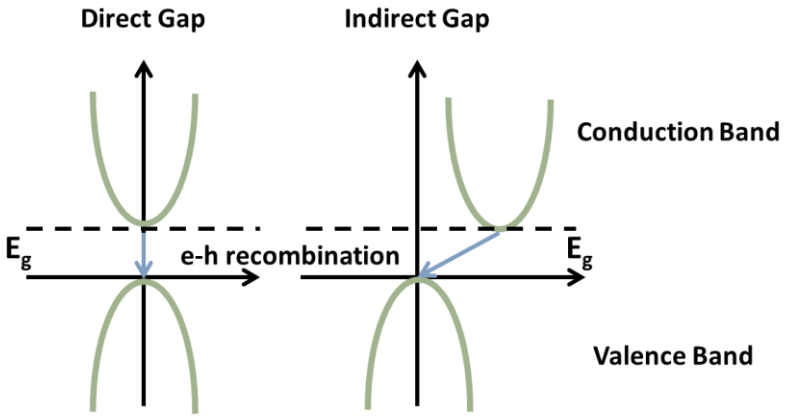

Figure 2-2 – Representation of direct and indirect band structures on energy-momentum diagrams

Conduction in semiconductors can therefore occur due to the creation of partially filled band states. When an electron is excited from the valence band into the conduction band, it leaves behind an empty electron

state known as a hole. In intrinsic semiconductors (undoped) there exist a similar number of electrons in the conduction band as there are holes in the valence band due to thermal excitation at room temperature. Another property of semiconductors is their ability to be doped by additional materials. Doped semiconductors can have an excess of electrons or holes depending on the dopant. Replacing one atom in the crystal structure with one of higher or lower outer orbital electron, results in an almost free electron or hole in the device respectively. Doping materials will create an *n*-type or *p*-type semiconductor depending on whether there are additional electrons (*n*-type) or holes in the crystal structure (*p*-type). In order to describe semiconductors fully, another important concept needs to be introduced, namely the Fermi level (E_F). In an intrinsic semiconductor, the Fermi level is in about the centre of the forbidden region. Deviation from this point within the forbidden region depends on the effective mass of electrons and holes. Generally speaking, for *n*-doped semiconductors, the Fermi level rises to a level close to the conduction band while for *p*-type it falls to a level close to the valence band.

2.1.1 Conduction, Mobility and Recombination

As stated, electrons and holes are responsible for the conduction in semiconductor materials. There are two mechanisms behind this process, drift and diffusion. Drift is the result of an electric field acting on the carriers, while diffusion is caused by a concentration gradient. The influence of drift is controlled via the strength of the electric field exerted on the electrons and holes. The drift velocity of a semiconductor is a product of the electric field (E) and the mobility (μ), in which mobility is the measure of carriers' ability to move.[4] There are a number of scattering mechanisms, which will limit a further increase in velocity with an increase in the applied electric field. This is potentially through defects and collective vibrations of lattice atoms, due to thermal energy, which can be described in the form of phonons. As a result of these limits, a saturation level is reached, which is called the saturation velocity and is dependent on the material.[5]

In a typical semiconductor device under operation, an electric field and concentration gradient will exist. The total current is therefore determined by both drift and diffusion. A change in carriers away from equilibrium is ultimately only temporary. In regards to semiconductors, the relaxation back to equilibrium conditions occurs via a process known as recombination. The generated electron and hole pairs recombine, returning back to the undisturbed state. Recombination is controlled in part by the diffusion length of the carriers. Upon injection, in doped semiconductors, the majority carrier concentration changes by an insignificant amount but there is a drastic change in minority carriers. Therefore the minority carriers dominate and the recombination rate is proportional to the population and lifetime of these carriers.[6] As discussed, carriers after injection will move via diffusion principles, combination with a lifetime, results in the carriers having a specific diffusion length. This property plays a crucial role in semiconductor device efficiencies.

There are a number of mechanisms that affect recombination and these can be material dependent.[5] Recombination via the emission of a photon is known as radiative recombination which can occur via various mechanisms (Figure 2-4). As illustrated in Figure 2-4, process i-ii indicates the excitation of an electron into the conduction band, rapid thermalisation and then recombination. In process iii, a free exciton or impurity bound exciton decays into the valence band. Processes iv-vi indicate the presence of neutral states within the material, either acceptor or donor states, in which transitions can occur.[7] These donor states may be present due to doping within the semiconductor. Not all recombination processes proceed via photon emission and nonradiative processes occur via three dominant mechanisms, transformation into heat, creation of defects and photochemical changes of the material.[8] The presence of nonradiative pathways can result in a decreased efficiency of a semiconductor device. Nonradiative recombination can occur via the presence of trap states between the conduction and valence bands due to defects or impurities (Shockley-Read-Hall) or via an Auger process.[9] Auger processes involve the

transmission in the recombination energy to another electron or hole, resulting in a change to the kinetic energy of the system. It is a particularly important aspect in regards to light emitting diodes due to high carrier densities.

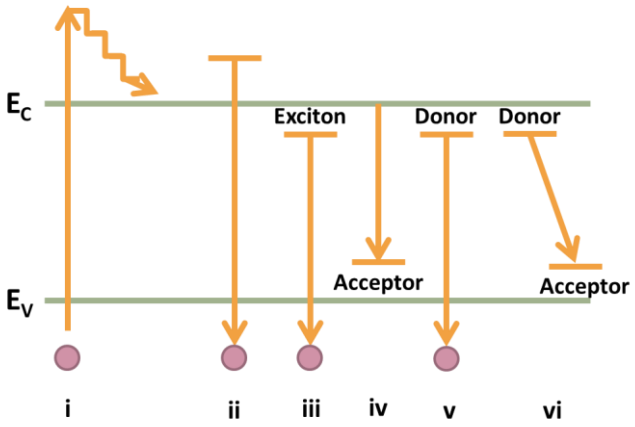

Figure 2-4 – Radiative recombination mechanisms in semiconductors[7]

2.1.3 Optical Properties

Electromagnetic radiation in the form of light is both an interesting feature of semiconductors as well as a useful diagnostic tool.[10] Spectroscopic techniques can provide information regarding the band gap of the semiconductor due to the radiative recombination processes occurring within the material. When a semiconductor is illuminated, a number of processes occur at the interface. Some of the incident radiation will be reflected and the rest transmitted through the sample. Unlike metals, the reduced number of free energy carriers in semiconductors means that until the incident wavelength is larger than the semiconductor band gap, no significant absorption occurs.[5] Therefore, via the use of absorption spectroscopy, information can be inferred regarding the band gap of the material due to the absorption or transmission level of each defined wavelengths.

During optical injection, when carriers recombine, the emitted radiation as photons is known as photoluminescence. Photoluminescence can occur via two mechanisms, fluorescence and phosphorescence and is a significant process in semiconductors. Fluorescence is a direct energy

transfer from singlet states, while phosphorescence involves an intermediary step in which the energy is transferred into a forbidden energy state. As a result of the differences in energy transfer routes, fluorescence is typically a very fast process dependent on band structure and whether it is stimulated or spontaneous emission, while phosphorescence can last for significantly longer periods after the initial injection.[5] Photoluminescence spectroscopy (PL) is the study of the radiative recombination processes (Figure 2-4) via the excitation of carriers using light and is a common diagnostic tool for semiconductors.

Alternative methods of injection involve the use of high energy electron beams or electric currents. The processes in which the energy causes light emission are known as cathodoluminescence and electroluminescence respectively.[5] Each spectroscopic technique provides an insight into the described recombination processes and through advanced techniques, such as time resolved photoluminescence, information regarding rates of decay can be investigated. The specific techniques implemented in this thesis will be described in further detail in the experimental section to provide relevant and useful information pertaining to the theory and method.

2.1.4 Semiconductor-Metal Interface

As discussed, it is possible to inject carriers into a semiconductor via a metal. When a metal and semiconductor are brought into contact, there are a number of material properties that are required to be considered. The work function (Ø) of the material is a critical property in determining whether the metal-semiconductor interface will be ohmic or Schottky.[11] The work function, as depicted in Figure 2-5 is the minimum amount of energy required to take an electron from a solid into the vacuum. If $Ø_M > Ø_S$ a potential barrier is created when the metal and semiconductor are brought into contact. This occurs as the Fermi levels are required to be in coincidence forcing the semiconductor valence and conduction bands to bend upwards. When the work function of the semiconductor is larger than that of the metal, the conduction bands bend downwards (Figure 2-5),

removing the barrier, allowing current flow in either direction, thus creating an ohmic contact.[12]

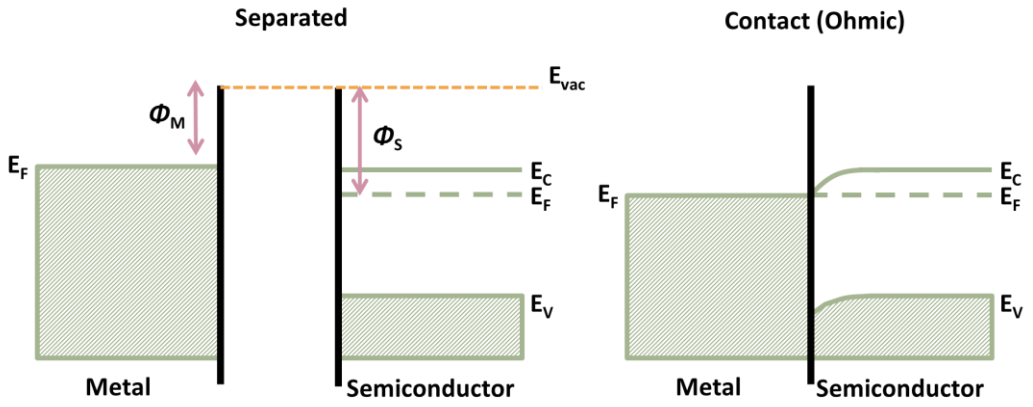

Figure 2-5 – Schematic representation of metal-semiconductor (*n*-type) band structures when separated and in intimate ohmic contact

2.2 III-Nitride Semiconductors

The III-nitride semiconductor family is comprised of Ga, In and AlN with ternary and quaternary structures also available.[13] These are all of a direct band gap structure, with their band gaps covering a wide spectral region from deep UV (~200 nm) through to infrared (1770nm), including the complete visible part of solar spectrum. III-nitrides could therefore potentially be the best candidates for the fabrication of high performance optoelectronics for future energy saving applications. This can include solar energy applications, use in solid state lighting to replace general illumination lighting sources and solar hydrogen generation. The pioneering work of Akasaki and Nakamura the in late 1980s[14,15] and early 1990s[16] has resulted in GaN and its alloys to become established as the industry's preferred semiconductor materials for short-wavelength emitters over the last two decades.[17,18] The major achievements are however limited to violet/blue emitters. Furthermore, there still exist a number of scientific and technological challenges, limiting their potentially overwhelming advantages, to be explored. Typical examples of this are within solar applications where the energy efficiency of III-nitride devices is far behind the theoretical predictions.

2.2.1 Structural Properties

The III-nitrides can form a *wurtzite*, *zinc blende* or *rock salt* crystal structure (Figure 2-6), with *wurtzite* the thermodynamically stable structure under ambient conditions. The cubic *zinc blende* structure has been grown with the aid of cubic substrates to overcome the thermodynamic tendency to form the hexagonal *wurtzite* structure.[13] The stability of the *wurtzite* structure is thought to arise from the electrostatic interactions between the anions and cations (dashed lines Figure 2-6 (b)) as a result of the ionicity of the III-nitrides.[19] As discussed previously, the bonding within semiconductors is typically covalent in nature. However, if the electronegativity of the two bonding species is significantly different, a degree of ionicity in the bonding can arise. In this case, a dipole moment may form resulting in a more donation-acceptance nature of the bond. This is true for the III-nitrides in which the electrons are typically found around the nitrogen atoms.[20] Due to these properties, under high pressures, the ionic nature wins out and results in the phase transition to the rock salt structure (Figure 2-6 (c)).[13]

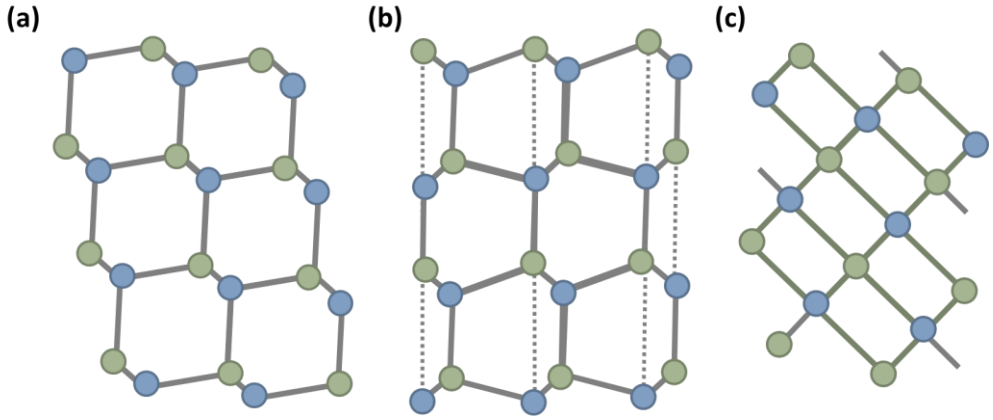

Figure 2-6 – Atomic structures of different crystal structures (a) *zinc blende* (b) *wurtzite* (c) *rock salt*

The structural properties of the III-nitrides such as the lattice constant and thermal requirements for growth have resulted in difficulty in finding suitable growth substrates. The high temperature required for epitaxial growth has resulted in the wide spread use of sapphire as the growth substrate, however due to the differences in thermal expansion coefficients and the lattice mismatch of the materials, typical films of III-nitrides are liable

to a level of strain.[21] Recently, silicon as a substrate for epitaxial growth of GaN is developing due to the complimentary applications, however the issue of strain is an even more severe issue than for growth on sapphire, which is leading to massive cracking of the epitaxial layers.[22]

2.2.2 Band Gaps

The III-nitride semiconductors have direct band gaps that range from 0.7 eV up to 6.2 eV making them applicable to a wide range of applications. The initial belief was that InN had a band gap of 1.9 eV, instead of the actual 0.7 eV, due to the difficulty in growing high quality samples and this resulted in confusion over the band structures of the alloys of indium as well.[23] The band gap of GaN was found to be 3.5 eV for the *wurtzite* structure however this changes slightly for *zinc blende* GaN as a result of symmetry differences.[23] For AlN the room temperature obtained band gap for a high quality sample has a value of 6.2 eV.[21] With any mix of III-nitride materials possible, semiconductors with direct band gaps of 0.7 eV through to 6.2 eV are feasible. Detailed band structures have been investigated for each of the nitrides exploring the specific nature of the electronic transitions that arise.[23] The band gaps of the III-nitrides all show a degree of temperature dependence which can be expressed by the Varshni formula (Equation 2-1).[19]

$$E_g(T) = E_g(0) - \frac{\alpha T^2}{T + \beta}$$

Equation 2-1 – Varshni formula for band gap variation with temperature where α and β are material specific parameters

2.2.3 Growth

As stated in the introduction, there were a number of breakthroughs in growth technology that has allowed the commercial use of III-nitrides. Due to lack of native substrates, III-nitrides are generally epitaxially grown on foreign substrates, predominantly on sapphire.[24] Due to the extremely large lattice-mismatch between GaN and sapphire (up to 16%), III-nitride growth remains a significant challenge. Despite this there have been developments in regards to growth techniques on alternative substrates, such as Si, SiC, AlN and GaN.

The typical growth technique of the III-nitrides is via metal organic chemical vapour deposition (MOCVD). This is a technique that allows the deposition of controlled films onto a growth substrate resulting in the formation of the semiconductor crystal. MOCVD uses chemical feedstock as the source of the semiconductor molecules. High quality reactants are vaporised and injected into the reactor where the specific growth conditions have been set. This includes the growth temperature, flow rates of reactants and reactor pressure. The injected reactants are elevated to decomposition temperatures by the susceptor which results in the formation of thin films of the desired compound semiconductor.[25]

For growth of III-nitrides, the traditional reactant gases or precursors are trimethyl- variants ($(CH_3)_3M$ where M=In, Al, Ga) and ammonia (NH_3).[26] The deposition process can then proceed via the elimination of alkane radicals upon heating. The growth temperature of each III-nitride varies and is one reason for the difficulty in growing high quality InN. For InGaN, a value in excess of 600 °C is commonly utilised while GaN and AlN require temperatures of at least 1000 °C.[26] The ratio of the III/V elements is also a crucial factor in controlling the growth with high ratios used in the growth of GaN. The initial problems in growing GaN were overcome via the implementation of a low temperature AlN (and later GaN) buffer layer with a typical thickness of 25 nm,[14] on the sapphire substrate prior to the GaN growth. The growth layer has to be accurately controlled in order to result in the observed improvements in surface roughness which paved the way for the growth of *p*-type GaN. This resulted from the generation of nucleation sites of the thin AlN which aided the directionally controlled growth of the subsequent GaN layer. Our group has developed a technique using a high temperature AlN buffer,[27] which can further improve the crystal quality of GaN and also eliminate the strict requirements for the thickness of the nucleation layer in the two-step approach.

Further improvement in crystal quality of GaN can be obtained by means of epitaxial lateral overgrowth (ELOG) and the techniques evolved from ELOG overgrowth techniques,[26] where a complicated ex-situ mask

patterning process is involved.[28] Overgrowth techniques are based on selective area growth, and require the use of a dielectric mask such as SiO_2 or Si_3N_4 via ex-situ processes, which is patterned into stripes on a micro meter scale using a standard photolithography.[29] The dislocations under the mask stripes, caused by the large lattice-mismatch are effectively blocked. However, it potentially causes no*n*-uniformity issues and an atomically flat surface cannot be obtained till the overgrown layer is 10-20 μm thick. As a result there are still issues to be addressed for wide scale application of this technique. The advances that have been made in the growth of III-nitrides have resulted in the ability to grow larger higher quality wafers for various applications improving their commercial applications.[30]

Doping

Presently, nominally undoped GaN exhibits *n*-type characteristics with a typical background carrier concentration in the region of 10^{16} cm^{-3}. As a result of the existence of a large number of defects such as Ga or N vacancies, dislocations arise with a typical of density of 10^8-10^9 cm^{-3}. For the generation of *n*-type GaN, an additional electron is required, either via the replacement of a nitrogen or gallium site in the lattice. Silicon is the dopant of choice due to the level of control it provides over the final carrier concentration.[31] The silicon replaces Ga sites in the lattice, adding the required electron for *n*-type materials making it possible to dope the ternary nitride alloys of AlGaN and InGaN. Doping of the material is controlled by altering the flow of silane (SiH_4) during MOCVD growth.

Unlike *n*-type GaN, the growth of *p*-type GaN proved difficult as the majority of potential acceptor materials were all deep level acceptors preventing the growth of a conducting *p*-type material.[32] Substitution of gallium sites with divalent magnesium, via biscyclopentadienyl magnesium (CP_2Mg), provides good control over the dopant level. However, the magnesium is typically required to be activated due to the presence of H_2 in the reactor, which forms Mg-H complexes leading to passivation of the material. Activation was initially found via the use of an electron beam[33] and later in the early 1990s Nakamura developed an annealing process in a high

temperature N_2 atmosphere. [34] The high energy process causes the Mg-H complex to break and removes the H^+ preventing further formation of the complex. The breakthrough based on the simple but cost-effective technology represents a milestone in the fields of III-nitrides, which laid a solid foundation for the current III-nitride industry.

2.2.4 III-nitride Devices

Semiconductor based optoelectronics,[30,32,35,36] in particular, LEDs or LDs, generally consist of *n*-type regions, an active emitting region and *p*-type regions. Low dimension structures, such as quantum well or quantum dots, are generally used as the emitting region. Furthermore, correct metals need to be selected in order to form good ohmic contacts on the devices.

Quantum Wells

For III-nitride devices, quantum well (QW) structures are commonly utilised.[21,37–40] A two-dimensional dimensional quantum well structure, are a typical double heterostructure which consists of a thin layer with a low band gap material as a quantum well sandwiched between two layers of larger band gap material that serve as barriers.[41] The quantum well thickness needs to be smaller than the de Broglie wavelength of the material, leading to the generation of a two-dimensional quantum confinement effect along the growth direction, for simplicity, denoted as Z direction.

The quantum confinement effect leads to the generation of a number of extra discontinuous energy levels in both valence and conduction bands as shown in Figure 2-7 (a). This is dependent on the discontinuity of the band gaps of quantum well and barrier which is denoted as the band-offset. Accordingly, these extra energies are quantization energies, which can be tuned by modifying the quantum well thickness. The optical transitions between the sub bands in the conduction and valence band must follow a selection rule, namely, $\Delta n=0, \pm2, \pm4, ...$, where Δn is the difference of the sub band indices. In bulk material, vertical transitions conserve the momentum but can have different energies. This results in the optical absorption being related to the density of states, following a rise with the square root of

energy.[36] For quantum wells the density of states for i*n*-plane motion is constant with energy, resulting in the formation of steps, therefore the optical absorption in keeping with the density of states, occurs stepwise for each quantum number (Figure 2-7(b)).[10]

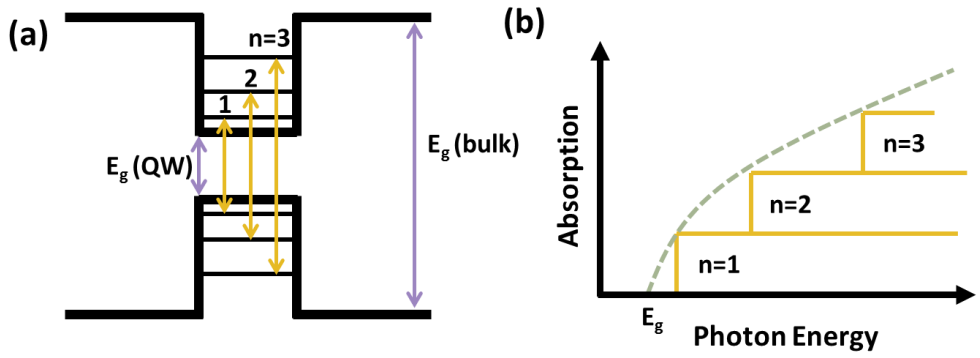

Figure 2-7 – (a) Simple model of optical absorption in quantum wells (b) density of states for a bulk (dashed) and quantum well semiconductor

InGaN quantum wells have been widely used as an emitting region in the growth and fabrication of visible emitters. Although a number of major achievements have been made within the last two decades, there are still a number of challenges in regards to both the science and technology of the devices. It is currently difficult to incorporate high levels indium into GaN in order to form InGaN with emission towards green, yellow, or even longer wavelengths.[42] Currently, reducing the growth temperature for InGaN has been widely used in order to enhance indium incorporation, but it leads to a severe degradation in crystal quality of InGaN layer. As a result of the large lattice-mismatch between InGaN and GaN when forming InGaN/GaN quantum well structures on the widely used c-plane sapphire substrates, piezoelectric fields are generated across the quantum wells, leading to the modification of band diagram as shown Figure 2-8 (a). As a result, the devices using InGaN/GaN MQW as an emitting region, suffer from reduced overlap between the electron and hole wave functions and thus a long radiative recombination time. This results in a low quantum efficiency, a concept known as the quantum confined Stark effect (QCSE). This becomes a severe issue when the emitters move towards the green spectral region, as a much higher InN fraction is required and the internal electric fields become

extremely high. Growth on non-polar or semi-polar substrates are being utilised to combat this issue. In nonpolar material, there is no deformation of the bands or wave function (Figure 2-8 (b)). The great challenge arises with the crystal quality of non-polar or semi-polar GaN which is currently far behind that of c-plane GaN.

For the fabrication of devices for solar energy related applications, a thick InGaN layer with high indium contents as an absorption region would be ideal. However, the critical thickness for the formation of misfit dislocations in InGaN on GaN surfaces is very limited and dependent on indium content.[43] The reports on the critical thickness of InGaN thickness are under debate due to the lack of high quality samples. It has been generally accepted that it would be less than 10 nm for InGaN with a 30-40% indium, corresponding to the major part of the solar spectrum. However, it is worth highlighting that the spatial separation of the electrons and holes is beneficial in solar application, as a long recombination time is requested for the solar device in order to enhance photocurrent. Therefore, traditional c-plane GaN with high indium content layers would be ideal for the fabrication of solar devices with improved efficiency due to the QCSE described in Figure 2-8 (a).

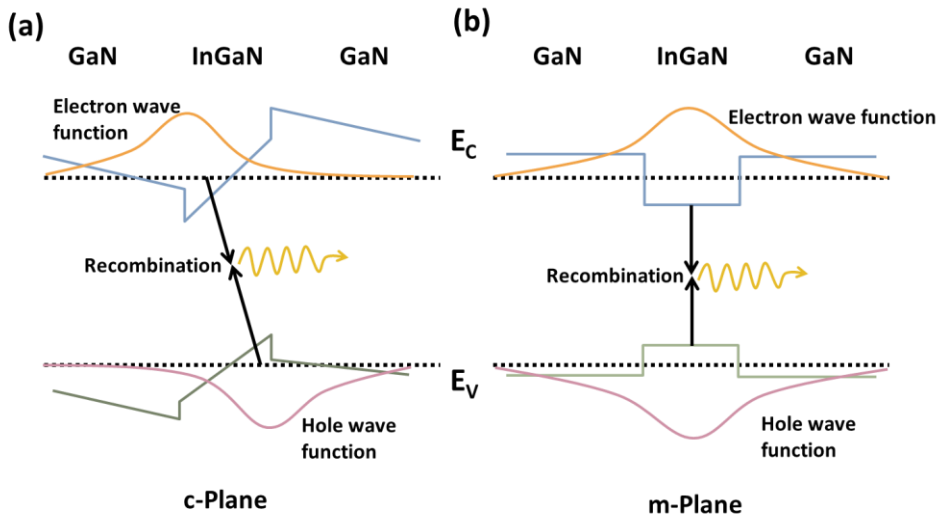

Figure 2-8 – Effect of polarization on quantum well band diagrams (a) polar c-plane GaN (b) nonpolar m-plane GaN[44]

Ohmic Contacts

As discussed, in order to achieve an ohmic contact to a semiconductor the work function of the metal has to be smaller than that of the semiconductor. The work function of GaN has been measured at 4.1 eV, therefore a metal is required to have a value lower than this in order to form an ohmic contact to *n*-type GaN.[45] Low-resistance ohmic contacts for both *n*- and *p*-type GaN took a considerable degree of time to identify, however since the beginning of the century a consensus seems to have been reached. For *n*-type GaN, contacts are typically comprised of a base layer of titanium which leads to a formation of a thin TiN layer.[46] The nature of the ohmic contact forms as a result of the increase in nitrogen vacancies at the interface increasing the localised dopant level of the GaN.[47] Good ohmic contacts have been demonstrated via the use of either Ti/Al/Ti/Au[48,49] or simply Ti/Au layers.[48,50,51] As discussed, *p*-type GaN proved difficult to grow due to the background doping of the material and the required activation of the dopants. Formation of a low resistance contact to *p*-type GaN also proved troublesome as a result of high activation energy above 150 meV (while that of *n*-GaN is less than 20 meV). A good ohmic contact can be achieved via the use of thin annealed Ni/Au films.[52] Annealing of the film results in the oxidation of the nickel to *p*-type NiO at the interface of the GaN allowing for better charge-transfer as a result of band alignment.[53]

2.3 Electrochemistry

In order to understand the principles that underpin solar hydrogen production it is important to have an understanding of electrochemistry. Electrochemistry itself is an area of science that focuses on the relationship of electrical and chemical reactions. Electrochemistry has been utilised widely in industry for many years in the creation of battery technologies and by laboratory scientists trying to gather thermodynamic information about their solutions.[54] Today, however it is a modern branch of chemistry in which the potential for the different applications as well as the understanding of processes has evolved significantly. The focus here will be to introduce key

principles, focusing towards photoelectrochemistry and the role that semiconductors have to play.

2.3.1 Electrochemical Reactions & Potentials

Reactions of an electrochemical nature involve the use of electrodes (electronic conductors) and an electrolyte (ionic conductor).[55] The interaction of the electrode and electrolyte at the interface is of significant importance. While for electrodes, electrons and holes are the charge carriers, between the electrodes, charge is transferred via ions in the electrolyte solution. The processes occurring within the electrode and electrolyte vary and therefore the interface between the two systems is relatively complex. The nature of the reactions that occur at each electrode is different and therefore it is important to look at the individual processes occurring in order to build the full picture of the reactions in the whole system.

A typical cell arrangement is of two electrodes and a single electrolyte solution. The reaction in the cell is comprised of half reactions. Each reaction occurs as a result of the potential differences at the interface of the electrode-electrolyte interface. The combination of the two reactions described the overall process in the cell.[56] In order to determine the potential required for the half reactions to occur, a standardised reference is utilised. The standard hydrogen electrode (SHE) is the base reaction in which all other electrochemical processes can be measured and is a theoretical process with a potential value of 0. Occasionally, reference electrodes which have a constant electrode-electrolyte interface are utilised, such as a saturated calomel electrode (SCE), which is comprised of a mercury, mercury chloride and potassium chloride solution. For ease of comparison, standard potentials ($E^{\ominus}$) versus the SHE will be utilised throughout this work.

The two half reactions involved in the reaction involve an oxidation and reduction process. If the electrode is only acting as an intermediary in the system, it will act as either a sink or source of electrons. Thus a reaction

proceeds via the electrolyte, in which species in the solution become either oxidised (electron loss) or reduced (electron gain). This is represented in Figure 2-9 in which the individual oxidation and reduction reactions are described. As illustrated, there is no net change in the charge of the system. Alternatively to the aforementioned process, the electrodes themselves may be involved in the reaction as a result of dissolution or corrosion. For hydrogen production this is a less than desirable effect.[57] At the interface of the electrode and electrolyte two distinct types of processes occur. These include the illustrated charge transfer mechanisms (Faradaic) and are proportional to the amount of current in the system as well as nonfaradaic processes.[55] Unlike their counterparts, no charge transfer is exhibited, however adsorption and desorption processes can occur ultimately changing the composition of the interface and the electroylte.[58] The nature of the interface between the electrode and electrolyte will be discussed in further detail later.

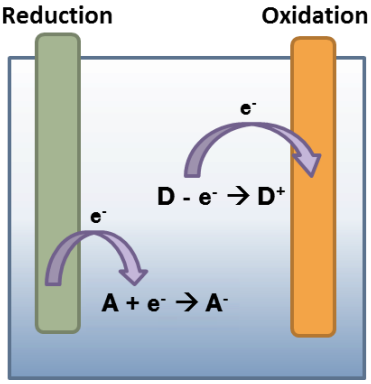

Figure 2-9 – Illustration of oxidation and reduction reactions occurring at electrode-electrolyte interface

The natures of the half reactions are dependent on the potential of the oxidation and reduction processes. The total potential of the cell is calculated from both reactions.[59] Considering an electrochemical cell with two electrodes of zinc and copper and an electrolyte containing both zinc and copper ions. The cell reaction is identified below (Equation 2-2).[59]

Overall: $Zn + Cu^{2+} \rightarrow Zn^{2+} + Cu$ $E^{\ominus}$ = +0.34 – (-0.76) = 1.10 V

Right: $Cu^{2+} + 2e^{-} \rightarrow Cu$ $E^{\ominus}$ = +0.34 V

Left: $Zn^{2+} + 2e^- \rightarrow Zn$ $E^{\ominus}$ = -0.76 V

Equation 2-2 – Illustration of simple electrochemical cell reaction with potentials

The total cell potential is derived from the difference in potential between the reduction potentials of the two species involved in the reaction. Two further equations are important in determining the potential of electrochemical reactions. The first relates the Gibbs free energy of the reaction to the cell potential,

$$\Delta G = -nFE_{cell}$$

Equation 2-3 – Gibbs free energy of electrochemical cell reactions

where n is the molar number of electrons required, F, the Faraday constant and E_{cell} the potential value of the reaction. Understanding the thermodynamic relationship of the cell reaction means that details of particular reactions can be derived from thermodynamic data.[60] The second equation is the Nernst equation (Equation 2-4), first derived in 1889,[61] which relates the potential of a cell to the activities of the species. A system that follows the Nernst equation is stated as being either electrochemically or thermodynamically reversible.[60] Once the principles behind the Nernst equation have been satisfied in relation to chemical potentials, satisfactory values for the energy of a cell can be obtained.[59]

$$E = E^{\ominus} + \frac{RT}{nF} ln \frac{a_O^{v_i}}{a_R^{v_i}}$$

Equation 2-4 – Nernst equation for relating electrode potential and concentration of reaction species[60]

2.3.2 Mass & Charge Transport

In order for the discussed electrochemical reactions to occur, a transfer of mass is required. Due to the properties of an electrochemical reaction and the components involved, the nature of the molecules within the reaction vessel varies. In a similar manner to the properties of charge transport in semiconductors, ions in electrolyte solutions are affected by concentration gradients and electric fields.[59] The velocity at which solvated ions move through the solution is dependent on both the charge and size of

the ion. Diffusion related transfer will occur for all species, while migration caused by an electric field will only affect particles of a charged nature. Small effects on particles with dipole moments are observed.

Diffusion of species will occur as a result of the concentration gradient present in the solution. During an electrochemical reaction, the nature of the species at the electrode-electrolyte interface will change. The concentration of the oxidised and reduced species will therefore alter creating a concentration gradient in the solution. As illustrated in Figure 2-10, species will transfer from the bulk solution towards the surface of the electrolyte. Further chemical reactions may occur prior to, or following, the electron transfer as well as the potential for surface effects.[55] As a result of the chemical reactions occurring at the electrode surface, the concentration of the starting material, O, will dominate at the bulk; migrate towards the electrode before being reduced into species R. Subsequently the concentration of the reduced species at the surface of the electrode will be relatively high and diffuse towards the bulk solution.[58] The rate of diffusion is dependent on the flux of the species and the concentration gradient, as described by Fick's law.[59]

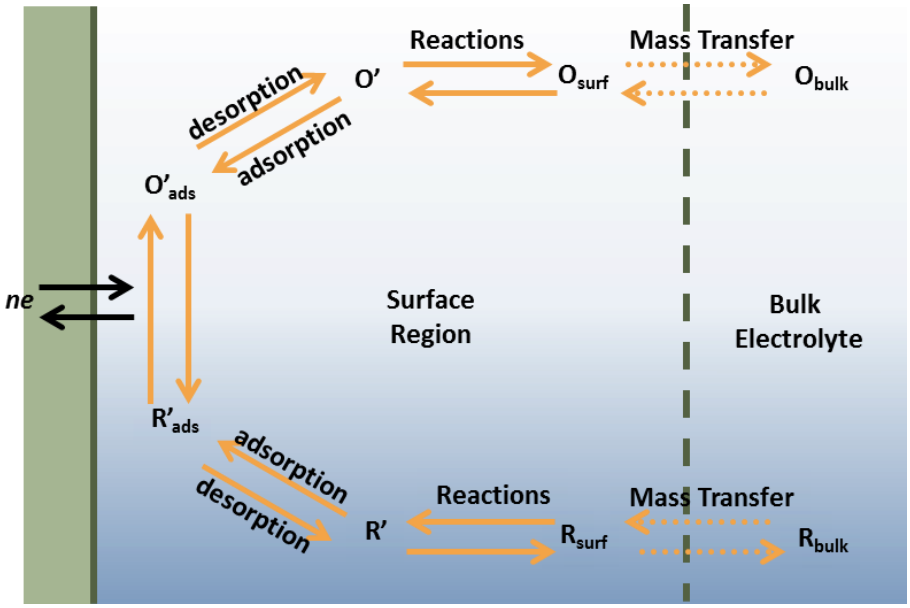

Figure 2-10 – General reaction pathway and mass transport between bulk solution and surface region of electrode. Adapted from Bard & Faulkner, 2001.[55]

The migration of charged particles as a result of a potential gradient accounts for carrying the majority of current in an electrochemical cell, as away from the electrode interface, concentration gradients are minimal.[62] However, migration is not essential for the transport of the electroactive species (species involved in reaction) as the charge can be carried by any ionic species. If a large excess of reaction independent electrolyte is added to the solution, this will carry the majority of the charge and therefore the only some of the electroactive species are transported by migration.[58] There are also three forces opposing the action of the electric charge. Due to solvation of ions a frictional force dependent on the ion size will retard the migration. Asymmetric and electrophoretic effects also act as a result in the distortion of the ionic atmosphere and contrary movement of solvent molecules respectively.[59] The conductivity of the system is therefore dependent on the ion concentration in the solution. Convection effects can also affect the movement of species in solution if stirrers are used in solution, thereby disrupting the natural balance of the system.[58]

Electric Double Layer

The interaction between the electrode and electrolyte is complex in nature and took over 50 years for the interface to be described to a reasonable level. Stern modified the initial theories by Gouy, Chapman and Helmholtz in 1924.[63] Further modifications have been made over the years to improve the understanding of the various different scenarios that occur at the interface.[64] Due to the properties of charged electrodes and the formation of a region of charge at the surface, a layer of opposite charge in the electrolyte is expected to surround the electrode. Therefore there would essentially be two layers of opposite charges at the interface between the electrode and electrolyte, noted by Helmoltz as an *electric double layer* (Figure 2-11 (a)).[65] Helmholtz only took into account a rigid balance of charge in which the interactions between the electrode and electrolyte balance at the surface without extending further into the solution.[64] The electrostatic potential therefore drops rapidly to the value of the bulk solution, at a distance of x_H, forming a compact layer of charge.

This simplistic model didn't take into account the ability of the charges to move in an electrolyte solution or the effect of electrolyte concentration.[64] Gouy and Chapman, independently identified that both the potential and electrolyte solution would have an effect on the capacity of the double layer. Rather than being compact, the counteracting charges in the electrolyte would extend throughout the electrolyte forming a diffuse double layer (Figure 2-11 (b)). The effect of thermal motion and the coulombic interactions of the electrolyte with the electrode result in an increased concentration at the interface, before steadily declining towards the bulk potential at x_D.[66] The model also took into account that although the charge at the electrode is fixed at the surface, it may require a reasonable degree of electrolyte thickness to accommodate the full charge potential of the electrode.[65] In reality, the interface is a combination of both models.

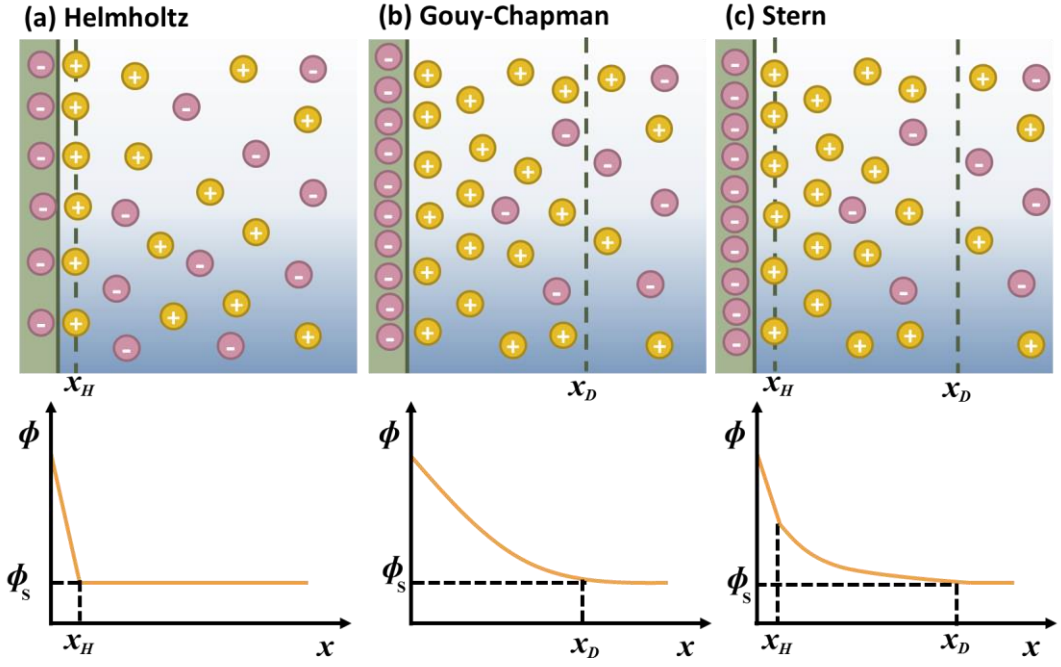

Figure 2-11 – Representation of different double layer models plus electrostatic potential (ϕ) diagrams versus distance from electrode (x) of each model (a) Helmholtz (b) Gouy-Chapman (c) Stern models

The Stern model (Figure 2-11 (c)) accounts for the size of the ions and allows for the formation of a compact layer at the surface of the electrode (x_H), at a distance determined by the ion size. A diffuse layer (x_D) then forms following the compact layer. Within the compact layer, there are two distinct

layers known as the inner and outer Helmholtz layers. The inner layer is comprised of specifically adsorbed species to the electrode. Due to the adsorption, the ions are at the closest possible approach.[65] Within the solution, particles will solvate increasing in radius due to the addition of water molecules. Due to their size, the solvated particles reside within the outer Helmholtz layer and are not specifically adsorbed. The size of the diffuse layer is dependent on the total ionic concentration of solution and therefore related to the electrolyte concentration.[55] The nature of the interface of the layer and the adsorbed species can affect the rate of reaction and therefore it is important to understand these base principles. However, unlike metal electrodes, semiconductors have significantly fewer accessible energy levels. This results in differences between the interface of a metal and electrolyte and that of a semiconductor and electrolyte.

2.3.3 Semiconductor-Electrolyte Interface

The interactions of a semiconductor and electrolyte are somewhat similar to those of a semiconductor-metal interface and the metal-electrolyte interfaces that have been discussed. However there are notable differences as a result of the specific properties of semiconductors. The conduction of semiconductors is typically lower than their metal counterparts as it is when compared to electrolyte solutions. Therefore, when a semiconductor and electrolyte are bought into contact there will be a potential drop in the system across the boundary to accommodate this disparity.[67] The variation in potential at the surface is known as the space charge region of the semiconductor and results in the conduction and valence bands bending, as with semiconductor-metal interfaces (Figure 2-5). Typically, doped semiconductors are utilised in electrochemical work and therefore the band bending is dependent on whether the semiconductor is *n*- or *p*-doped.

The change in the surface potential of the system is dependent on both the properties of the semiconductor and that of the electrolyte system. The redox potential of the electrolyte ultimately determines the extent to which the space charge regions changes. Figure 2-12 illustrates the different scenarios possible for an *n*-type semiconductor. The reverse is true for a *p*-

type semiconductor.[68] If the redox potential and Fermi level of the semiconductor are equivalent, no band bending occurs as there is no net transfer of charge. This stage, Figure 2-12 (a), is known as the flatband potential, E_{fb}. An accumulation region forms if the potential is below that of the flatband as a result of electron injection, forcing the bands to bend downwards (Figure 2-12 (b)).[64] In an accumulation layer, there is an excess of majority carriers at the interface giving rise to metallic like behaviour. The alternative situation is the formation of a depletion region (Figure 2-12 (c)).

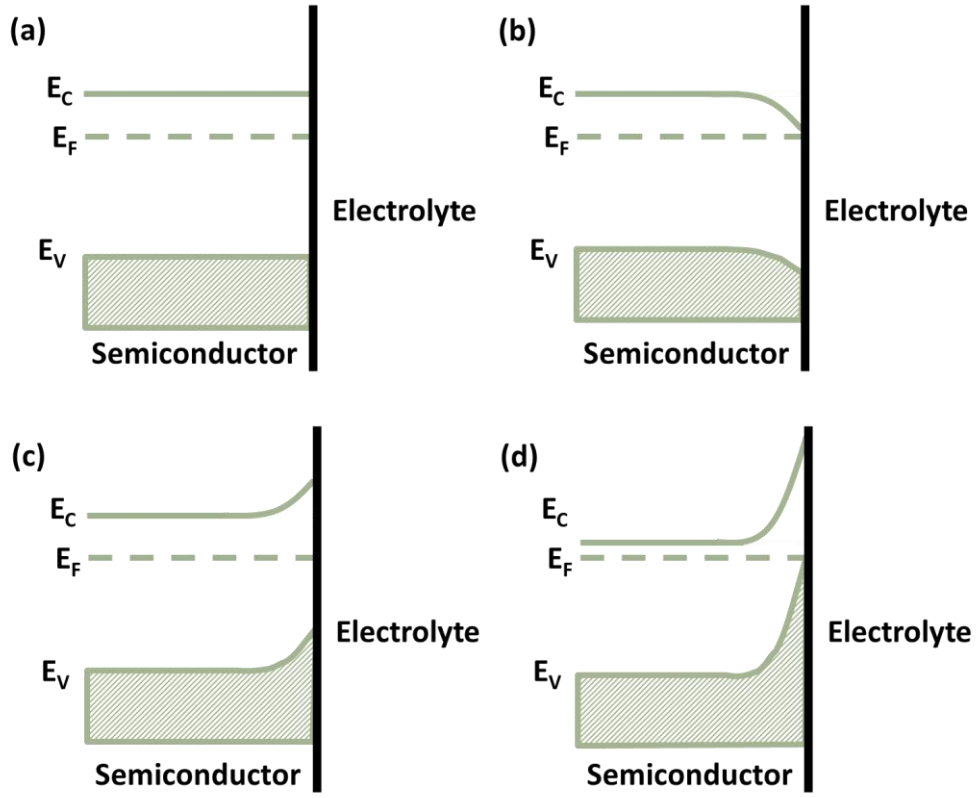

Figure 2-12 – Band structures of *n*-type semiconductors in electrolyte solution (a) equivalent Fermi level and redox potentials (b) semiconductor Fermi level < redox potential (c) semiconductor Fermi level > redox potential (d) semiconductor Fermi level >> redox potential

When the Fermi level of the semiconductor is greater than that of the electrolyte redox potential, there is a net flow of electrons into the electrolyte. This results in a depletion of electrons in the semiconductor surface and an upward shift in the bands of an *n*-type semiconductor. If a depletion region forms, electron-transfer processes are slow due to the lack of charge carriers. If a significant force is exerted on the system to extract

electrons from both the conduction and valence band of the electrode, an inversion layer will form (Figure 2-12 (d)). The excessive removal of electrons at the surface of the semiconductor causes an inversion of the semiconductor type in the space charge region. Therefore *n*-type semiconductors will become *p*-type at the interface.[64] In order for effective charge-transfer processes to occur, there has to be the presence of carriers. An accumulation of electrons in an *n*-type electrode accommodate reduction reactions while the accumulation of holes in *p*-type facilitates oxidation reactions.

Electron-Transfer Reactions

The reactions occurring at the surface of the semiconductor vary quite significantly from those on metals.[67] In order to fully understand the processes, knowledge of the relative positions of the semiconductor conduction and valence bands are required. Typically, semiconductor scientists regard band positions with reference to the vacuum energy level, while electrochemists, as stated, typically refer back to the standard hydrogen electrode (SHE).[69] The zero potential of the SHE is approximately -4.5 eV on the vacuum scale. In order for effective electron transfer reactions to occur there has to be sufficient overlap of the redox potentials and those of the semiconductor. However, the reactions are not limited solely to the conduction band and can occur due to overlap of the redox reaction with the valence band or semiconductor surface states.[69]

Figure 2-13 illustrates three potential scenarios in which electron-transfer reactions can occur in an *n*-type semiconductor. Overlap of the redox couple with the conduction band (Figure 2-13 (a)) would result in a relatively simple transfer of electrons from the redox couple into the conduction band resulting in a reduction of the electrolyte.[67] Alternatively, the redox couple could be positioned over the valence band (Figure 2-13 (b)), in which a transfer of holes into the redox couple result in the oxidation of species. The unique feature of semiconductors is the presence of adsorbates on the surface.[64] Adsorbates have distinct energy levels that differ from the bulk semiconductor and are known as surface states. Dependent upon the

energy position, the surface states can facilitate redox reactions between the semiconductor and electrolyte. Figure 2-13 (c) illustrates the presence of a surface state that conjugates with the conduction band.[69] Through the conjugation, despite the lack of conduction band overlap, there is still potential for a redox couple to interact via the intermediary of the surface state.

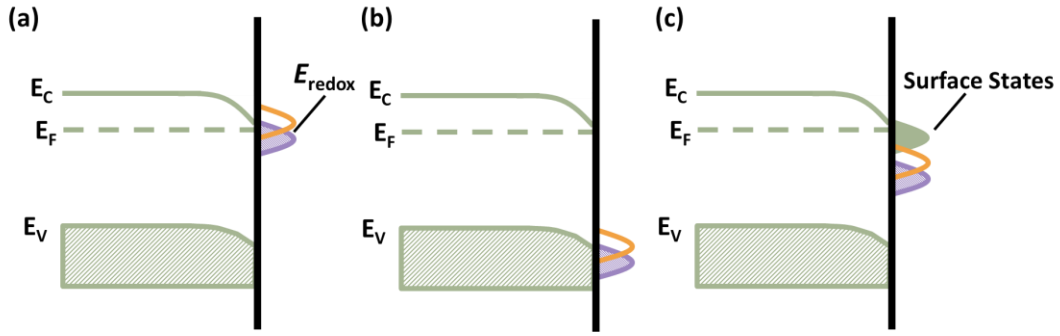

Figure 2-13 – Electron-transfer reactions for *n*-type semiconductor with redox electrolyte (a) overlap at conduction band (b) valence band overlap (c) conjugation of surface states & redox level

Surface states, band alignment and redox potentials are all essential pieces of required information in order to achieve desired reaction pathways. However, as a result of the properties of semiconductors, it is possible to enhance the electron transfer rate.[67] Photoexcitation of carriers in a semiconductor-electrolyte system can lead to reactions at the conduction and valence band sites. This process is known as photoelectrochemistry and is the basis of hydrogen production from sunlight.[70]

2.4 Photoelectrolysis

The introduction to semiconductor electrochemistry provides a basis for understanding the principals involved in the conversion of solar energy into hydrogen. However, it is necessary to discuss the process of photoelectrolysis before delving into the use of semiconductors to drive the process. Conversion of water (H_2O) into the constituent elements, H_2 and ½ O_2 results in a net energy change of 237.2 kJ mol^{-1}. From Equation 2-3, this equates to a $\Delta E^{\ominus}$ of 1.23 V. Therefore, in order to effectively split water a semiconductor is required to have a band gap of at 1.23 eV. In regards to the

available solar energy, 1.23 eV corresponds to wavelengths of <1000 nm, and therefore the majority of the visible spectrum has the available energy to split water.[71] This is the minimum theoretical value based on a perfect system. In reality there are losses associated with the electron-transfer process which results in typical energies of at least 1.6 eV being required to account for the over potentials occurring at the reaction sites.[72]

Although the amount of energy available is adequate, as discussed previously, in order for reactions to occur, there has to be suitable band overlaps of the redox potentials. Equation 2-5 (i) and (ii) represent the half reactions undergone when water is electrolysed as well as the potentials relative to the standard hydrogen electrode (SHE).[73] Since, the SHE is based on hydrogen, conversion of hydrogen ions has a reduction potential of 0 eV and requires the generation of two electrons. The oxidation half reaction requires 1.23 eV and the generation of 4 holes. The overall reaction for the production of one mole of oxygen and two moles of hydrogen requires the generation of four electron-hole pairs.

$$2H^+ + 2e^- \rightarrow H_2 \qquad E^{\emptyset}_{red} = 0\ eV \qquad \text{(i)}$$

$$2H_2O + 4h^+ \rightarrow O_2 + 4H^+ \qquad E^{\emptyset}_{ox} = 1.23\ eV \qquad \text{(ii)}$$

$$2H_2O \rightarrow O_2 + 2H_2 \qquad E^{\emptyset} = -1.23\ eV \qquad \text{(iii)}$$

Equation 2-5 – Redox potentials for photoelectrolysis of water (i) reduction of hydrogen (ii) oxidation of water (iii) overall reaction and potential vs. SHE

In order to drive the reaction, the semiconductor has to straddle the redox potentials. This system can either be completed with a single semiconductor material or via the use of multiple semiconductors to drive the individual reactions. Figure 2-14 illustrates the possible energy diagram for single step excitation and a two-step or z-scheme system.[74] In a type I system, a single semiconductor photocatalyst has the required band gap (>1.23 eV) and conduction and valence band positions to drive the reaction. When irradiated at energies above the band gap, an electron will be promoted from the valence band to the conduction band. The promoted

electron will drive the reduction of the H^+ ions while the generated hole will oxidise the water to O_2. For a single band gap device (E_g = 1.6 eV) the maximum theoretical efficiency under standard one sun illumination conditions is 30 %.[71] The type II system, also known as a Z-scheme, uses two semiconductors and a redox mediator. The reduction and oxidation of water occur at each separate semiconductor and the electrons are transferred via the use of a redox mediator. As each semiconductor is only required to have one overlapping band position, narrow gap semiconductors can be utilised in this system.[75]

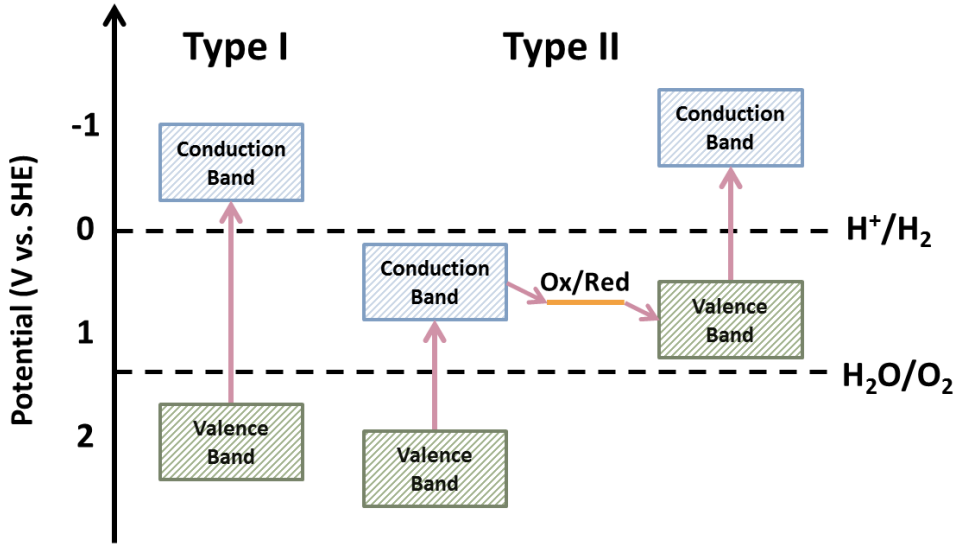

Figure 2-14 – Energy diagrams of water splitting based on (i) Type I system using a single semiconductor and excitation and (ii) Type II in which a two-step excitation of two semiconductors (Z-scheme)

The two systems described above are just potential variations on the process of water splitting. Typically semiconductors are either *n*- or *p*-type and therefore they will act as either a photoanode or photocathode respectively. In a type I system, the semiconductor acts as the working electrode however a counter electrode, typically platinum, is required to complete the circuit. If a photoanode is being employed, upon generation of the electron-hole pairs, the electrons will migrate out of the semiconductor to the counter electrode (Figure 2-15). The reduction of hydrogen will therefore happen at the counter electrode while the holes migrate to the surface of the semiconductor and oxidise the water. It is possible to have two

semiconductors acting in the system with both having the correct band positions for water splitting. The use of two electrodes can produce a higher voltage to overcome the over potentials as well as harnessing a greater portion of the solar spectrum effectively increasing the efficiency of the device.[76]

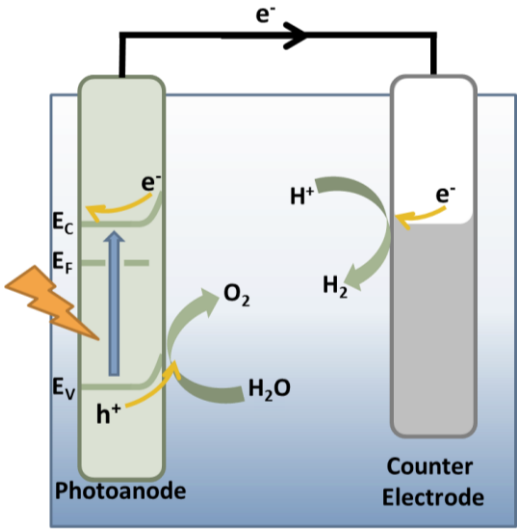

Figure 2-15 – Schematic of *n*-type photoanode under operation from irradiation source

Independent of system type, the processes occurring within the semiconductors is the same. Initially the semiconductor will absorb the incident radiation resulting in the promotion of an electron the conduction band (Figure 2-15). The generation of charges happens simultaneously, at this point, the charges can then migrate or recombine. The ideal situation is the separation of the electrons and holes, with migration to their respective reaction sites. However, as previously discussed (Figure 2-4), it is possible for the generated charges to recombine. Recombination can happen at the surface or in the bulk of the semiconductor.[77] In either situation, it is undesired, as it prevents the necessary charge-transfer reactions from occurring, limiting the overall efficiency of the device. Techniques can be employed to help reduce the recombination by encouraging the separation of the generated charges. This can include the addition of secondary particles to the semiconductor or alterations of device structure. Ultimately, the aim is to try and increase the efficiency of the device.

2.4.1 Efficiencies

In order to assess the performance of the device the generated photocurrent has to be compared to the amount of energy that has been input into the device. There are a number of different methods in which the efficiency can be represented however a recent review tried to standardise the methods in which it is reported.[78] Due to the nature of the water splitting reaction, the efficiency can be based on the generated photocurrent or the rate of the hydrogen production. The solar to hydrogen efficiency (STH) can be calculated based on the generated hydrogen versus the input energy (Equation 2-6).

$$STH = \frac{Output\ of\ H_2}{Energy\ of\ incident\ light} = \frac{r_{H_2} \times \Delta G}{P_{sun} \times S}$$

Equation 2-6 – Solar-to-hydrogen efficiency calculation

where r_{H_2} is the rate of hydrogen production and ΔG the gain in Gibbs energy of 237.2 kJ mol^{-1}. P_{sun} is the incident solar energy and S the area of the reactor.[74] Measurement of hydrogen during practical experiments is not always feasible and is dependent on the reactor.[79] If photocurrent is measured under the influence of an applied external bias this has to be accounted for in determining the efficiency (Equation 2-7). The efficiency is determined by the total current density of the system (j_p) multiplied by the difference between the required and applied voltage divided through by the incident power density (I_0).

$$\eta = j_p(1.23\ V - V_{ext})/I_0$$

Equation 2-7 – Photon to current efficiency equation of a photoelectrochemical cell under applied external bias

From the photocurrent it is possible to determine the theoretical hydrogen expected through the use of Faraday's law of electrolysis relating current ($\boldsymbol{i}$) to the production of reactant species ($\boldsymbol{N_{H_2}}$).[80]

$$\frac{dN_{H_2}}{dt} = \frac{i}{nF}$$

Equation 2-8 – Faraday's law of electrolysis relating current to molar production of hydrogen

When working with specific material types, the band gap of the semiconductor relates to a set wavelength. It is often useful to relate the efficiency of the device over a set range of wavelengths. This is known as the incident-photon conversion efficiency (IPCE)[81] and provides accurate wavelength dependent performance indicators. As the spectra of incident solar radiation is well known, understanding the operating performance at specific wavelengths provides an indication on device quality.

$$IPCE(\%) = 1240 \times \frac{J(mAcm^{-2})}{\lambda(nm) \times I(mWcm^{-2})} \times 100\%$$

Equation 2-9 – Incident-photon conversion efficiency calculation

2.4.2 Current Approaches

Since the seminal work on titanium dioxide of Honda and Fujishima in 1972,[82] there are and have been a wide array of semiconductors investigated for solar water splitting (Figure 2-16) with a number of reviews on the topic.[74,77,83,84] Oxide semiconductors are still the forefront in regards to research concentration however the variety of oxides studied has expanded significantly from the traditional titanium dioxide that led for many years.[85] The use of transition metal oxides, such as $NaTaO_3$, have shown reasonable levels of photocatalytic activity however the band gaps of these materials are typically large, resulting in the absorption of UV light only.[71] It is now common that co-catalysts are added to the semiconductor materials such as NiO or $Rh_{2-y}Cr_yO_3$ to improve the efficiency of hydrogen evolution.[74] These catalysts aid the efficiency of the devices though improved electron-hole separation, reducing recombination effects as well as improving the charge-transfer reactions to the water molecules.[84]

Independent on base semiconductor material, the desire is to push the absorption further into the visible portion of the solar spectrum. In order to achieve this, semiconductors are being sensitised via the addition of organic

dyes or additional narrow gap semiconductors. Various dyes have been investigated to push the absorption of oxide semiconductors into the visible range.[86] The dyes work by absorbing light in the visible region and transferring electrons into the conduction band of the semiconductor. In order for the charge-transfer to occur effectively, the molecular orbitals of the dye have to be sufficiently overlapping with the conduction band of the semiconductor.[86] This is also true when coupling with narrow gap semiconductors is concerned. The ideal situation occurs if the partnered semiconductor absorbs a complimentary portion of the solar spectrum (i.e. visible), has sufficient band overlaps with the wide gap semiconductor and fast electron transfer is possible.[84] As an example, CdS could be added to TiO_2 as a composite structure based on the band alignments (Figure 2-16).

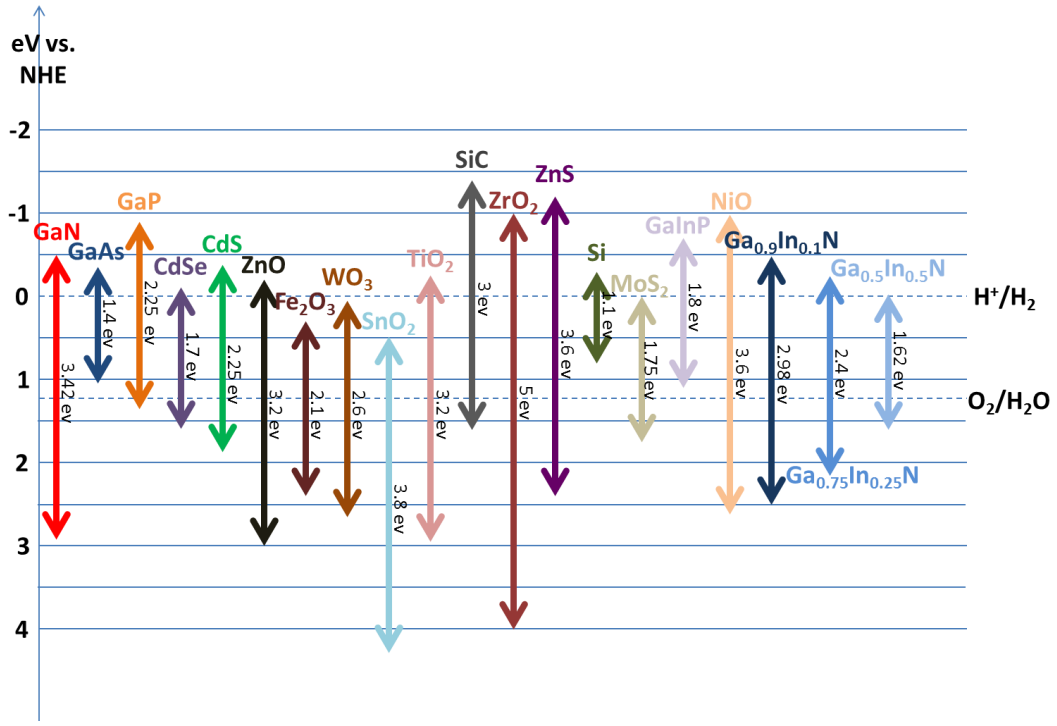

Figure 2-16 – Band positions of various semiconductors utilised for solar hydrogen production

Alongside material considerations, structural advances have also been a major area of development in recent years.[84] As the reaction between the semiconductor and electrolyte is dependent on charge-transfer, alterations to the device architecture can lead to efficiency improvements. The transport and recombination of the electrons and holes is dependent on the

crystal quality and structure of the semiconductor as well as the property of the semiconductor surface.[71] Different preparation techniques[74] have been implemented to create nanowires, nanotubes and nanorods.[57] The use of these one dimensional nanostructures has significant advantages over their planar counterparts because of the high surface area ratio of the devices. Alternative structures include porous and branched devices in which high levels of control are implemented to create the desired structures.[74]

The efficiency of these devices is steadily improving with current z-scheme systems achieving greater than 10 % efficiency.[87] However, the long term stability required for these devices has not yet been achieved. Currently, the devices cannot withstand the conditions exhibited in long term water splitting and undergo photocorrosion.

Photocorrosion

Ideally, the generated holes will migrate to the surface of the electrode (*n*-type) and oxidise the water on the surface. However, it is possible that the generated holes react with the semiconductor itself, oxidising and potentially corroding the device. This process is known as anodic photocorrosion. Cathodic photocorrosion is also possible for *p*-type electrodes in which the generated electrons cause the corrosion. The general decomposition reactions are illustrated in Equation 2-10.

$$M_xO_y + \frac{2y}{x}h^+ \overset{electrolyte}{\Longleftrightarrow} xM^{2y/x^+} + \frac{y}{2}O_2 \qquad \text{(i)}$$

$$M_xO_y + 2ye^- \overset{electrolyte}{\Longleftrightarrow} xM + yH_2O \qquad \text{(ii)}$$

Equation 2-10 – Typical photocorrosion reactions (i) anodic corrosion (ii) cathodic corrosion

This is a significant problem for many narrow gap semiconductors that have the required band positions for water splitting.[81] Photocorrosion can occur if the energy levels of anodic and cathodic decomposition are above the valence band minimum and below the conduction band minimum respectively.[88] The decomposition is influenced by both the pH of the solution and of the reactant product concentration. It is therefore possible

that the degree of corrosion can be controlled, either via an alteration of the reaction conditions or through the promotion of water splitting by using cocatalysts.[81]

2.4.4 III-Nitrides in Water Splitting

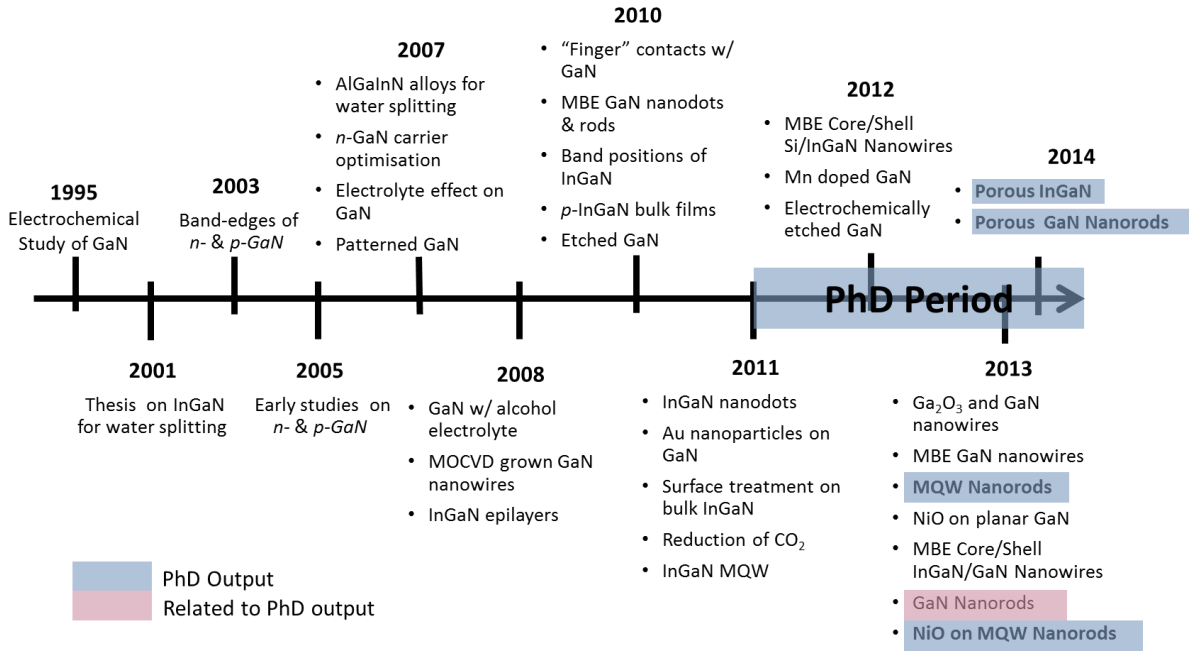

Figure 2-17 – Timeline of developments in III-nitrides for water splitting. Only first or significant reports mentioned and listed in publication order

As stated, it is possible to alloy any quantity of indium into gallium, harnessing significant portions of the solar spectrum (Figure 1-6). However, this is only beneficial if the band positions of GaN and the subsequent InGaN alloys are correctly aligned for water splitting. Theoretical and experimental work on the materials indicates that *p*- and *n*-type GaN[89] as well as InGaN alloys with indium contents up to 50 % have suitable band positions.[90] These properties, combined with the strong chemical resistance[21] of the nitrides make them suitable candidates for water splitting. Despite these properties, until recently there were relatively few reports on III-nitrides for water splitting, potentially due to the difficulties in understanding the band gap of InN as well as the growth of high quality materials. Figure 2-17 illustrates the progress in the field over the past two decades.

Early photoelectrochemical work was carried on GaN in 1995[91] and indicated that the band-edge potential of the material was suitably positioned

for water splitting. Despite this, further developments of the III-nitrides didn't arise until 2001. Beach examined the potential of InGaN materials for water splitting, characterising the flat band potentials and stability of the material in his thesis.[92] A decade after the initial investigation two groups began investigating planar *n*- and *p*-type GaN.[93–95] Typically *n*-type GaN has demonstrated significantly higher photocurrent than *p*-type, attributed to fast recombination processes of the magnesium (*p*-type) doped sample.[94] Since 2005 work on planar *n*- and *p*-type GaN continued in a range of mediums.[96–99] A reduction in photocurrent was observed for both types of electrode with prolonged use. For *n*-type GaN, photocorrosion has been observed[100] due to the oxidation of the GaN surface via the photogenerated holes, as in Equation 2-10, specifically for GaN,

$$2GaN\ (s) + \ 6h^{+} = 2Ga^{3+} + N_2(g)$$

Equation 2-11 – Oxidation of *n*-type GaN with photogenerated holes

The oxidation ultimately results in the dissolution and alteration of the surface resulting in a reduction of the generated photocurrent. A pH range of 2.5-11.7 offers the most stable region for Ga^{3+} and therefore the most appropriate region for preventing corrosion in the system.[101] In a *p*-GaN system, there is the potential to withstand a greater degree of corrosion in comparison to *n*-GaN due to the accumulation of electrons at the surface, forming a barrier preventing photocorrosion and anodic oxidation.[94] However the degradation experienced in *p*-type is thought to arise from the passivation of the magnesium carriers, reducing the total number of charge carriers available and increasing resistance.[102] Optimisation of the carrier concentration in *n*-type GaN resulted in a value in the region of 10^{17} cm^{-3} indicating that only minimum doping levels are required for the highest photocurrents.[103] However, control over the depletion region and resistivity of *n*-GaN has been achieved through an *n-n+* structure in which the top layer has a different doping level to the bulk *n+* layer, resulting in an improved photocurrent.[97]

Surface modifications have also resulted in changes to the performance of the GaN devices. This has been achieved via a number of methods,[104–109] which either help to remove recombination centres, increases the active surface area or a combination of both. Further discussion on this area will be presented in Chapters 4 and 6. Additions to the GaN surface have also proved effective. Nobel metals including ruthenium and platinum have been shown to be beneficial co-catalysts in the production of hydrogen. Typically core-shell nanoparticles have been utilised to promote the forward reaction while limiting the reverse reaction via the creation of a preventative barrier between the oxygen and the noble catalyst.[110–112] Due to the unreactive nature of gold, particles were found to increase the photocurrent in *p*-type GaN due to a positive effect in band bending.[113] While the addition of NiO has shown improved photocurrents and device stability due to the overlapping band structure promoting reactions at the NiO surface.[114–116] This topic will be explored further in Chapter 5.

For InGaN photoelectodes, a greater deal of success has been achieved with *p*-type material compared to *p*-GaN with a direct relationship between hole mobility and photocurrent observed.[117] The majority of work has been conducted with bulk InGaN films[118–120] with some on MQW devices[108,115,121] Unfortunately for the bulk devices, the quality of the indium films has degenerated with increased composition which has resulted in varied results.[117] The improvements achieved over bulk GaN material has been attributed to the increased absorption of solar radiation. There has been some recent work conducted on MBE grown nanowires which have shown reasonable performance in visible light.[122,123] The use of core/shell structures has allowed the formation of multi-band gap materials which potentially have the ability to harness narrow gap semiconductors while protecting them from degradation with a nitride shell.

The work to date on III-nitride materials has shown a reasonable degree of progress with device and material considerations being investigated. The following chapters will explore the contribution I have made over the course of my PhD.

Bibliography

[1] K. Seeger, *Semiconductor Physics: An Introduction*, 9th ed. (Springer-Verlag, Berlin, 2004), pp. 1–9.

[2] G. Parker, *Introductory Semiconductor Device Physics* (Prentice Hall Europe, Trowbridge, 1994), pp. 1–7.

[3] G. Parker, *Introductory Semiconductor Device Physics* (Prentice Hall Europe, Trowbridge, 1994), pp. 8–25.

[4] G. Parker, *Introductory Semiconductor Device Physics* (Prentice Hall Europe, Trowbridge, 1994), pp. 45–69.

[5] D.K. Roy, *Physics Of Semiconductor Devices (Rev.)*, 2nd ed. (Orient BlackSwan, Hyderabad, 2004), pp. 1–45.

[6] K. Seeger, *Semiconductor Physics: An Introduction*, 9th ed. (Springer-Verlag, Berlin, 2004), pp. 118–158.

[7] Baldassare Di Bartolo and J. Collins, in *Handb. Lumin. Semicond. Mater.*, edited by L. Bergman and J.L. McHale (Taylor & Francis, Boca Raton, 2011), pp. 1–20.

[8] I. Pelant and J. Valenta, *Luminescence Spectroscopy of Semiconductors*, Illustrate (Oxford University Press, Oxford, 2012), pp. 148–160.

[9] A.M. Stoneham, *Reports Prog. Phys.* **44**, 1251 (1981).

[10] P. YU and M. Cardona, *Fundamentals of Semiconductors: Physics and Materials Properties*, 4th ed. (Springer, London, 2010), pp. 244–333.

[11] D.K. Roy, *Physics of Semiconductor Devices (Rev.)*, 2nd ed. (Orient BlackSwan, Hyderabad, 2004), pp. 306–354.

[12] E.H. Rhoderick and R.H. Williams, *Metal-Semiconductor Contacts*, 2nd ed. (Clarendon Press, Oxford, 1988), pp. 1–35.

[13] H. Morkoç, *Handbook of Nitride Semiconductors and Devices, Materials Properties, Physics and Growth* (Wiley-VCH Verlag GmbH & Co. KGaA, Weinheim, 2009), pp. 1–110.

[14] H. Amano, N. Sawaki, I. Akasaki, and Y. Toyoda, *Appl. Phys. Lett.* **48**, 353 (1986).

[15] H. Amano, I. Akasaki, T. Kozawa, K. Hiramatsu, N. Sawaki, K. Ikeda, and Y. Ishii, *J. Lumin.* **40-41**, 121 (1988).

[16] S. Nakamura and T. Mukai, *Jpn. J. Appl. Phys.* **31**, L1457 (1992).

[17] H. Amano, *Jpn. J. Appl. Phys.* **52**, 050001 (2013).

[18] S. Nakamura and M.R. Krames, *Proc. IEEE* **101**, 2211 (2013).

[19] T. Hanada, in *Oxide Nitride Semicond. Process. Prop. Appl.*, edited by T. Yao and S.-K. Hong (Springer Berlin Heidelberg, Berlin, 2009), pp. 1–19.

[20] S. Adachi, *Properties of Group-IV, III-V and II-VI Semiconductors* (John Wiley & Sons, Chichester, 2005), pp. 1–22.

[21] S. Strite and H. Morkoc̆, *J. Vac. Sci. Technol. B Microelectron. Nanom. Struct.* **10**, 1237 (1992).

[22] D.K. Kim and C.B. Park, **47**, 1006 (2005).

[23] H. Morkoç, *Handbook of Nitride Semiconductors and Devices, Materials Properties, Physics and Growth* (Wiley-VCH Verlag GmbH & Co. KGaA, Weinheim, 2009), pp. 131–321.

[24] H. Morkoç, *Handbook of Nitride Semiconductors and Devices, Materials Properties, Physics and Growth* (Wiley-VCH Verlag GmbH & Co. KGaA, Weinheim, 2009), pp. 323–400.

[25] J.L. Zilko, in *Handb. Thin Film Depos. Process. Technol.*, edited by K. Seshan, 2nd ed. (Noyes Publications, Norwich, NY, 2002), pp. 151–203.

[26] O. Ambacher, *J. Phys. D. Appl. Phys.* **31**, 2653 (1998).

[27] J. Bai, T. Wang, P. Comming, P.J. Parbrook, J.P.R. David, and a. G. Cullis, *J. Appl. Phys.* **99**, 023513 (2006).

[28] J. Wang, M. Nozaki, Y. Ishikawa, M.S. Hao, Y. Morishima, T. Wang, Y. Naoi, and S. Sakai, **197**, 48 (1999).

[29] H. Wang, C. Chen, Z. Gong, J. Zhang, M. Gaevski, M. Su, J. Yang, and M.A. Khan, *Appl. Phys. Lett.* **84**, 499 (2004).

[30] H. Amano, and S.P. Izabella Grzegory, Michal Bockowski, Piotr Perlin, Czeslaw Skierbiszewski, Tadeusz Suski, Marcin Sarzynski, Stanislaw Krukowski, A.D. and A. Krost, R.K. and Z. Sitar, A. Strittmatter, and N.G. Raphaël Butté, Gatien Cosendey, Lorenzo Lugani, Marlene Glauser, Antonino Castiglia, Guillaume Perillat-Merceroz, Jean-François Carlin, H. Miyake, M.K. and T. Wernicke, R.S. and E. Monroy, J.Y. Duboz, and T.P. Yvon Cordier, Tatsuya Fujishima, Bin Lu, Elison Matioli, M.T. and F. Julien, and B.G. Tatiana V. Shubina, Mikhail M. Glazov, Nikolay A. Gippius, C. Gergely, W.R.L.L. and A. Punya, and O.K. and I.A. Shelykh, *III-Nitride Semiconductors and Their Modern Devices*, 1st ed. (Oxford University Press, New York, 2013).

[31] I. Akasaki, *Mater. Sci. Eng. B* **74**, 101 (2000).

[32] J.I. Pankove, *Mater. Sci. Eng. B* **61-62**, 305 (1999).

[33] H. Amano, M. Kito, K. Hiramatsu, and I. Akasaki, *Jpn. J. Appl. Phys.* **28**, L2112 (1989).

[34] S. Nakamura, T. Mukai, M. Senoh, and N. Iwasa, *Jpn. J. Appl. Phys.* **31**, L139 (1992).

[35] M. Asif Khan, M. Shatalov, H.P. Maruska, H.M. Wang, and E. Kuokstis, *Jpn. J. Appl. Phys.* **44**, 7191 (2005).

[36] D. Mui, Z. Wang, and H. Morkoç, *Thin Solid Films* **231**, 107 (1993).

[37] R.M. Farrell, C.J. Neufeld, S.C. Cruz, J.R. Lang, M. Iza, S. Keller, S. Nakamura, S.P. DenBaars, U.K. Mishra, and J.S. Speck, *Appl. Phys. Lett.* **98**, 201107 (2011).

[38] D.-M. Yeh, C.-F. Huang, C.-Y. Chen, Y.-C. Lu, and C.C. Yang, *Appl. Phys. Lett.* **91**, 171103 (2007).

[39] C. Lee, S. Kim, and K. Lim, **35**, 280 (1999).

[40] R. Horng, S. Lin, Y. Tsai, M. Chu, W. Liao, M. Wu, R. Lin, and Y. Lu, *IEEE Electron Device Lett.* **30**, 724 (2009).

[41] B.R. Nag, *Physics of Quantum Well Devices* (Kluwer Academic Publishers, Dordrecht, 2001), pp. 1–6.

[42] Z.L. Li, P.T. Lai, S. Member, and H.W. Choi, *IEEE Photonics Technol. Lett.* **21**, 1429 (2009).

[43] F.K. Yam and Z. Hassan, *Superlattices Microstruct.* **43**, 1 (2008).

[44] S.P. DenBaars, D. Feezell, K. Kelchner, S. Pimputkar, C.-C. Pan, C.-C. Yen, S. Tanaka, Y. Zhao, N. Pfaff, R. Farrell, M. Iza, S. Keller, U. Mishra, J.S. Speck, and S. Nakamura, *Acta Mater.* **61**, 945 (2013).

[45] J.I. Pankove, *Appl. Phys. Lett.* **25**, 53 (1974).

[46] S. Ruvimov, Z. Liliental-Weber, J. Washburn, K.J. Duxstad, E.E. Haller, Z.-F. Fan, S.N. Mohammad, W. Kim, a. E. Botchkarev, and H. Morkoc, *Appl. Phys. Lett.* **69**, 1556 (1996).

[47] B.P. Luther, S.E. Mohney, T.N. Jackson, M. Asif Khan, Q. Chen, and J.W. Yang, *Appl. Phys. Lett.* **70**, 57 (1997).

[48] D.-F. Wang, F. Shiwei, C. Lu, A. Motayed, M. Jah, S.N. Mohammad, K. a. Jones, and L. Salamanca-Riba, *J. Appl. Phys.* **89**, 6214 (2001).

[49] Z.X. Qin, Z.Z. Chen, Y.Z. Tong, X.M. Ding, X.D. Hu, T.J. Yu, and G.Y. Zhang, *Appl. Phys. A Mater. Sci. Process.* **78**, 729 (2004).

[50] C.-L. Tsai, Y.-K. Fu, H.-T. Chen, C.-H. Chou, and R. Xuan, *Phys. Stat. Sol (C)* **11**, 957 (2014).

[51] Y.-I. Nam and B.-T. Lee, *Semicond. Sci. Technol.* **26**, 085014 (2011).

[52] J.-K. Ho, C.-S. Jong, C.C. Chiu, C.-N. Huang, C.-Y. Chen, and K.-K. Shih, *Appl. Phys. Lett.* **74**, 1275 (1999).

[53] J.-K. Ho, C.-S. Jong, C.C. Chiu, C.-N. Huang, K.-K. Shih, L.-C. Chen, F.-R. Chen, and J.-J. Kai, *J. Appl. Phys.* **86**, 4491 (1999).

[54] C.M.A. Brett and A.M.O. Brett, *Electrochemistry Principles, Methods and Applications* (Oxford University Press, Oxford, 1993), pp. vii–viii.

[55] A.J. Bard and L.R. Faulkner, *Electrochemical Methods: Fundamentals and Applications*, 2nd ed. (John Wiley & Sons, New York, 2001), pp. 1–39.

[56] C.M.A. Brett and A.M.O. Brett, *Electrochemistry Principles, Methods and Applications* (Oxford University Press, Oxford, 1993), pp. 1–7.

[57] Y. Lin, G. Yuan, R. Liu, S. Zhou, S.W. Sheehan, and D. Wang, *Chem. Phys. Lett.* **507**, 209 (2011).

[58] D. Pletcher, R. Greff, R. Peat, L.M. Peter, and J. Robinson, *Instrumental Methods in Electrochemistry*, Reprint (Woodhead Publishing Ltd., Cambridge, 2011), pp. 15–41.

[59] C.M.A. Brett and A.M.O. Brett, *Electrochemistry Principles, Methods and Applications* (Oxford University Press, Oxford, 1993), pp. 13–38.

[60] A. Bard and L. Faulkner, *Electrochemical Methods: Fundamentals and Applications*, 2nd ed. (John Wiley & Sons, New York, 2001), pp. 44–82.

[61] P.H. Rieger, *Electrochemistry*, 2nd ed. (Chapman & Hall Inc., New York, 1994), pp. 1–54.

[62] A. Bard and L. Faulkner, *Electrochemical Methods: Fundamentals and Applications*, 2nd ed. (John Wiley & Sons, New York, 2001), pp. 137–154.

[63] P.H. Rieger, *Electrochemistry*, 2nd ed. (Chapman & Hall Inc., New York, 1994), pp. 59–68.

[64] C.M.A. Brett and A.M.O. Brett, *Electrochemistry Principles, Methods and Applications* (Oxford University Press, Oxford, 1993), pp. 39–69.

[65] A.J. Bard and L.R. Faulkner, *Electrochemical Methods: Fundamentals and Applications*, 2nd ed. (John Wiley & Sons, New York, 2001), pp. 534–579.

[66] D. Pletcher, R. Greff, R. Peat, L.M. Peter, and J. Robinson, *Instrumental Methods in Electrochemistry*, Reprint (Cambridge University Press, Cambridge, 2011), pp. 149–176.

[67] W. Schmickler and E. Santos, *Interfacial Electrochemistry*, 2nd ed. (Springer Berlin Heidelberg, Berlin, 2010), pp. 117–131.

[68] A.W. Bott, *Curr. Sep.* **17**, 87 (1998).

[69] K. Rajeshwar, in *Encycl. Electrochem. Vol. 6*, edited by A.J. Bard, M. Stratmann, and S. Licht (Wiley-VCH Verlag GmbH & Co. KGaA, 2007), pp. 1–51.

[70] C.M.A. Brett and A.M.O. Brett, *Electrochemistry Principles, Methods and Applications* (Oxford University Press, Oxford, 1993), pp. 278–283.

[71] M.G. Walter, E.L. Warren, J.R. McKone, S.W. Boettcher, Q. Mi, E. a Santori, and N.S. Lewis, *Chem. Rev.* **110**, 6446 (2010).

[72] J. a. Turner, *Science* **285**, 687 (1999).

[73] A. Currao, *Chim. Int. J. Chem.* **61**, 815 (2007).

[74] T. Hisatomi, J. Kubota, and K. Domen, *Chem. Soc. Rev.* (2014).

[75] S.W. Bae, S.M. Ji, S.J. Hong, J.W. Jang, and J.S. Lee, *Int. J. Hydrogen Energy* **34**, 3243 (2009).

[76] H. Zhang, S. Huang, and G. Conibeer, *Energy Procedia* **22**, 10 (2012).

[77] A. Mills and S. Le Hunte, *J. Photochem. Photobiol. A Chem.* **108**, 1 (2000).

[78] Z. Chen, T.F. Jaramillo, T.G. Deutsch, A. Kleiman-Shwarsctein, A.J. Forman, N. Gaillard, R. Garland, K. Takanabe, C. Heske, M. Sunkara, E.W. McFarland, K. Domen, E.L. Miller, J. a. Turner, and H.N. Dinh, *J. Mater. Res.* **25**, 3 (2011).

[79] L.J. Minggu, W.R. Wan Daud, and M.B. Kassim, *Int. J. Hydrogen Energy* **35**, 5233 (2010).

[80] A.J. Bard and L.R. Faulkner, *Electrochemical Methods: Fundamentals and Applications*, 2nd ed. (John Wiley & Sons, New York, 2001), pp. 418–427.

[81] R. van de Krol and M. Grätzel, *Photoelectrochemical Hydrogen Production* (Springer US, Boston, MA, 2012), pp. 13–67.

[82] A. Fujishima and K. Honda, *Nature* **238**, 37 (1972).

[83] P.N. Ciesielski, F.M. Hijazi, A.M. Scott, C.J. Faulkner, L. Beard, K. Emmett, S.J. Rosenthal, D. Cliffel, and G. Kane Jennings, *Bioresour. Technol.* **101**, 3047 (2010).

[84] R.M. Navarro Yerga, M.C. Alvarez Galván, F. del Valle, J. a Villoria de la Mano, and J.L.G. Fierro, *ChemSusChem* **2**, 471 (2009).

[85] M. Woodhouse and B. a Parkinson, *Chem. Soc. Rev.* **38**, 197 (2009).

[86] M. Ni, M.K.H. Leung, D.Y.C. Leung, and K. Sumathy, *Renew. Sustain. Energy Rev.* **11**, 401 (2007).

[87] F.E. Osterloh, *Chem. Soc. Rev.* **42**, 2294 (2013).

[88] S.R. Morrison, *Electrochemistry of Semiconductor and Oxidized Metal Electrodes*, Illustrate (Plenum Press, New York, 1980).

[89] J.D. Beach, R.T. Collins, and J. a. Turner, *J. Electrochem. Soc.* **150**, A899 (2003).

[90] P.G. Moses and C.G. Van de Walle, *Appl. Phys. Lett.* **96**, 021908 (2010).

[91] S.S. Kocha, *J. Electrochem. Soc.* **142**, L238 (1995).

[92] J.D. Beach, InxGa1-xN For Potoelectrochemical Water Splitting, Colorado School of Mines, 2001.

[93] N. Kobayashi, T. Narumi, and R. Morita, *Jpn. J. Appl. Phys.* **44**, L784 (2005).

[94] K. Fujii and K. Ohkawa, *Jpn. J. Appl. Phys.* **44**, L909 LP (2005).

[95] K. Fujii, T. Karasawa, and K. Ohkawa, *Jpn. J. Appl. Phys.* **44**, L543 (2005).

[96] K. Fujii and K. Ohkawa, *J. Electrochem. Soc.* **153**, A468 (2006).

[97] Y. Iwaki, M. Ono, K. Yamaguchi, K. Kusakabe, K. Fujii, and K. Ohkawa, *Phys. Stat. Sol (C)* **5**, 2349 (2008).

[98] S.-Y. Liu, J.K. Sheu, M.L. Lee, Y.-C. Lin, S.J. Tu, F.W. Huang, and W.C. Lai, *Opt. Express* **20 Suppl 2**, A190 (2012).

[99] K. Fujii, H. Nakayama, K. Sato, T. Kato, M.-W. Cho, and T. Yao, *Phys. Stat. Sol (C)* **5**, 2333 (2008).

[100] K. Fujii, T. Ito, M. Ono, Y. Iwaki, T. Yao, and K. Ohkawa, *Phys. Stat. Sol (C)* **4**, 2650 (2007).

[101] M. Pourbaix, *Atlas of Electrochemical Equilibria in Aqueous Solutions* (National Association of Corrosion Engineers, 1974).

[102] D. Takagi, T. Narumi, N. Kobayashi, J. Yamamoto, Y. Ban, and K. Wakao, *Jpn. J. Appl. Phys.* **46**, 572 (2007).

[103] M. Ono, K. Fujii, T. Ito, Y. Iwaki, A. Hirako, T. Yao, and K. Ohkawa, *J. Chem. Phys.* **126**, 054708 (2007).

[104] I. Waki, D. Cohen, R. Lal, U. Mishra, S.P. DenBaars, and S. Nakamura, *Appl. Phys. Lett.* **91**, 093519 (2007).

[105] H. Jung, Y. Hong, Y. Li, J. Cho, Y. Kim, and G. Yi, *ACS Nano* **2**, 637 (2008).

[106] J.-S. Hwang, T.-Y. Liu, S. Chattopadhyay, G.-M. Hsu, A.M. Basilio, H.-W. Chen, Y.-K. Hsu, W.-H. Tu, Y.-G. Lin, K.-H. Chen, C.-C. Li, S.-B. Wang, H.-Y. Chen, and L.-C. Chen, *Nanotechnology* **24**, 055401 (2013).

[107] K. Fujii, T. Kato, K. Sato, I. Im, J. Chang, and T. Yao, *Phys. Stat. Sol (C)* **7**, 2218 (2010).

[108] J. Benton, J. Bai, and T. Wang, *Appl. Phys. Lett.* **102**, 173905 (2013).

[109] B. AlOtaibi, M. Harati, S. Fan, S. Zhao, H.P.T. Nguyen, M.G. Kibria, and Z. Mi, *Nanotechnology* **24**, 175401 (2013).

[110] B.S. Kwak, J. Kim, and M. Kang, *Int. J. Hydrogen Energy* **35**, 11829 (2010).

[111] N.V. Long, M. Ohtaki, T.D. Hien, J. Randy, and M. Nogami, *Electrochim. Acta* **56**, 9133 (2011).

[112] X. Wang, G. Liu, G.Q. Lu, and H.-M. Cheng, *Int. J. Hydrogen Energy* **35**, 8199 (2010).

[113] W.-H. Tu, Y.-K. Hsu, C.-H. Yen, C.-I. Wu, J.-S. Hwang, L.-C. Chen, and K.-H. Chen, *Electrochem. Commun.* **13**, 530 (2011).

[114] K. Ohkawa, W. Ohara, D. Uchida, and M. Deura, *Jpn. J. Appl. Phys.* **52**, 08JH04 (2013).

[115] J. Benton, J. Bai, and T. Wang, *Appl. Phys. Lett.* **103**, 133904 (2013).

[116] S.H. Kim, M. Ebaid, J.-H. Kang, and S.-W. Ryu, *Appl. Surf. Sci.* **305**, 638 (2014).

[117] K. Aryal, B.N. Pantha, J. Li, J.Y. Lin, and H.X. Jiang, *Appl. Phys. Lett.* **96**, 052110 (2010).

[118] J. Li, J.Y. Lin, and H.X. Jiang, *Appl. Phys. Lett.* **93**, 162107 (2008).

[119] M. Li, W. Luo, B. Liu, X. Zhao, Z. Li, D. Chen, T. Yu, Z. Xie, R. Zhang, and Z. Zou, *Appl. Phys. Lett.* **99**, 112108 (2011).

[120] W. Luo, B. Liu, Z. Li, Z. Xie, D. Chen, Z. Zou, and R. Zhang, *Appl. Phys. Lett.* **92**, 262110 (2008).

[121] K. Fujii, S. Nakamura, S. Yokojima, T. Goto, T. Yao, M. Sugiyama, and Y. Nakano, *J. Phys. Chem. C* **115**, 25165 (2011).

[122] Y.J. Hwang, C.H. Wu, C. Hahn, H.E. Jeong, and P. Yang, *Nano Lett.* **12**, 1678 (2012).

[123] B. AlOtaibi, H.P.T. Nguyen, S. Zhao, M.G. Kibria, S. Fan, and Z. Mi, *Nano Lett.* **13**, 4356 (2013).

Chapter 3

Experimental Techniques

Various techniques are required to achieve the targets for the project, including device fabrication, structural characterisation and performance assessment. The principles behind each technique are introduced in detail in order to provide a coherent overview of all methods utilised.

3.1 Growth

All wafers were grown in a single chamber 3x2" showerhead metal organic chemical vapour deposition (MOCVD) reactor. A schematic of the reaction process is illustrated in Figure 3-1. As discussed in Chapter 2, trimethyl-metals (Al, Ga or In) and ammonia are used as reagents with nitrogen gas the carrier gas. A growth substrate (2" sapphire wafer) is placed onto a susceptor, which then enters into the reaction chamber. The flow rates of the reagents are controlled depending on reaction requirements and the susceptor heats the substrate to the specified growth temperatures. As the reagents (trimethy gallium and ammonia) enter the chamber, the decomposition process initiates at the surface of the substrate, due to the elevated temperature, and epitaxial layers begin to form. As a result of the reaction, chemical by-products in the form of methane (CH_4) are formed and removed from the chamber by the carrier gases. The deposition process

continues until the desired epitaxial later thicknesses are achieved and the reaction terminated.

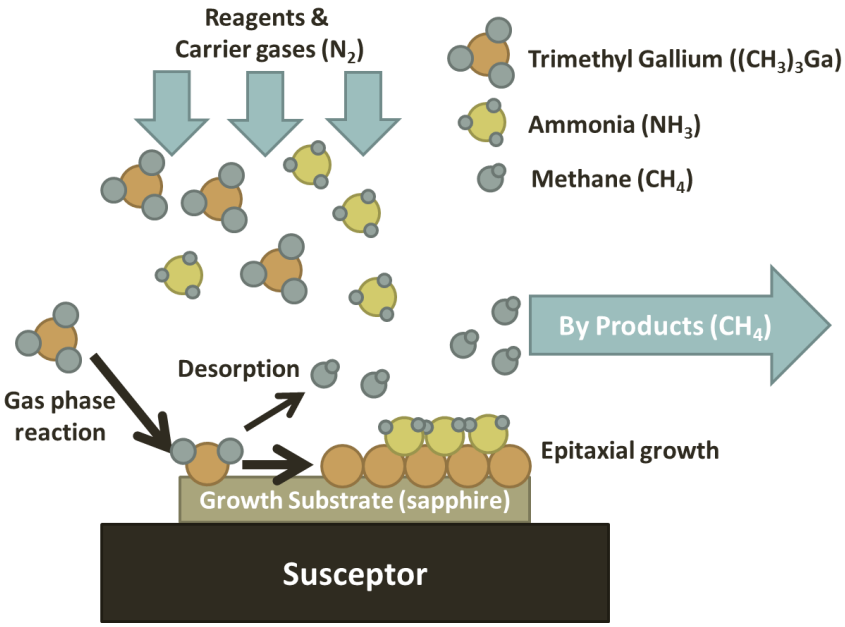

Figure 3-1 – Schematic illustration of reaction process in a metal organic chemical vapour deposition (MOCVD) reactor for the growth of GaN

3.2 Fabrication

A number of methods for semiconductor device fabrication have been developed in order to fabricate novel nanostructures with an enhanced performance within this thesis. The majority of device fabrication has been performed in the high class cleanroom at Sheffield University, where the EPSRC III-V National centre is partially involved. All the material characterization and device testing has been carried out within our III-nitride research group. All the epi-wafers utilised are also grown within our III-nitride research group.

3.2.1 Dry Etch Techniques

Etching technologies are typical approaches for the fabrication of semiconductor devices. There are two major approaches, dry etching and chemical wet etching.[1] The former provides a quick and isotropic etching process however it will generally generate damage which can be avoided in chemical etching. Depending on the materials utilised, the wet etching rate and final surface effect can vary significantly. Alongside this, wet etching also

depends on crystallographic orientation of the material. In practical applications within the semiconductor industry, dry etching is the dominant approach. Both dry and wet etch methods, including photoelectrochemical wet etching are utilised to achieve the desired nanostructures.

Reactive-Ion Etching

Reactive-ion etching (RIE) utilises chemically reactive plasma to etch semiconductors, where the plasma is generated under low pressure (vacuum) through a radio frequency (RF) generator. It can provide a greater degree of control over etch conditions and profiles. An RIE consists of a process chamber in which two parallel electrodes are positioned at the top and base of the chamber. The side walls and upper electrode are electrically grounded, isolating the lower electrode where the sample is located. The chamber allows for a controlled flow of etchant gases into the chamber during the etch process.

As mentioned above, it is necessary to pump down the pressure of the chamber prior to etching. Etchant gases are then injected into the chamber and the pressure stabilised. Typical etchant gases include Ar, CHF_3, O_2, SF_6 and the flow rates controlled depending on the required etch,[2] usually at low pressures of a few millitorr. CHF_3, O_2 and SF_6 are the main gases used in this work for the etching of SiO_2.[3–5] Once stabilised, a radio frequency (RF) generator with a typical frequency of 13.56 megahertz is switched on, with a power around 100 W, to the lower electrode creating an electric field between the parallel electrodes. The RF electric field ionises the gas molecules, losing electrons from their outer orbitals becoming positive ions. This forms a high density plasma within the chamber. As a result of the electric isolation of the lower electrode, bombardment of electrons to the sample platter causes an electron charge to build-up. The disproportionate charge between the upper and lower electrodes causes the positive etchant gas ions to migrate towards the sample. These ions interact with the sample surface where they either react or remove some of the sample material. Hence it is the reactive-ions within the chamber that result in the etching of the material.

Inductively Coupled Plasma RIE

Inductively coupled plasma etching (ICP) is another advanced dry etching technique which includes the RIE function. ICP has an additional plasma generator in the form of an inductively coupled generator. The resultant enhanced plasma density allows for a greater degree of control over the etch conditions and results in faster etch rates. In normal RIE systems, etch rates are limited as increasing the RF power will cause the bias voltage across the cathode to increase, reducing the selectivity of the etch. ICP allows for greater selectivity due to the separation of the RF generator and etch chamber, with the RF coupled into the chamber with an inductive couple. A second RF generator is connected to the sample stage increasing the plasma density. The combination of the two generators gives a greater degree of control over the self-biasing of the sample platter. ICP has been widely used for the etching of III-nitride materials, typically with a Cl_2/Ar gas mixture.[6,7] The etchant gas flow and RF power can be controlled depending of the required etch. An Oxford Instruments Plasma Technology ICP 380 is utilised within this thesis.

3.2.2 Photolithography

Photolithography is a standard technique in semiconductor device processing, allowing the transfer of a pattern from prepared masks to the material for further device fabrication process. A light sensitive material, known as a photoresist is utilised as the medium to transfer the pattern to the sample. As a result of the light sensitivity, device processing is performed in a yellow room in which filters have been implemented to prevent the premature change in the photoresists chemical makeup. The typical conditions utilised to obtain the best uniformity are described. Prior to deposition of the photoresist, the sample is dehydrated at 100 °C to remove any adsorbed moisture from the surface and prevent proper adhesion of the photoresist. The sample is then spun at 4000 rpm for 30 seconds to remove any further dust particles. A few drops of resist are then placed upon the sample and left to spread before spinning again at 4000 rpm to create a thin

even film. It is finally soft-baked at 100 °C for a minute to remove excess resist solvent to prevent the sample sticking to the photomask.

A photomask is a quartz plate in which a designed pattern is deposited onto one side, commonly in chrome. The photomask is inserted into a mask aligner with the metal side down and secured in position. The photoresist covered sample is positioned under the photomask, aligned and moved into contact with the metal side. An exposure time is set and the sample exposed to UV light through the photomask, transferring the pattern onto the sample by altering the bonds within the photoresist in the exposed areas. The exposed sample is then developed in the resists counterpart developer, finalising the transfer of the pattern. With a positive resist the developer removes the exposed resist while with a negative resist the developer removes any unexposed resist. Exposure and development times are dependent on the resist, UV source and developer. As a final step the sample is rinsed in deionised water to prevent any further development once the sample is taken out of the yellow room. Multiple stages of lithography are possible with sequential masks aligned via the use of alignment marks on the photomask. A Karl Suss MJB3 aligner is utilised in this work.

3.2.3 Thin Film Deposition

The deposition of thin films upon semiconductors is a vital aspect of semiconductor processing in which a variety of materials are utilised. These materials can be either dielectric material such as SiO_2 or metal contacts. There are a variety of different techniques available to achieve the desired result, which will be used for the project and thus be introduced below

Plasma Enhanced Chemical Vapour Deposition

A plasma enhanced chemical vapour deposition (PECVD) is based on a technique with a mechanism which is similar to that of a reactive ion etcher in regards to the utilisation of plasma. Within a device chamber there are two parallel electrodes, gas inlet/outlet pipes and an RF generator.[8] In comparison to chemical vapour deposition (CVD) the introduction of the plasma allows a reduction of the growth temperatures of the thin films.

PEVCD is commonly used for the growth of dielectric materials, typically, SiO_2 or Si_3N_4.[9] Reactant gases (SiH_4, N_2, N_2O) are injected into a chamber resting at an elevated temperature (~300 °C). An RF generator is used to create the plasma within the chamber generating a bias between the upper and lower electrodes. The reactive gas mixture, containing radicals, ions, atoms and molecules will then interact with the substrate surface. The diffusion of the reactive species to the sample surface then results in a surface reaction forming the required film.[8] Specification of the conditions within the chamber – flow rate, temperature, RF power – allows the deposition rate to be controlled and precise growth rates can be achieved allowing the growth of high quality thin films.[10] Within this work, PECVD has been typically utilised for the growth of silicon dioxide layers.

Thermal Evaporation

Thermal evaporation is a physical vapour deposition method widely utilised for the deposition of a variety of metals. The material to be deposited is fitted within the deposition chamber, typically a piece of metal wire inserted into a tungsten filament, and the sample is located at the base of the chamber.[11] A high vacuum (~3_x10^{-6} torr) is required for deposition in order to significantly reduce or eliminate disruption as a result of the residual gas in the chamber. The solid material is then heated via passing a current (~20-40 A) through the tungsten coil, melting the solid material and thus creating an atomic vapour within the deposition chamber. Due to the directionality of the deposition, the vapour cloud condenses on the surface of semiconductor samples, forming a thin film on the sample.[12]

A crystal thickness monitor is located beneath the filament, and employed to monitor the deposition thickness throughout the process. Films range from a few nanometres through to micrometres and multiple materials can be deposited in a single deposition. An Edwards E306a deposition system is implemented in this work.

E-beam Evaporation

An E-beam evaporator is another physical vapour deposition technique operating in a similar manner to a thermal evaporator, with a highly energised electron beam implemented instead of a resistive coil in order to generate atomic vapour. In contrast to the thermal evaporator, the material source is located at the base of the chamber and the samples located above the source. Deposition material is placed into a crucible which is then inserted into the chamber. A high vacuum is also required in this deposition process. An electron gun, operating at about 10 kV, is fired at the crucible atomising the deposition material.[11] A crystal thickness monitor is again utilised to monitor the deposition rate and film thickness. .

Sputter Deposition

Another physical vapour deposition technique, this involves the use of a sputter target and deposition substrate. A high vacuum is achieved prior to deposition and then an inert gas is fed into the system at a specified flow rate. A current is applied between the target (cathode) and sample platter (anode) which ionises the inert gas creating a plasma.[11] The plasma impacts the sputter target ejecting atoms into the chamber. The ejected atoms deposit on top of the sample surface forming a thin even material layer. Various materials are available to sputter, however it is metal films of Ti, Au and Ni that are fabricated in this work.

3.2.5 Rapid Thermal Annealing

It is often necessary to quickly heat or cool samples during processing, either as a fabrication step or alloy metallisation in the formation of ohmic contacts. One method is via rapid thermal annealing (RTA) in which higher temperatures (300-900 °C) are achieved in a matter of minutes evenly heating the sample. The RTA operates with the use of two silicon susceptor wafers, separated by a small air gap with the sample residing on the lower wafer. Once entered into the chamber, the banks of infra-red bulbs are initiated, radiatively heating the silicon wafers. The chosen gas, N_2, N_2/O_2 mix, is passed through the chamber. The lower wafer passes heat into the sample while the upper wafer will radiatively heat the area above the sample. The

temperature is controlled by the use of a pyrometer. Following the rapid heating, the sample is cooled with high flowing nitrogen.

3.3 Characterisation

Assessment of the fabricated devices is an essential requirement in semiconductor processing. There are a number of characterisation techniques to completely assess the full performance of the device. Optical techniques provide non-destructive feedback on the material properties, such as information regarding the band gap or stresses in a system. Solar hydrogen naturally involves the use of light and therefore optical characterisation results in knowledge on the performance of a device.

3.3.1 Photoluminescence

Photoluminescence (PL) is a very powerful technique to study optical properties of semiconductors. A PL system consists of an excitation source, typically a laser whose energy should be high enough to excite the material under study, a monochromator which can disperse the emission and a proper detector which can detect the emission. For GaN whose band edge is around 3.4 eV (or 362 nm), a 325 nm laser or any laser whose wavelength is shorter than 362nm is utilised to allow electrons from the valence band to be promoted into the conduction band. The schematic of a typical system is illustrated in Figure 3-2.

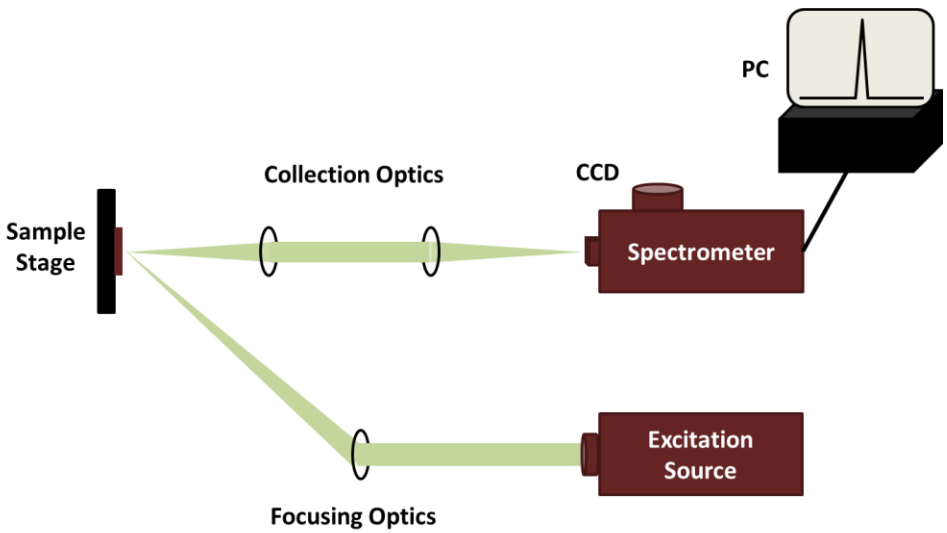

Figure 3-2 – Schematic of Photoluminescence experimental set-up

In quantum well samples due to the structure of the semiconductor, excitation with a laser suitable for GaN emission will result in reduced absorption of the InGaN quantum wells due to absorption by the GaN capping layers. Therefore a 375 nm (or any laser >362 nm) laser is utilised, passing through the GaN resulting in excitation of the carriers in the quantum well only allowing the properties of these structures to be investigated.

3.3.2 Scanning Electron Microscopy

High resolution images are required in order to assess semiconductor nanostructures. Scanning electron microscopy (SEM) works by focusing a beam of electrons onto a sample surface producing resolutions on nanometre scales.[13] Operating within a vacuum, a steady stream of electrons is required. A field emission gun (FEG) is utilised in this research which operates via the formation of a strong electrical field to remove electrons from their associated atoms. A series of magnetic lenses focuses the electrons into an electron beam which is then centred onto the sample. The interaction of the electron beam with the sample surface ejects secondary electrons which are then sensed with the secondary electron detector and the intensity is monitored. The signal is amplified and processed to produce an image depicting the surface of the sample. The difference in contrast ratios is dependent on the number of secondary electrons detected.

3.3.3 Atomic Force Microscopy

Atomic force microscopy (AFM) is a beneficial tool in non-destructively assessing the sample surface, providing topographic information difficult to obtain in other microscopy techniques. The initial AFM utilised a scanning tunnelling microscope in tandem with a surface profiler[14] and the basic principle is still utilized in which a cantilever and feedback mechanism is used to assess physical properties of a sample, including atomic growth steps. On the cantilever is a minute tip, typically made from silicon. As GaN is a very hard material, standard silicon tips can be easily damaged. Therefore, to assess the surface of nitrides a silicon tip with a SiN coating is implemented. As the probe scans the surface of the sample, interactions between the probe and the sample cause deflections of the cantilever. A laser is utilised to

evaluate and monitor the deflection during a scan. This happens by reflecting the laser spot on the back of the cantilever, providing feedback during the scan to maintain the minimum distance between the sample and surface. Operation of the AFM can occur via contact or non-contact techniques in which the probe tip is either above or directly on the sample.

3.4 Photoelectrochemical Techniques

Accurate characterisation of the device performance is essential to determine areas for improvement. Within this work, a number of different photoelectrochemical (PEC) measurement techniques were implemented in order to obtain a variety of information regarding the working potential of the fabricated devices.

3.4.1 PEC Cell

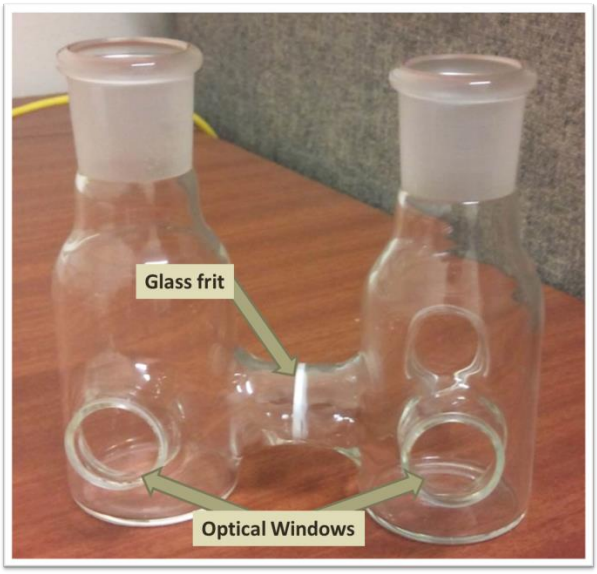

Figure 3-3 - Photograph of photoelectrochemical cell utilised in majority of testing

With the vast quantity of research in the area of photoelectrochemical procedures there is an array of different PEC cells implemented in this research.[15] Initial work was conducted on a single windowed Perspex reactor in which the working electrode (the fabricated sample) and the counter electrode (Pt rod) were located in the same compartment. This simple design provided a basic analysis approach for the materials.

The second revision of the reactor was comprised of a two compartment cell to separate the working and counter electrodes (Figure 3-3). This was a custom made design of borosilicate glass with three UV fused silica optical windows. The compartments are separated via the use of a glass frit to reduce the flow of generated gases between compartments and to allow better quantification of the separate gases. A plastic sample holder is located into the base of one of the compartments in order to secure and maintain the same sample position throughout all testing. A schematic of the test set-up is illustrated in Figure 3-4. In this example an *n*-type semiconductor is acting as the working electrode resulting in the formation of oxygen at the sample and hydrogen generated at the platinum counter electrode. A 300 W Xe lamp with solar filter acts as the light source and a Keithley 2401 source measure unit both supplies bias voltages to the system and measures the current. An electrolyte, typically an acid or base acts as the medium between the working and counter electrode.

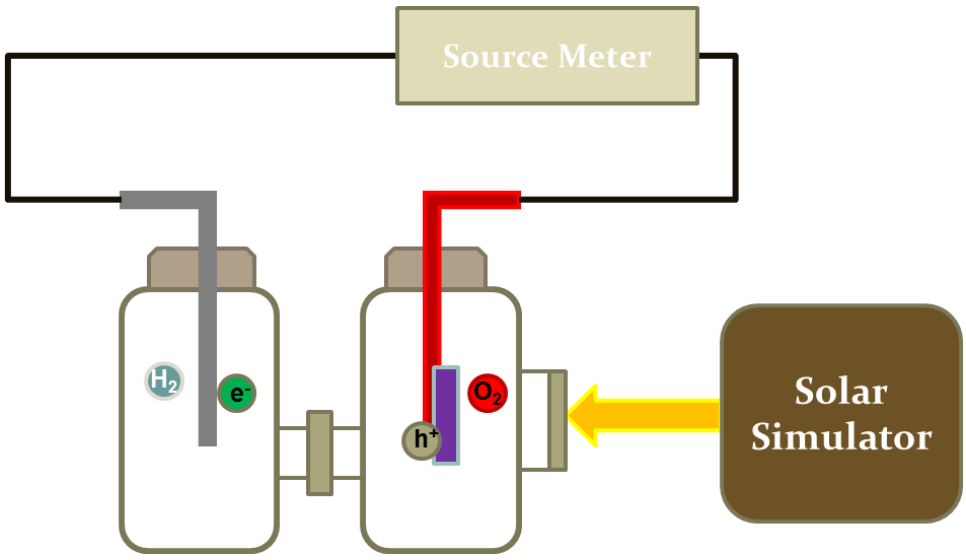

Figure 3-4 – Schematic of Experimental Set-up with an *n*-type semiconductor

3.4.2 Step Voltage Testing

Optimum conditions for device performance would be hydrogen production under solely the power of the sun. However, for some material classes, improved efficiencies can be obtained when a bias voltage is applied. As discussed in Chapter 2, a minimum of 1.23 V is required to electrolyse water and therefore any bias below that has the potential of being beneficial.

To investigate this, with the experimental set-up described above and demonstrated in Figure 3-4, a stepwise measurement of photocurrent under different applied biases is tested. Biases of -1 V to 2 V in linear step increments are supplied by the Keithley and the photocurrent measured at each step. An illumination intensity of 100 mW cm^{-2} with a solar filter acts as the light source and demonstrates the potential of the device under normal operating conditions. The overall efficiency of the device can be calculated via Equation 2-7.

3.4.3 Reliability Testing

Typical operating times required for these devices will be hundreds of hours and therefore assessing the long term stability and their potential for hydrogen production over time is essential. The test is conducted in a similar manner to the step voltage testing however a single bias voltage is chosen and applied for the duration of the test. The photocurrent is measured over a prolonged period of time, taking measurements at regular intervals. Rapid assessment of device stability is conducted with the use of increased illumination intensity, representing an increased number of PEC cycles.

Hydrogen Monitoring

In tests in which hydrogen generation is assessed, a long term test is conducted however the volume of hydrogen is collected. Prior to testing, the electrolyte is purged with nitrogen to reduce any dissolved oxygen. The platinum counter electrode is located in an upturned burette in order to collect any gas produced. The gas (hydrogen) collects within the burette and displaces the solution into the main cell compartment to allow monitoring over the course of the reaction.

3.4.4 Incident Photon Conversion Efficiency

The efficiency of a device at specific wavelengths is a useful indicator as to the operating potential of the device. The incident photon conversion efficiency (IPCE) assesses the performance of the device under single wavelength illumination (Equation 2-9). A 75 W Xe lamp is utilised as the light source and a SPEX .55 monochromator allows the selection of single

wavelengths. A calibrated photodiode quantifies the power density of incident radiation. The photoelectrochemical current is measured with a Keithley 2401. The PEC measurements were taken using the same experimental set-up implemented for all performance testing.

3.4.5 Accuracy and Error

In order to ensure accurate results and consistent data, a number of procedures were included to ensure a minimum degree of error. This was achieved by keeping all test conditions identical in a set of experiments. Any potential areas for variation were monitored and controlled to reduce error. Within an experiment, multiple measurements were conducted and the variation in data assessed to ensure it was within a defined tolerance level. Consistency checks were also carried out during measurements to ensure that all the reporting was similar to allow a comparison between measurements. Reference samples were utilised to provide a baseline value in which any exhibited change could effectively be assessed.

Bibliography

[1] B. El-Kareh, *Fundamentals of Semiconductor Processing Technology*, illustrate (Kluwer Academic Publishers, Massachusetts, 1994), p. 599.

[2] H. Jansen, H. Gardeniers, M. De Boer, M. Elwenspoek, and J. Fluitman, *J. Micromechanics Microengineering* **6**, 14 (1996).

[3] R. Legtenberg, H. Jansen, M. De Boer, and M. Elwenspoek, **142**, (1995).

[4] R.F. Figueroa, S. Spiesshoefer, S.L. Burkett, and L. Schaper, *J. Vac. Sci. Technol. B Microelectron. Nanom. Struct.* **23**, 2226 (2005).

[5] S. Grigoropoulos, *J. Vac. Sci. Technol. B Microelectron. Nanom. Struct.* **15**, 640 (1997).

[6] R.J. Shul, G.B. McClellan, S. a. Casalnuovo, D.J. Rieger, S.J. Pearton, C. Constantine, C. Barratt, R.F. Karlicek, C. Tran, and M. Schurman, *Appl. Phys. Lett.* **69**, 1119 (1996).

[7] S.A. Smith, C.A. Wolden, M.D. Bremser, A.D. Hanser, R.F. Davis, and W. V Lampert, *Appl. Phys. Lett.* **71**, 3631 (1997).

[8] P.K. Chu, X. Tian, and L. Li, in *Handb. Metall. Process Des.*, edited by G.E. Totten, K. Funatani, and L. Xie, 1st ed. (Marcel Dekker, New York, 2004), pp. 805–809.

[9] S. Arulkumaran, T. Egawa, H. Ishikawa, T. Jimbo, and M. Umeno, *Appl. Phys. Lett.* **73**, 809 (1998).

[10](2003).

[11] M.J. Madou, *Fundamentals of Microfabrication: The Science of Miniaturization*, 2nd ed. (CRC Press, Boca Raton, 2002), pp. 134–140.

[12] Z. Guo and L. Tan, *Fundamentals and Applications of Nanomaterials*, 1st ed. (Artech House, Norwood, 2009), pp. 99–106.

[13] L. Reimer, *Scanning Electron Microscopy: Physics of Image Formation and Microanalysis*, 2nd ed. (Springer-Verlag, New York, 1998), pp. 1–12.

[14] G. Binnig, C.F. Quate, and C. Gerber, *Phys. Rev. Lett.* **56**, 930 (1986).

[15] L.J. Minggu, W.R. Wan Daud, and M.B. Kassim, *Int. J. Hydrogen Energy* **35**, 5233 (2010).

Chapter 4

GaN Nanostructures for Enhanced Solar Hydrogen Production

In this chapter, a self-organised nickel mask approach developed within the group has been used to fabricate GaN nanorod arrays for use as photoelectrodes. A significant enhancement in solar hydrogen generation has been achieved as a result of using a GaN-based nanorod array in comparison with a planar one fabricated from the same parent wafer. Under identical illumination conditions in hydrochloric acid solution, the photoelectrode with the nanorod array structure has demonstrated a photocurrent enhancement with a factor of 6 and an enhancement in the rate of hydrogen generation with a factor of 7. The enhancement in solar hydrogen generation is attributed to a massive improvement in light absorption area, reduced travelling distance for the migration of the photogenerated carriers to the semiconductor/electrolyte interface and surface band bending effects.

4.1 Background

4.1.1 Nanostructures for Solar Hydrogen

The advancement of techniques for the growth and fabrication of nanostructured semiconductors has resulted in a significant increase in the design and implementation of these devices for water splitting.[1] As discussed,

water splitting is a surface reaction that requires the generation and transfer of charge-carriers to the electrolyte. The use of nanostructures in this process can result in improved device performance. Recombination of photogenerated carriers is undesirable in water splitting and therefore controlling the number of recombination centres is essential if high efficiencies are to be achieved. The properties of the semiconductor such as the grain size, surface morphology and number of defects all influence the recombination pathways. As discussed, the diffusion length of the minority carriers is a critical value if low recombination is to be obtained. Variations in the structure of the semiconductor surface can therefore strongly influence the recombination kinetics. As illustrated in Figure 4-1, for an identical semiconductor material, the electrons and holes will have a specific diffusion length, L_e and L_h respectively. In a flat surface, the number of generated carriers that will migrate to the surface is limited by the diffusion length, reducing the active region of the device to the top layer only. If a rough surface is employed, it is easier for the carriers to migrate to the semiconductor-electrolyte interface due to the increase in available sites. This increases the opportunity for reactions to occur, effectively increasing the performance of the device.[2]

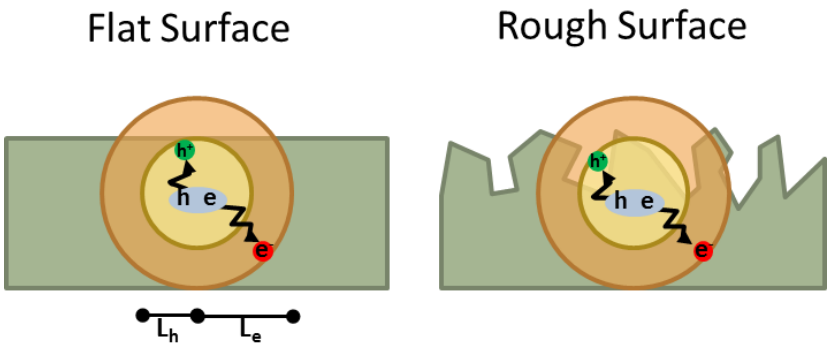

Figure 4-1 – Variation in charge collection in different semiconductor structures. L_h: hole diffusion length; L_e: electron diffusion length. Adapted from Osterloh (2013)[2]

Furthermore, the use of nanostructures can increase the light adsorption and distribution compared to flat devices.[1] Light absorption is related to the materials ability to absorb light at specific wavelengths (α) and the Beer Lambert law. The penetration of light in a material is related to α^{-1}

and a film thickness of 2.3 times this coefficient is required to absorb more than 90 % of incident light.[2] Altering the structure of the semiconductor surface can increase light absorption through scattering, reducing the loss of light that occurs due to reflection in flat surfaces. If the total amount of light absorbed increases, this will increase the number of carriers generated which will improve the device performance. The increased surface area results in a larger junction area between the semiconductor and electrolyte. This can lead to an increase in recombination due to pathways created at defects and trap sites, therefore careful control is required to optimise the nanostructured design.[3]

Despite the underlying challenges with the use of nanostructures, their potential is significant. Various device structures have been investigated for water splitting including colloidal suspensions,[4] nanorods,[5,6] nanotubes[7–9] and branched rods.[10] Varying the fabrication conditions and ultimately the morphology of the device can and has resulted in improved device performance.

4.1.2 GaN Nanorods

There are increasing activities on research into GaN nanostructures for a number of applications.[11,12] There are a number of approaches to the fabrication of GaN nanostructures, mainly based on direct synthesis and post-growth fabrication. For the former, early structures of GaN were grown with the use of a catalyst (Au,[13] Ni[14] and Ta[15]) via the vapour-liquid-solid growth mechanism. Horizontal growth of the nanorods occurs within a chemical vapour deposition (CVD) system in which the catalyst particles are dispersed on the substrate. After growth, the metal particles are found at the tops of the nanorods. Although successful devices have been fabricated by this technique,[16] the growth can result in twisting and bunching of the nanorods, undesirable for effective surface reactions. Alternate methods for GaN nanostructures include catalyst free methods in which they can be grown either via molecular beam epitaxy (MBE) or metal organic chemical vapour deposition (MOCVD).

Self-assembled growth techniques initially required stringent growth conditions if nanorods were to be grown, with the III/V ratio and AlN interlayer thickness playing crucial roles.[17,18] A nitrogen rich atmosphere produces GaN nanorods while Ga rich growth leads to thin film growth. Nanorod density and diameter could be controlled via this technique however the uniformity across a sample was poor. Selective area growth (SAG) methods were investigated with the use of patterned substrates via both MBE[19] and MOCVD[20] methods. Due to the control exhibited over the patterned substrate, a high degree of uniformity was achieved via the SAG technique and is a becoming a prevalent technology as a result of this control.[11]

Post-growth fabrication techniques exhibit a number of major advantages as MOCVD growth of standard GaN epi-wafers has been well established. Wet and dry etch processes have been employed as post-growth techniques for the fabrication of the nanorods.[21,22] One such method utilises nickel as an etch mask before ICP etching of the GaN occurs. This technique creates a relatively uniform pattern on the GaN wafer. Modifications and adaptions to this process were made to this method to improve uniformity and quality of the etched nanorods by the nitride group at Sheffield.[23,24]

GaN Nanostructures in Water Splitting

As discussed in Chapter 2, the initial focus of GaN devices were planar structures. However there has been some limited attempts at utilising nanorods or nanodots in this application.[25,26] In both cases, the growth of the nanostructures were via intensive processes such as e-beam lithography and MBE growth limiting their potential for commercial III-nitride applications.

4.2 As-Grown GaN Devices

4.2.1 Fabrication

All as-grown GaN samples were grown using an MOCVD reactor. The technique implemented has been designed by the Sheffield research group and provides superior crystal quality compared to standard two step growth

techniques.[27,28] A high temperature (1200 °C) AlN buffer layer is grown on a (0001) sapphire substrate under low pressure conditions after thermal substrate cleaning in flowing hydrogen. The V/III ratio during this step is 40. The high temperature AlN buffer layer produces an atomically flat surface as a result of two dimensional growth dominating over the standard three dimensional growth observed in standard techniques. This technique results in a significant reduction in structural defects.[29] An un-doped GaN layer is then grown upon the flat AlN layer in high then low pressure conditions. The upper active layer then follows these two procedures. For *n*-type GaN, silicon is introduced as the dopant with the silane flow rate controlled to alter the overall doping level. Magnesium is utilised as the dopant in *p*-type epi-wafers.

Following epi-wafer growth, the sample undergoes a number of characterisation steps including optical microscopy and x-ray diffraction (XRD) to assess the quality of the wafer. Samples are cleaved from the wafer using a diamond scribing pen into regular square samples of between 0.2 cm^2 and 1 cm^2. Photolithographic techniques mask off a contact area of approximately 20 % of the sample size. The ohmic contact is deposited using either a thermal evaporator or sputterer. The contact is comprised of a mixture of Ti/Au or Ti/Al/Ti/Au and is either 120 nm or 200 nm thick respectively for *n*-type wafers. A Ni/Au contact, of approximately 60 nm, acts as the ohmic contact to the *p*-type wafers. Finally an insulated copper wire is bonded to the sample with conducting epoxy before being fully insulated with a layer of insulating resin.

4.2.2 Device Characterisation

Assessment of the device properties were carried out with a number of characterisation techniques including photoluminescence (PL), atomic force microscopy (AFM) and Hall measurements.

Photoluminescence (PL)

PL measurements were conducted using a 325 nm He-Cd laser at room temperature. The light was dispersed by a .75 M monochromator and detected by a Jobin Yvon CCD. The observed spectrum is comprised of two

main peaks (Figure 4-2), the near band-edge emission and a broad yellow band emission. The near band-edge emission is centred at 361 nm, close to the expected band gap of GaN at 300 K of 3.437 eV (360.73 nm).[30] This luminescence has been attributed to a free exciton transitions and donor-bound excitons.[31]

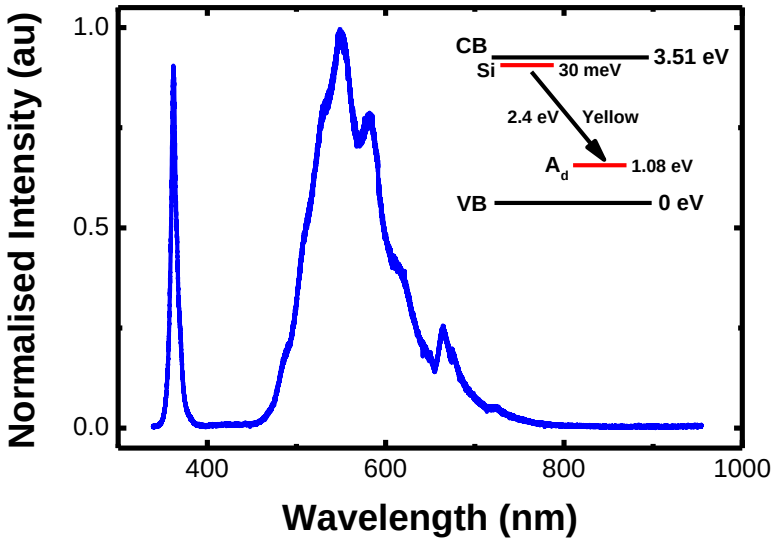

Figure 4-2 – Room temperature photoluminescence of silicon doped GaN (inset) schematic of donor-acceptor recombination model in *n*-GaN

The yellow band emission is broadly centred at 550 nm, which can be typically observed in silicon doped GaN as a result of silicon-induced deep levels.[32,33] The emission is due to a donor-acceptor mechanism creating a shallow and corresponding deep centre, demonstrated on inset of Figure 4-2.[34] The recombination between these two donor states causes the broad yellow band visible in silicon doped GaN and was initially identified in 1980.[35]

Atomic Force Microscopy (AFM)

AFM provides detailed topographic information regarding the quality of the material surface as well as distinguishing any features such as defects, growth steps and surface roughness. A typical surface of *n*-type GaN is illustrated in Figure 4-3. In Figure 4-3 (b) the growth steps are clearly visible despite little variation in actual height. The average surface roughness for the as-grown wafers used in this work is typically 0.2 nm. This illustrates a good

quality GaN sample and is attributed to the growth technique utilised,[27] minimising defects within the crystal lattice.

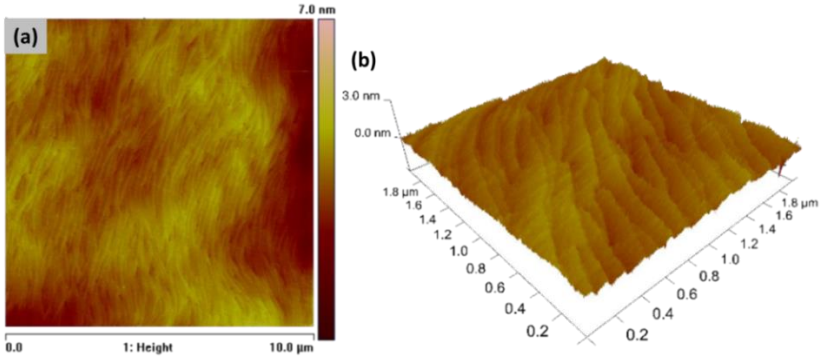

Figure 4-3 – AFM scan of *n*-type GaN wafer (a) 100 µm^2 surface profile (b) 3D topography of 4 µm^2 scan

Hall Measurements

To assess the level of doping of the as-grown material Hall measurements were conducted. The dopant level of *n*-type GaN has been shown to have a significant effect on photocurrent[36] and therefore it is a necessary step to clarify potential device performance. Carrier concentrations of the MOCVD grown GaN were determined via the Van der Pauw method. This technique involves the deposition of four contacts in the corners of a uniform piece of wafer. 5 x 5mm pieces of GaN wafer were thoroughly cleaned by the three solvent methodology described previously, before small pieces of indium were physically contacted to the corners of the GaN. Vertical and horizontal voltage measurements were taken under 0.2 mA of applied current across the different contact positions of the sample. Measurements between the corners of the sample were also taken under the effect of a positive and negative magnetic field. For all measurements, a 0.556 T magnet acted as the source of the field.

As a result of increased resistance at lower carrier concentrations and increased recombination rates at higher concentrations, there is a tipping point in which the optimum value can be attained. Figure 4-4 illustrates the variation between carrier concentration and current density in non-biased conditions. There is a clear trend between carrier concentration and current even across data sets, with a potential shift around a median for different

growth conditions. The optimum value however is approximately $2x10^{17}$ cm^{-3}. The shaded area illustrates the region in which the *n*-type GaN samples utilised in this work fall, with carrier concentrations around $2x10^{18}$ cm^{-3}, a factor of 10 above the optimum value. Based on these values, the current densities will be approximately half that under potential optimum doping conditions.

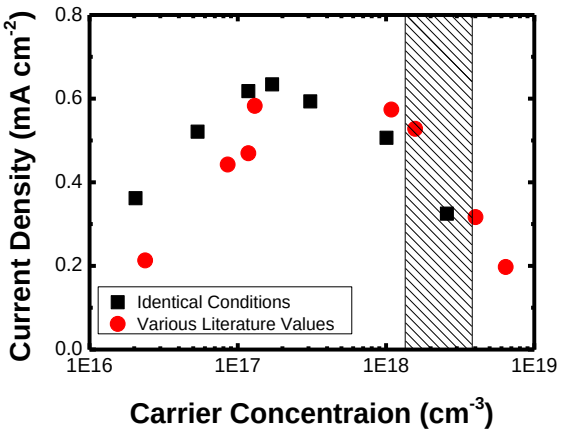

Figure 4-4 – Variation in current density with carrier concentration of different samples at 0 V bias in 1 M HCl under 150 W Xe lamp illumination, black squares indicate samples from same test run, red circles are literature values of various tests. Shaded area indicates carrier concentration of devices used in this work. Adapted from Ono *et al.*. 2007[36]

4.2.3 Solar Hydrogen Performance

Electrochemical measurements of as-grown devices were performed in the experimental set-up described in Chapter 3.

Preliminary Measurements

Stepwise measurements of as-grown *n*- and *p*-type GaN were conducted in a 1 M HCl electrolyte solution under illumination and dark conditions. Photocurrent measurements from -1 V through to 2 V were measured in 0.2 V steps. In dark current measurements, all sources of illumination were minimised and an equilibrium condition obtained. Multiple measurements were taken at each step to ensure accuracy within test data. Nominally low dark current measurements were recorded for both the *n*- and *p*-type GaN devices (Figure 4-5). Increases in dark currents are observed above the required potential to split the HCl electrolyte solution of 1.4 V, consistent with expected results.

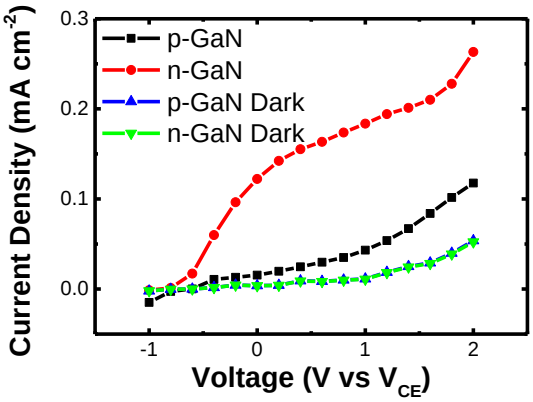

Figure 4-5 – Dark and light photocurrent measurements of as-grown *n*- and *p*-type GaN devices in a 1 M HCl electrolyte solution. Illumination intenstiy was 100 mW cm-2.

Illumination tests were conducted with a 300 W Xe lamp with a solar filter applied. The use of a solar filter matches the output of the light source to that of global irradiance observed at the Earth's surface. Under these conditions less than 2 % of the incident radiation is at wavelengths applicable to GaN. A power density of 100 mW cm^{-2}, corresponds to the output of one sun and relates to approximately 2 mW cm^{-2} of useable radiation. Under illumination, the turn on voltage of the *n*-GaN is -0.6 V and -0.4 V for *p*-GaN. The difference in turn on voltage is a result of the shifted conduction and valence band positions of the two doped materials. Under zero bias there is a considerable difference in the obtained photocurrent of the two devices. The *n*-type sample demonstrates a photocurrent 8 times higher than *p*-type GaN. This result is comparative to other literature values in which the performance of *p*-type GaN is significantly lower than that of *n*-type GaN.[37] This has been widely accepted to be a result of the higher carrier density of *n*-type GaN resulting in a reduced resistance compared to the *p*-type GaN.

As a result of the surface reactions occurring at the interface between the *p*-type GaN and electrolyte, the build-up of electrons at the surface forms a protective barrier and prevents anodic etching of the GaN.[38] This suggests that *p*-type GaN could be the ideal electrode but due to material constraints and the demonstrated photocurrent, the focus of this thesis has been on *n*-type GaN and InGaN/GaN multi-quantum well (MQW) devices. As discussed the efficiency of the device can be calculated using the following equation,

$$\eta = j_p(1.23 - V_{ext})/I_0$$

Equation 4-1 – Photon to current efficiency equation of a photoelectrochemical cell under applied external bias

The calculated maximum efficiency for the devices using Equation 4-1 is 0.17 and 0.03 % for the *n*- and *p*-type devices respectively.

In order to determine the activity of the device for hydrogen production a typical *n*-GaN sample is utilised. Measurements were conducted at elevated light intensities (700 mW cm^{-2}) and an applied bias of 0.8 V to achieve a significant volume of hydrogen in a shortened time. The volume of hydrogen was measured via the previously discussed method. The sample underwent 50 minutes of testing in a 0.5 M HCl solution and hydrogen measurements were taken at periodic intervals through this time. The theoretical value of hydrogen is obtained using the current produced during the test (Figure 4-6(a)) and Equation 2-8). As presented in Figure 4-6(b) the volume of hydrogen collected is very similar to the theoretical value and the final volume is almost identical to the total possible volume. This suggests an almost 100 % conversion rate of the photocurrent to hydrogen indicating the potential of our *n*-GaN sample and device processing technique as a photoelectrode for hydrogen production.

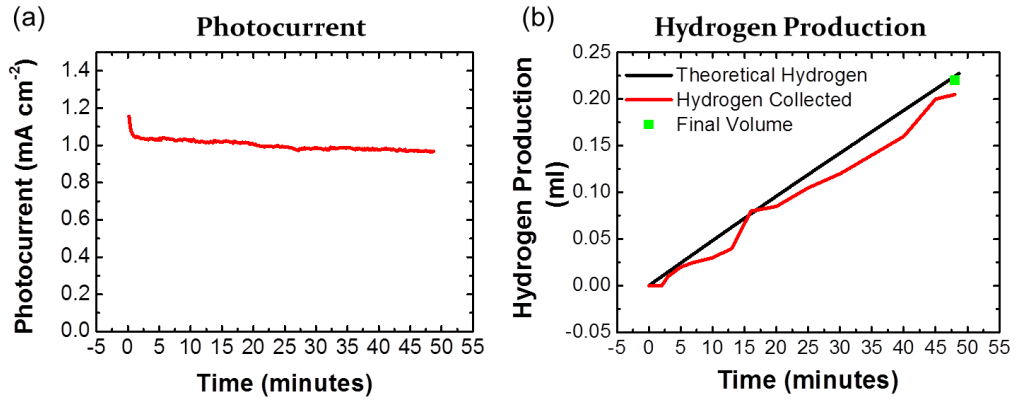

Figure 4-6 – Photoelectrochemical water splitting of 0.5 M HCl with *n*-GaN electrode under ~500 mW cm^{-2} and 0.8 V applied bias (a) photocurrent density (b) Theoretical and actual hydrogen production

Electrolytes

The role of the electrolyte is crucial in delivering high energy conversion efficiencies as well as reducing the dissolution of the material. The concentration and type of electrolyte plays a significant role in terms of material viability and therefore it is important to choose a suitable electrolyte. Ideally sea water and other water sources would be utilised due to their low cost, abundance and chemical neutrality however due to low ion concentration, high conversion efficiencies are required to make this a viable option. Sea water has a typical salinity of 3.5 % equivalent to 0.6 M. The majority of the ions are sodium and chloride however there is a variety of other materials that make up the total. Various electrolytes are currently in use across literature and range in pH from acidic to basic solutions.

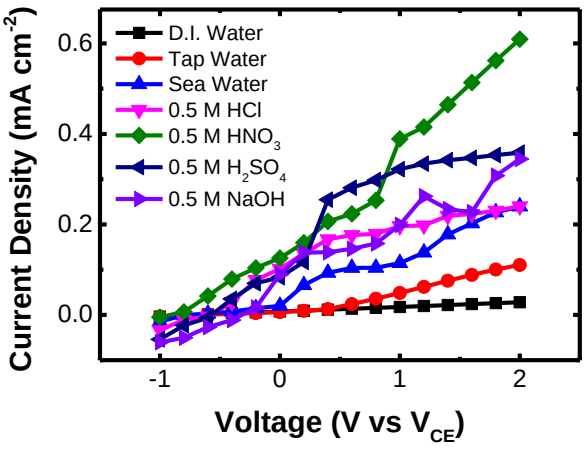

Figure 4-7 – Photocurrent densities of *n*-GaN with different electrolytes under 100 mW cm^{-2} AM1.5 Xe lamp illumination

Photoelectrochemical measurements were conducted using a series of *n*-GaN samples fabricated from the same epi-wafer. Various acidic and basic electrolytes were tested at concentrations of 0.5 M, approximately the level of sea water, against three water samples. De-ionised water was used as a standard with tap water and a sample of sea water also tested. Each sample was tested at step measurements from -1 V to 2 V under 100 mWcm^{-2} of filtered illumination (Figure 4-7). As expected the deionised water demonstrated a nominal photocurrent due to the lack of ions in the solution. This was mirrored with the tap water in which system resistances meant the production of photocurrent was not observed until 0.6 V vs V_{CE}. A sample of

sea water taken from off Sagami Bay, Japan was utilised. Due to the increased salinity and therefore ion concentration of this sample compared to the standard D.I. water (around 0.02 M) there is at least a 200 % increase in photocurrent densities. Despite the increased ion concentration, the photocurrent of sea water is still comparatively low compared to other electrolytes. The performance in sea water does however does reach around 60 % the performance of HCl indicating the potential opportunity to utilise sea water as the electrolyte in the future for high efficiency devices.

Table 4-1 - Reduction half reactions and potentials of 1 mol dm^{-3} solution under 1 atm pressure

Electrolyte	Reduction Half Reaction	E°_{red} (V)
Water	$2H_2O + 4h^+ \rightarrow O_2 + 4H^+$	1.23
HCl	$2Cl^- + 2h^+ \rightarrow Cl_2$	1.36
HNO_3	$[NO_3]^- + 4H^+ + 2e^- \rightarrow HNO_2 + H_2O$	0.93
	$HNO_2 + H^+ + e^- \rightarrow NO + H_2O$	0.98
H_2SO_4	$2[SO_4]^{2-} + 2h^+ \rightarrow [S_2O_8]^{2-}$	2.01
NaOH	$4[OH]^- + 4h^+ \rightarrow O_2 + 2H_2O$	0.40

The choice of electrolyte can play a major role in the lifetime and performance of the device as it can affect the products produced in the reaction. The half reactions and reduction potentials of common electrolytes are presented in Table 4-1. Water, hydrochloric acid, sulphuric acid and sodium hydroxide are all potential electrolytes for the stoichiometric production of hydrogen and oxygen. Nitric acid however, has a lower reduction potential than water and therefore could not effectively be identified as "water" splitting as it is not water being split. The decreased reduction potential of the device explains the higher photocurrent obtained in Figure 4-7. Although hydroxyl radicals have a lower reduction potential than oxygen, the products are identical. The paired half reaction involving the conversion of sodium ions to sodium metals requires a significantly larger potential thereby maintaining the reaction at stoichiometric levels. Hydrochloric acid poses a latent issue due to the similar reduction potential

of water. In practice, losses and conversion potentials at the electrode in the formation of oxygen result in a highly competitive reaction, resulting in the production of both oxygen and chlorine when hydrochloric acid is implemented as the electrolyte.

Despite the potential issues in the production of both oxygen and chlorine, hydrochloric acid is utilised as the electrolyte for many of the reactions reported due to the similarity to the "ideal" solution sea water. Although sodium hydroxide or sulphuric acid appear ideal, there is evidence to support the etching of gallium nitride or indium gallium nitride in these solutions reducing the lifetime of the device.[39] When no bias is applied, the values for the three best electrolytes are similar indicating only minor differences in performance can be achieved under non biased direct solar illumination conditions.

4.2.4 Summary

The preliminary measurements indicate the potential of the material with device efficiencies of around 0.2 % for the *n*-type GaN. Visible production of hydrogen has also been demonstrated with a low level of conversion loss between photocurrent and hydrogen generation. Therefore modifications to the structure of the device could help to increase the overall device performance.

4.3 GaN Nanostructured Devices

4.3.1 Fabrication

The GaN nanostructures were fabricated via the use of a self-organised nickel nanomask that was developed in our group by Bai *et al.*[24,40] on a typical MOCVD grown GaN wafer discussed previously. A schematic of the fabrication process is illustrated in Figure 4-8. Initially the *n*-GaN wafer is cleaned of contaminants with the described three stage solvent cleaning process. Photolithography was utilised to mask off a contact area which is then etched by inductively coupled plasma reactive ion etching (ICP-RIE). The etchant gas is a mixture of Cl_2 and Ar at 50 W RF power and 450 W ICP power. The contact depth and etch time is related to the required nanorod

size in order to allow efficient current flow from nanorod to ohmic contact. The sample is cleaned again to remove any photoresist and 200 nm of SiO_2 is deposited via plasma enhanced chemical vapour deposition (PECVD). The silicon dioxide is formed from SiH_4 and N_2O in a nitrogen atmosphere at an RF power of 25 W and acts as an etch mask.

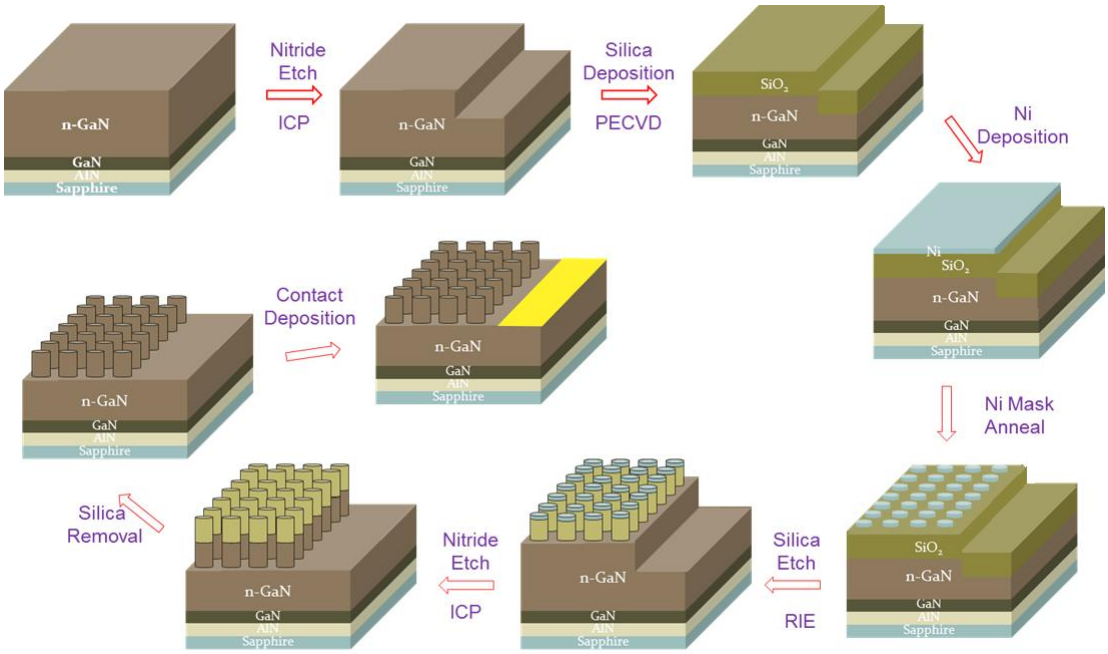

Figure 4-8 – Schematic of nanorod fabrication via use of self-organised nickel nanoparticles

The formation of the nickel nanoparticles follows via the deposition of a thin nanometre thick layer of nickel on the silicon dioxide. Thermal evaporation is the technique of choice as it provides an even layer across the intended nanorod area. Self-organisation of the nickel occurs via a thermal heat treatment in a rapid thermal annealer (RTA). Temperatures between 820 – 850 °C for 1 minute in a nitrogen atmosphere create a reasonably uniform spread of nanoparticles (Figure 4-9 (a)). The thickness of nickel and annealing conditions allow control over the nanoparticles and ultimately the nanorod size. The nickel acts as a primary etch mask to etch through the silicon dioxide. A reactive ion etch (RIE) using either a CHF_3/SF_6 or CHF_3/O_2 as the etchant gases produces the secondary etch mask (Figure 4-9 (b)). The flow rates are 30:10 sccm or 35:5 sccm respectively in a 35 mbar atmosphere.

The RF power is set at 75 W and the etch rate monitored via a laser feedback system.

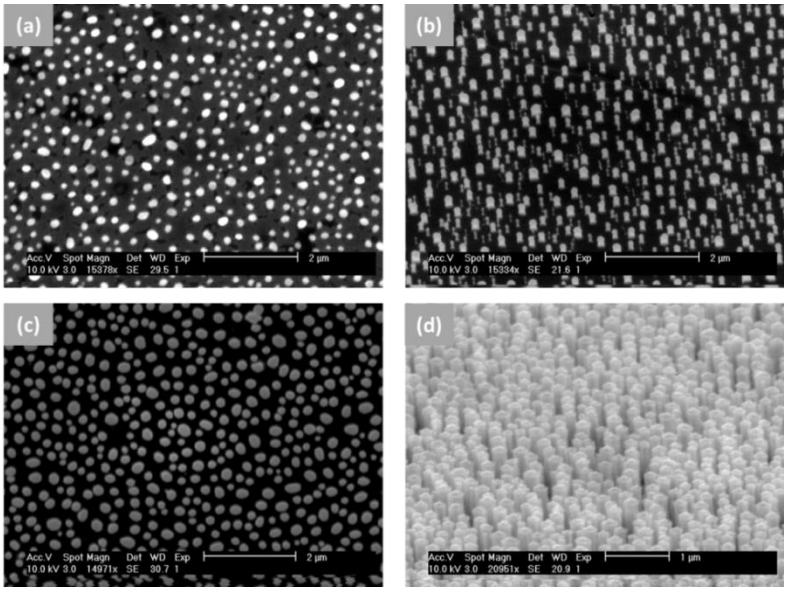

Figure 4-9 – SEM images of nanorod fabrication (a) Nickel nanoisland mask (b) Etched silicon dioxide mask (c) plan view of fabricated nanorods (d) tilted image of finished nanorods

Prior to the second ICP etch the nickel nano-islands are removed with a simple nitric acid treatment. The sample then undergoes the secondary ICP etch under identical conditions to the initial etch. A hydrofluoric acid treatment removes the silicon dioxide layer leaving the cleaned nanorods (Figure 4-9 (c & d)). An ohmic contact of Ti/Au or Ti/Al/Ti/Au is thermally deposited onto the contact area etched during the initial fabrication stages. Optical investigation during the fabrication process is carried out with a scanning electron microscope (SEM).

4.3.2 Characterisation of Nanostructures

Due to the fabrication method, a degree of control over the diameter and height of the nanorods can be obtained. Assessing the optimum performance of each condition can result in improved photocurrents for solar hydrogen production. In order to determine the positive and negative effects of the conditions, optical characterisation via SEM and PL can provide an indication behind the effects.

Nanorod Diameter

A degree of control over the diameter of the nanorods can be achieved by varying the thickness of the nickel layer thermally evaporated onto the silicon dioxide surface. As the nickel acts as the primary etch mask for the formation of the nanorods any change in this process will result in changes to the final etched GaN structure. The initial deposition creates a uniform layer across the silicon dioxide surface, annealing of the nickel follows an Ostwald ripening effect in which a decrease in the total surface energy results in the growth of larger particles.[41] As a result of the Ostwald ripening, altering the film thickness or annealing conditions leads to a change in the size of the formed nanoparticles.[42]

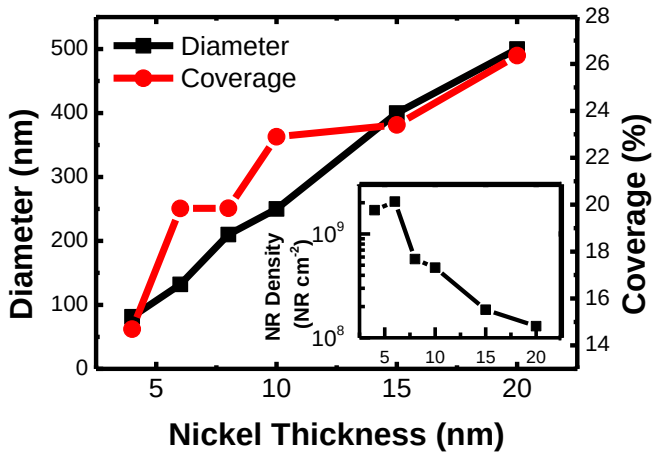

Figure 4-10 – Relationship between nickel thickness and nanorod diameter (inset) variation in nanorod density per cm^2

The original fabrication technique employed a 10 nm thick layer of nickel resulting in diameters of approximately 200 nm.[24] Varying the nickel thickness from 2 nm to 20 nm results in a significant variation in both the coverage of the final fabricated nanorods across the surface and the diameter of the nanorods. Figure 4-10 illustrates the linear relationship observed between the initial thickness and the final diameter of the nanorod. Alongside this, the total surface coverage is also displayed. As expected, as thickness increases the overall diameter of the nanorod increases. The density of nanorods across the surface indicates a negative relationship between nickel thickness and density (Figure 4-10 (inset)). With the increase

in nickel thickness, larger nickel islands form, however the distance between each particle is larger. These larger islands are formed by the coagulation of the smaller islands formed initially. This process of formation is thought to be responsible for the spread of the particle sizes (Figure 4-11).

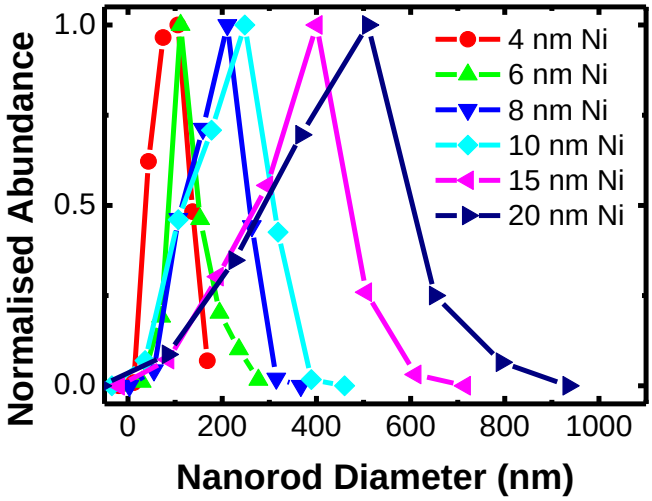

Figure 4-11 – Deviation of nanorod diameters with different nickel film thicknesses

As the size of the nickel thickness and ultimately the average size of the particles increases, there is a general trend in which the overall spread of the diameters increases. There is a clear broadening of the curves visible in Figure 4-11 with particles ranging from 50 nm through to <1000 nm when a 20 nm layer of nickel is utilized as the etch mask. The non-uniformity of the nanorods will result in various surface effects across the devices where the bend banding and depletion region associated with the semiconductor-electrolyte interface changes depending on diameter. Scanning electron microscopy of the various nanorods illustrates the variation in size caused by the deposition of different nickel thicknesses (Figure 4-12). Alongside the size dependence, the obvious reduction in density can be noted, as described in Figure 4-10 (inset), where the density decreases from a maximum of 2_x10^9 down to 1.2_x10^8 for the 6 nm and 20 nm nickel films respectively. As discussed, this is a result of the coagulation of the nickel particles, resulting in a decrease in overall nanorod numbers due to the increase in nickel thickness.

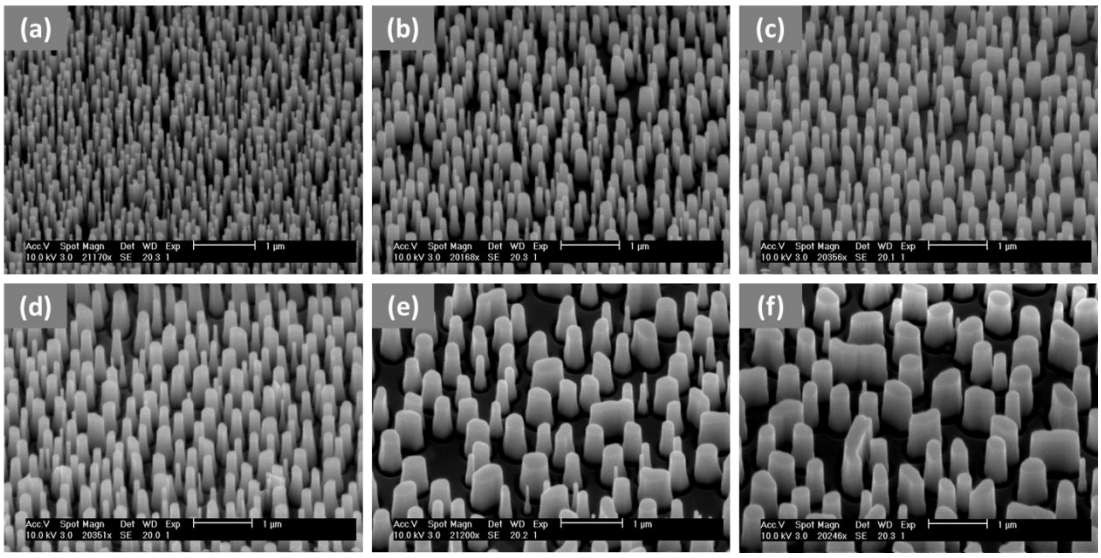

Figure 4-12 - SEM indicating nanorod size and density of various nickel mask thicknesses (a) 4 nm (b) 6 nm (c) 8 nm (d) 10 nm (e) 15 nm (f) 20 nm

Further to this, a change in the total strain in the nanorods can be observed via the room temperature photoluminescence (PL) of the different nanorod diameters. The normalised PL spectrum of each device is presented in Figure 4-13 where there is a clear increasing red shift occurring as nanorod diameter increases. This is due to the fabrication of nanorods reducing the compressive strain caused by the lattice mismatch that occurs between the GaN/AlGaN and sapphire substrate.[43,44] An estimation of the change in strain can be calculated from the shift in the PL and a proportionality factor (K), where K=21.2±3.2 meV/GPa for GaN.[45] From Figure 4-13 as the size of nanorod increases the degree of redshift and therefore reduction in compressive strain changes. For the 4 nm–20 nm nickel masks the shift ranges from 10 meV to 29.9 meV which relates to a change in strain of 0.47±0.08 GPa to 1.4±0.22 GPa respectively. The compressive strain present within a GaN substrate grown on an AlN buffer layer on sapphire is approximately 0.2 GPa for the GaN and 1.77 GPa for the AlN.[45] Therefore, the formation of the widest nanorods fabricated results in an almost complete relaxation of the strain in the sample. It is known that the compressive strain caused by the lattice mismatch causes the band gap of GaN to increase. This is a result of variations in the exciton transitions caused by the differences in the bulk material and sapphire substrate.[46,47]

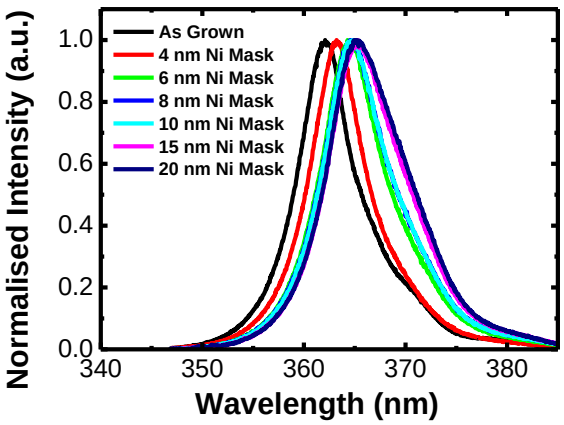

Figure 4-13 - Normalized room temperature PL of different diameter nanorods

Nanorod Height

Variation in the height of the nanorods was achieved by changing the ICP etch time. Over time, variations in conditions within the ICP chamber result in a degree of drifting in regards to etch rate. All samples fabricated during the investigation on the nanorod height were conducted sequentially allowing for direct comparison. Figure 4-14 illustrates how the etch rate affects the nanorod height with examples of the shortest (Figure 4-14 (a)) and longest (Figure 4-14 (b)) nanorods illustrated. There is a clear trend between etch time and nanorod height with an etch rate around 90 nm min^{-1}. Photoluminescence measurements of these samples were not investigated.

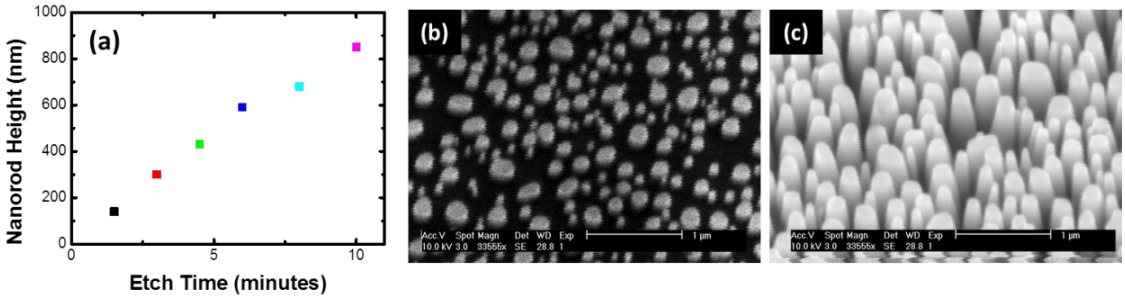

Figure 4-14 – (a) Variation of nanorod height with etch time (b) SEM of 1.5 minute ICP etch (c) SEM of 10 minute ICP etch

4.3.3 Solar Hydrogen Performance

An investigation into the effects of the nanorod diameter and height on solar hydrogen performance was investigated via the standard measurement technique described in Chapter 3.

Nanorod Diameter

As observed, a significant degree of control over the nanorod diameter can be achieved via the alteration of the nickel mask thickness. Utilising this method, an optimised size for the nanorods can therefore be assessed for solar hydrogen performance. Under the standard stepped voltage measurement technique, with a bias from -1 V to 2 V versus the platinum counter electrode applied, the difference in performance can be observed in Figure 4-15. The nanorod devices all have a delayed turn-on voltage when compared to the as-grown sample at -0.6 V compared to -0.8 V. This is caused by surface effects of the nanorods creating an additional potential barrier for the photogenerated electron-hole pairs to overcome and interact with the electrolyte. As for the variation in diameter, all nanorod device structures result in an increase in photocurrent over the reference as-grown sample due to the increase in surface area as a result of device fabrication.[48]

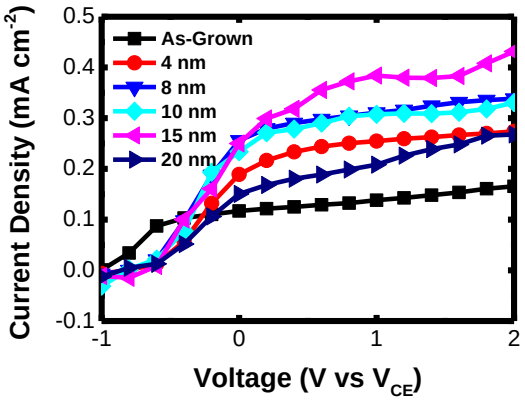

Figure 4-15 - Photocurrent values for different nanorod diameters caused by varying nickel thickness

If the increase in photocurrent was purely dependent on surface area effects then the smaller nanorods should exhibit the highest photocurrent due the largest change in surface area. The change is surface area based on nanorod density and average diameter is +3.47 cm^2, +6.6cm^2, + 2.7cm^2, +2.7cm^2, +1.6cm^2 and +1.7cm^2 for the 4-20 nm nickel films respectively. Therefore additional affects ultimately result in the wider (15 nm nickel film) nanorods generating the largest photocurrent. This is in part due to the number of effects discussed previously including the change in flux of the

system, the light distribution and the charge transfer properties. The minority carrier diffusion length for *n*-type GaN has been calculated around 250 nm.[49,50] As the nanorod diameter increases so does the distance that holes generated in the centre of the rod have to migrate. For the largest sample, the average diameter was equivalent to twice the diffusion length. As a result, carriers generated deep within the nanorod have a significantly higher chance of recombination than those at the edge. Similarly, nanorods that are smaller in diameter have decreased pathways for the holes to migrate, decreasing recombination. From the results, the nanorods approximately 1.5x the minority diffusion length prevent bulk like recombination that is observed at higher diameters.

Alongside the surface area and diffusion length, the absorption properties of the material have to be considered. A sufficient thickness of material is required to absorb the majority of incident radiation. The light penetration depth of GaN in which the intensity drops to 1/*e* of the original value is 0.1 μm.[51] In order to ensure >90 % absorbance, the film is required to be around 0.23 μm.[2] Based on these values, it is clear that until the nickel mask thickness increases to ~10 nm, the rods are smaller than the ideal film thickness. The combination of the light absorption, surface area and diffusion effects provides an explanation for the variation in photocurrent observed in Figure 4-15.

Height Optimisation

As with the diameter, control over the height is easily achievable. Variation in the nanorod height will again alter the total surface area of the device as well as the distances the generated carriers are expected to migrate. Standard step-voltage measurements were conducted on the fabricated samples (Figure 4-16). The turn-on voltage for all the nanorods are similar as expected due to the identical diameter resulting in similar depletion and surface effects. As with the changes to the nanorod diameter, variation in the height will not only alter the surface area of the sample but the recombination and light absorption effects. The optimum height for the GaN device is between 500-800 nm with a similar performance observed for

the three samples fabricated in this range. This is attributed to the increase in light scattering resulting in a greater number of charge carriers being generated.

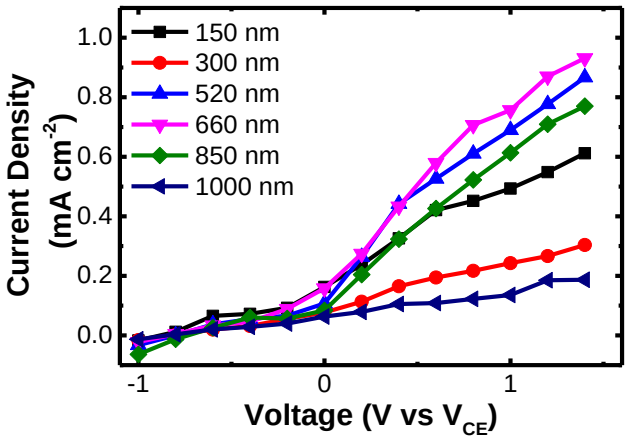

Figure 4-16 – Variation in etch depth of GaN nanorods

As the size of the nanorod increases, the contribution of the bulk material to the photocurrent decreases due to the variations in flux. Figure 4-17 illustrates how flux changes as the nanorod height increases. For the larger sample, the penetration of the light, omitting scattering effects, is only at the tops of the nanorods and the flux of the sample is lower per unit area. Changes in flux leads to variations in the open circuit voltage of a cell which will ultimately impact on the thermodynamic driving force of water splitting.[2] This partially explains the decrease observed in the larger nanorods. Other factors include recombination effects. As the size of the nanorod increases total surface area increases which can also result in an increase in the number of defects at the surface. As the etch depth increases, there is a greater chance for crystal defects to permeate the surface creating recombination centres. The increased recombination will ultimately reduce the available carriers for surface reactions decreasing the photocurrent. The optimum conditions balance all effects, combining a high active surface area with lower defect densities and adequate flux to provide a maximum value. It is postulated that the low photocurrent observed for the 300 nm device is due to the dominance of recombination effects over the positive benefits observed from changes to the device structure.

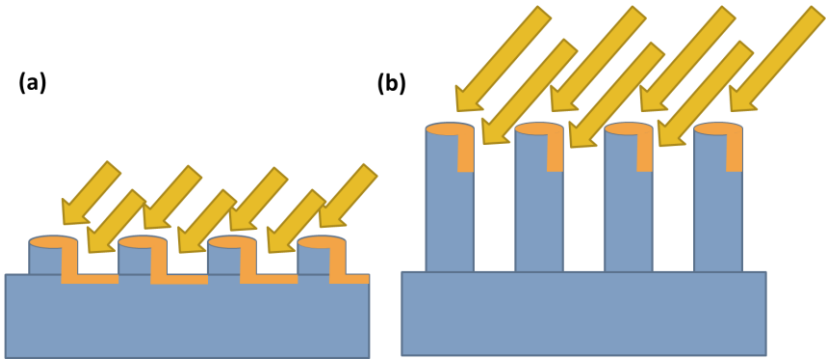

Figure 4-17 – Changes in absorbed flux of different nanorods (a) 150 nm nanorods (b) 1000 nm nanorods

4.3.4 Summary

The fabrication of a nanorod device structure has demonstrated significant benefits in terms of photocurrent compared to the as-grown device. The method of fabrication is relatively simple and includes an easy process to control both the diameter and height of the nanorods. Optimising these conditions has resulted in an increase in device efficiencies from 0.2 % up to 0.46 % illustrating the potential of GaN nanorods.

4.4 InGaN/GaN in Water Splitting

The work on InGaN/GaN devices is limited with only a small number of research groups utilising this material. The initial work by Beach[52] identified the potential of the material and following that, the majority of work has been completed on bulk InGaN/GaN films. The performance of these films has generally been relatively poor.[53–55] Recently the use of InGaN nanodots and MBE grown InGaN nanowires have shown some promise[56,57] however as previously discussed the commercial viability of this technique is not ideal. Previous work on InGaN/GaN quantum wells demonstrated a slight enhancement over bulk GaN with some variation between samples of different quantum well barrier heights.[58] Investigations into MQW nanostructures have not previously been investigated.

4.4.1 Fabrication of InGaN/GaN MQW Devices

The epi-wafer used was grown on c-plane sapphire substrates via a standard metal organic chemical vapour deposition (MOCVD) technique. The wafer has a typical optical device structure (Figure 4-18), which consists of 1.4

μm undoped GaN buffer, followed by 2.8 μm silicon doped GaN (*n*-GaN), a thin $In_{0.05}Ga_{0.95}N$ strain released layer and 10 periods of InGaN/GaN (2.5 nm/13.4 nm) multiple quantum wells (MQWs). A typical AlGaN layer of ~20nm was used as an electron blocking layer (EBL). The sample was finally capped with 200nm of magnesium doped GaN (*p*-GaN). This is a typical LED device structure and therefore the fabrication described is applicable to a large array of commercially available wafers. As-grown and nanorod devices were fabricated via the method described in Figure 4-8 resulting in two distinct samples.

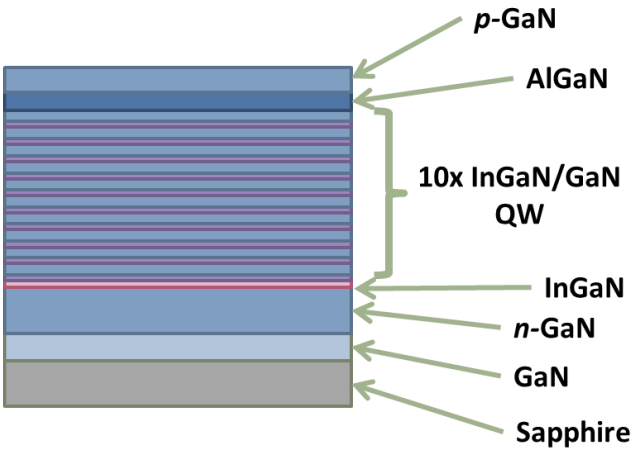

Figure 4-18 – Structure of InGaN/GaN MQW wafer

4.4.2 Characterisation

Optical characterisation of the samples was conducted via PL and SEM analysis (Figure 4-19). Photoluminescence measurements were carried out at room temperature with the use of a 375 nm diode laser. From Figure 4-19 (a) a clear peak at 467 nm is observable for the as-grown device which corresponds to a band gap of 2.66 eV, which is approximately a 16% indium composition. This shift in wavelength increases the amount of available energy by a factor of 4 compared to the GaN band gap. Typically, the fabrication of nanorods results in an enhancement in the PL emission[40] due to the increase in internal quantum efficiency, surface area and a reduction in total internal reflection. Furthermore, as observed in the GaN nanorods, the nanorod structure provides strain relief to the wafer. As previously discussed, a piezoelectric field exists within the InGaN/GaN quantum well

structures due to strain, creating a red shift of the emission peak. The observed blue shift of the nanorod structure illustrates that strain within the device has been relaxed.[24] SEM investigation (Figure 4-19 (b)) illustrates the uniformity and structure of the fabricated nanorods. The nanorods had a height of 700 nm, a diameter of 200 nm and a density of $6x10^8$ cm^2. This provides an additional 2.75 cm^2 per cm^2 of active surface compared to the as-grown structure.

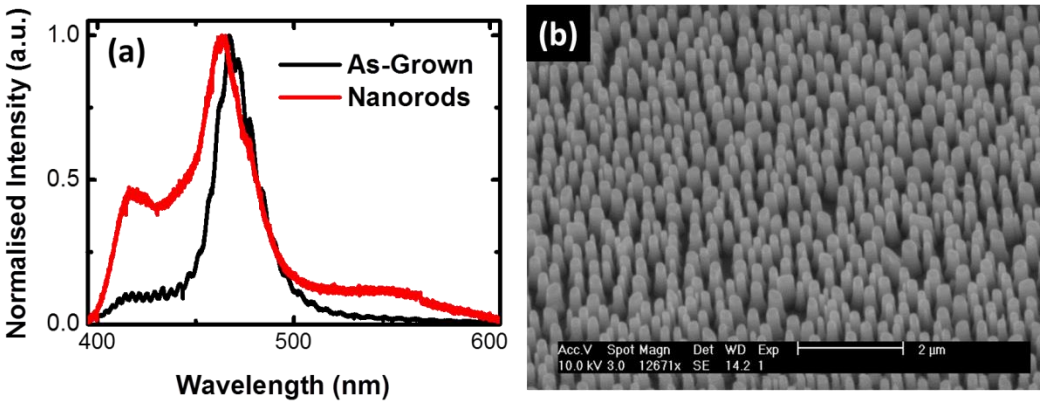

Figure 4-19 – Characterisation of InGaN/GaN MQW samples (a) normalised room temperature PL measurements of as-grown and nanorod devices (b) SEM image of fabricated nanorods

4.4.3 Solar Hydrogen Performance

Photocurrent and hydrogen measurements were conducted on the planar as-grown structure and nanorod devices. Step-voltage measurements were conducted at 100 mW cm^{-2} of solar illumination in a 0.5 M HCl electrolyte solution. The obtained photocurrents for the two devices are demonstrated in Figure 4-20. Dark photocurrent measurements were conducted with the absence of illumination in a darkened room. Both of the fabricated devices demonstrate low dark current measurements indicating good insulation of the contact and minimum leakage measurements. The obtained photocurrent of the planar as-grown device is comparable to the literature value obtained for a MQW sample operating in similar, but unfiltered illumination conditions.[58] The device performs relatively poorly due to the high resistance exhibited in the sample and the localisation of the carriers. Due to the quantum well structure and the GaN barriers, the photogenerated carriers in the quantum wells face a potential barrier to

escape the well resulting in recombination of the carriers and hence low conduction values.

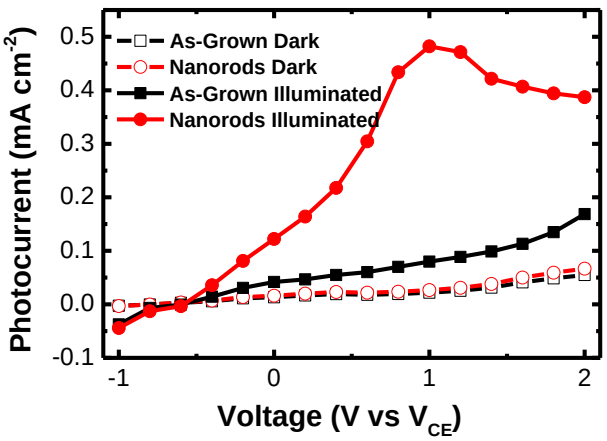

Figure 4-20 – Photocurrent of as-grown and nanorod photoelectrodes as a function of bias under 100 mW cm^{-2} illumination and "dark" conditions

The fabrication of the nanorod structure has demonstrated a significant enhancement over the as-grown device after turn on at -0.6 V. At zero bias the enhancement is proportional to the increase in surface area with an enhancement factor >3. As the applied voltage increases the improved photocurrent exhibited from the nanorod device increases further to a maximum enhancement of 6x at 1.0 V. The photocurrent of the nanorods decreases at voltages around the redox potential of water (1.23 V) which has been attributed to the decomposition of the nanorods due to photocorrosion.[26] An enhancement of 6x cannot solely be attributed to the increase in surface area (3.75 x). The fabrication of the nanorod increases the contact area of the device with the electrolyte which results in exposure of the quantum wells. The diffusion length of InGaN has been reported to be as short as 50 nm,[49,59] therefore with nanorods of 200 nm in diameter this allows for an increase in the extraction of carriers compared to the planar device. Additionally, surface band bending as a result of the nanorod fabrication[60] enhances the separation of the photogenerated electron-hole pairs increasing the recombination lifetime. These factors contribute to the increased current density. The efficiency of the devices at the maximum photocurrent value of 0.8 V are 0.042 % and 0.26 % for the as-grown and nanorod device respectively.

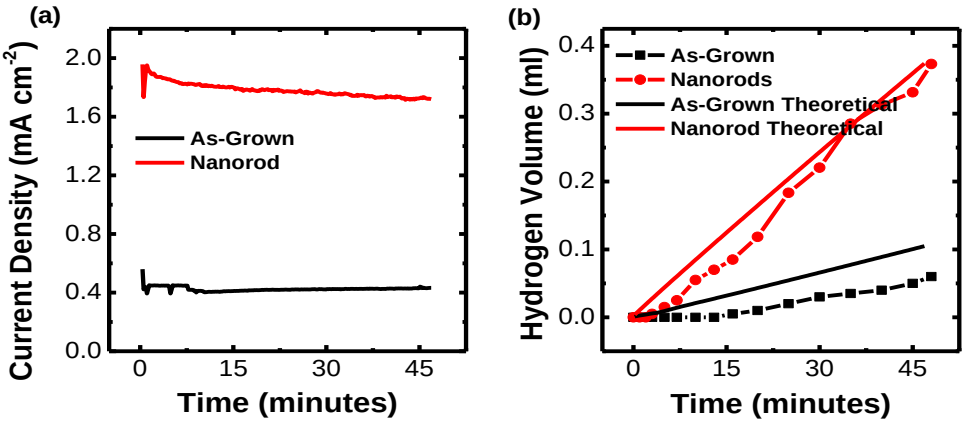

Figure 4-21 – Photoelectrochemical measurements under 400 mW cm^{-2} illumination and 0.8 V bias (a) photocurrents of the as-grown and nanorod sample as a function of time (b) obtained and theoretical hydrogen measurements as a function of time

The stability and potential of the nanorod devices for hydrogen generation were evaluated at elevated powers of 400 mW cm^{-2} illumination intensity and 0.8 V (Figure 4-21). Photocurrent was measured for a 50 minute period and hydrogen collected via the use of an upturned burette over the platinum electrode. A reduction in photocurrent is observed in both the as-grown and nanorod structures over the course of the 50 minute test duration of 3.5 and 9.5 % decrease respectively. This is a reasonable performance compared to other InGaN photoelectrodes.[61,62] Despite the increased loss of the nanorod structure, this is comparatively less than the planar structure based on total exposed surface area in which a reduction of 13 % would be expected. Evaluation of the hydrogen evolution potential (Figure 4-21 (b)) demonstrates a good agreement with the disparities in photocurrent of the two devices with the nanorod structure performing significantly better than the as-grown.

Hydrogen generation rates of 0.73 ml $h^{-1}cm^{-2}$ and 0.1 ml $h^{-1}cm^{-2}$ were obtained for the nanorod and as-grown devices respectively. The nanorod structure demonstrates a very good faradaic efficiency with the experimental values similar to the theoretical values obtained from the photocurrent. This is attributed to an increase in the surface area of the nanorod device which allows for an increase in reactions. As discussed the nanorod structure can also increase the number of defects at the surface creating hole traps which can help to facilitate the reaction with the electrolyte. Comparatively, the as-

grown device has a relatively poor efficiency. This is likely due to the structure of the device (Figure 4-18) which is inhibiting surface reactions.

4.4.4 Summary

In this work I have demonstrated that InGaN/GaN MQW wafers can be utilised as photoelectrodes for water splitting. Through the simple fabrication of a nanorod array structure the photocurrent of the device has been increased by a factor of 6 over the planar device. The enhancement is attributed in part to the additional surface area obtained from the nanorods increasing the number of surface reactions and light absorption area. Furthermore, the distance required for carrier extraction has been reduced increasing the number of electron-hole pairs contributing to the photocurrent due to reduced recombination rates. Finally, the band bending occurring within the nanorod aids the separation of the electrons and holes. The efficiency of the device has been increased from 0.04 % to 0.26 % and the rate of hydrogen generation increased by a factor of 7 while the relative stability of the device has increased.

4.5 Conclusions

In this chapter the fabrication of a nanorod array structure via the use of a self-organised nickel mask has demonstrated a remarkable enhancement in the performance of GaN and InGaN photoelectrodes. A high level of control over the structure has been demonstrated illustrating the ease in which structural characteristics can be varied leading to optimised performances. The enhancement exhibited by the nanorod structure is the result of a number of factors including surface area, light absorption and carrier diffusion. Furthermore, the use of this technique on a MQW structure illustrates the potential to extend the absorption range of the devices to increase the total available energy available for water splitting. A reasonable level of stability has been demonstrated however with the increased reaction area, anodic corrosion of the nanorod structure is an area for consideration.

Bibliography

[1] J. Zhu and M. Zäch, *Curr. Opin. Colloid Interface Sci.* **14**, 260 (2009).

[2] F.E. Osterloh, *Chem. Soc. Rev.* **42**, 2294 (2013).

[3] R.M. Navarro Yerga, M.C. Alvarez Galván, F. del Valle, J. a Villoria de la Mano, and J.L.G. Fierro, *ChemSusChem* **2**, 471 (2009).

[4] J.P. Best and D.E. Dunstan, *Int. J. Hydrogen Energy* **34**, 7562 (2009).

[5] X. Wang, G. Liu, Z.-G. Chen, F. Li, G.Q. (Max) Lu, and H.-M. Cheng, *Electrochem. Commun.* **11**, 1174 (2009).

[6] X. Wang, G. Liu, G.Q. Lu, and H.-M. Cheng, *Int. J. Hydrogen Energy* **35**, 8199 (2010).

[7] G.K. Mor, K. Shankar, M. Paulose, O.K. Varghese, and C. a Grimes, *Nano Lett.* **6**, 215 (2006).

[8] J.H. Park, S. Kim, and A.J. Bard, *Nano Lett.* **6**, 24 (2006).

[9] Z. Liu, B. Pesic, K.S. Raja, R.R. Rangaraju, and M. Misra, *Int. J. Hydrogen Energy* **34**, 3250 (2009).

[10] K. Sun, Y. Jing, C. Li, X. Zhang, R. Aguinaldo, A. Kargar, K. Madsen, K. Banu, Y. Zhou, Y. Bando, Z. Liu, and D. Wang, *Nanoscale* **4**, 1515 (2012).

[11] S. Li and A. Waag, *J. Appl. Phys.* **111**, 071101 (2012).

[12] Y.B. Tang, Z.H. Chen, H.S. Song, C.S. Lee, H.T. Cong, H.M. Cheng, W.J. Zhang, I. Bello, and S.T. Lee, *Nano Lett.* **8**, 4191 (2008).

[13] Y.-B. Tang, X.-H. Bo, C.-S. Lee, H.-T. Cong, H.-M. Cheng, Z.-H. Chen, W.-J. Zhang, I. Bello, and S.-T. Lee, *Adv. Funct. Mater.* **18**, 3515 (2008).

[14] Q. Li and G.T. Wang, *Appl. Phys. Lett.* **93**, 043119 (2008).

[15] F. Shi, H. Li, and C. Xue, *J. Mater. Sci. Mater. Electron.* **21**, 1249 (2010).

[16] F. Qian, Y. Li, S. Gradec, and C.M. Lieber, 20 (2004).

[17] R. Calarco, R.J. Meijers, R.K. Debnath, T. Stoica, E. Sutter, and H. Lüth, *Nano Lett.* **7**, 2248 (2007).

[18] K.A. Bertness, A. Roshko, L.M. Mansfield, T.E. Harvey, and N.A. Sanford, *J. Cryst. Growth* **300**, 94 (2007).

[19] E. Calleja, J. Ristić, S. Fernández-Garrido, L. Cerutti, M.A. Sánchez-García, J. Grandal, A. Trampert, U. Jahn, G. Sánchez, A. Griol, and B. Sánchez, *Phys. Stat. Sol (B)* **244**, 2816 (2007).

[20] S. Li, S. Fündling, Ü. Sökmen, R. Neumann, S. Merzsch, P. Hinze, T. Weimann, U. Jahn, A. Trampert, H. Riechert, E. Peiner, H.-H. Wehmann, and A. Waag, *Phys. Stat. Sol (C)* **7**, 2224 (2010).

[21] C.H. Chiu, T.C. Lu, H.W. Huang, C.F. Lai, C.C. Kao, J.T. Chu, C.C. Yu, H.C. Kuo, S.C. Wang, C.F. Lin, and T.H. Hsueh, *Nanotechnology* **18**, 445201 (2007).

[22] Y. Wu, C. Chiu, C. Chang, S. Member, and A. In, *IEEE J. Sel. Top. Quantum Electron.* **15**, 1226 (2009).

[23] T. Wang, GB2487917 (2011).

[24] Q. Wang, J. Bai, Y.P. Gong, and T. Wang, *J. Phys. D. Appl. Phys.* **44**, 395102 (2011).

[25] H. Jung, Y. Hong, Y. Li, J. Cho, Y. Kim, and G. Yi, *ACS Nano* **2**, 637 (2008).

[26] K. Fujii, T. Kato, K. Sato, I. Im, J. Chang, and T. Yao, *Phys. Stat. Sol (C)* **7**, 2218 (2010).

[27] J. Bai, T. Wang, P. Comming, P.J. Parbrook, J.P.R. David, and a. G. Cullis, *J. Appl. Phys.* **99**, 023513 (2006).

[28] J. Bai, T. Wang, P.J. Parbrook, K.B. Lee, and a. G. Cullis, *J. Cryst. Growth* **282**, 290 (2005).

[29] J. Bai, T. Wang, P.J. Parbrook, I.M. Ross, and a. G. Cullis, *J. Cryst. Growth* **289**, 63 (2006).

[30] B. Monemar, *Phys. Rev. B* **10**, 676 (1974).

[31] D. Miller, Gallium Nitride Epitaxy by a Novel Hybrid VPE Technique, Stanford University, 2011.

[32] W. Grieshaber, E.F. Schubert, I.D. Goepfert, R.F. Karlicek, M.J. Schurman, and C. Tran, *J. Appl. Phys.* **80**, 4615 (1996).

[33] E.F. Schubert, I.D. Goepfert, W. Grieshaber, and J.M. Redwing, *Appl. Phys. Lett.* **71**, 921 (1997).

[34] U. Kaufmann, M. Kunzer, H. Obloh, M. Maier, C. Manz, a. Ramakrishnan, and B. Santic, *Phys. Rev. B* **59**, 5561 (1999).

[35] T. Ogino and M. Aoki, *Jpn. J. Appl. Phys.* **19**, 2395 (1980).

[36] M. Ono, K. Fujii, T. Ito, Y. Iwaki, A. Hirako, T. Yao, and K. Ohkawa, *J. Chem. Phys.* **126**, 054708 (2007).

[37] K. Fujii and K. Ohkawa, *J. Electrochem. Soc.* **153**, A468 (2006).

[38] K. Fujii and K. Ohkawa, *Jpn. J. Appl. Phys.* **44**, L909 LP (2005).

[39] K. Fujii, T. Karasawa, and K. Ohkawa, *Jpn. J. Appl. Phys.* **44**, L543 (2005).

[40] J. Bai, Q. Wang, and T. Wang, *Phys. Stat. Sol (A)* **209**, 477 (2012).

[41] A. Baldan, **7**, 2171 (2002).

[42] J.D. Carey, L.L. Ong, and S.R.P. Silva, *Nanotechnology* **14**, 1223 (2003).

[43] F. Demangeot, J. Gleize, J. Frandon, M. a. Renucci, M. Kuball, D. Peyrade, L. Mani*n*-Ferlazzo, Y. Chen, and N. Grandjean, *J. Appl. Phys.* **91**, 2866 (2002).

[44] Y.D. Wang, S.J. Chua, S. Tripathy, M.S. Sander, P. Chen, and C.G. Fonstad, *Appl. Phys. Lett.* **86**, 071917 (2005).

[45] D.G. Zhao, S.J. Xu, M.H. Xie, S.Y. Tong, and H. Yang, *Appl. Phys. Lett.* **83**, 677 (2003).

[46] C.P. Kuo, S.K. Vong, R.M. Cohen, and G.B. Stringfellow, *J. Appl. Phys.* **57**, 5428 (1985).

[47] W. Shan, R. Hauenstein, A. Fischer, J. Song, W. Perry, M. Bremser, R. Davis, and B. Goldenberg, *Phys. Rev. B. Condens. Matter* **54**, 13460 (1996).

[48] I. Waki, D. Cohen, R. Lal, U. Mishra, S.P. DenBaars, and S. Nakamura, *Appl. Phys. Lett.* **91**, 093519 (2007).

[49] M. Godlewski, E. Łusakowska, E.. Goldys, M.. Phillips, T. Böttcher, S. Figge, D. Hommel, P. Prystawko, M. Leszczynski, I. Grzegory, and S. Porowski, *Appl. Surf. Sci.* **223**, 294 (2004).

[50] P.M. Bridger, E.C. Piquette, T.C. Mcgill, and Z.Z. Bandic, *Solid State Commun.* **44**, 221 (2000).

[51] X. Zhang, P. Kung, D. Walker, J. Piotrowski, a. Rogalski, a. Saxler, and M. Razeghi, *Appl. Phys. Lett.* **67**, 2028 (1995).

[52] J.D. Beach, InxGa1-xN For Potoelectrochemical Water Splitting, Colorado School of Mines, 2001.

[53] C. Mauder, Ö. Tuna, B. Gutrath, V. Balmes, H. Behmenburg, M. V. Rzheutskii, E. V. Lutsenko, G.P. Yablonskii, M. Noyong, U. Simon, M. Heuken, H. Kalisch, and a. Vescan, *Phys. Stat. Sol (C)* **9**, 964 (2012).

[54] J. Li, J.Y. Lin, and H.X. Jiang, *Appl. Phys. Lett.* **93**, 162107 (2008).

[55] C. Pendyala, J.B. Jasinski, J.H. Kim, V.K. Vendra, S. Lisenkov, M. Menon, and M.K. Sunkara, *Nanoscale* **4**, 6269 (2012).

[56] L. Wang, W. Zhao, Z.-B. Hao, and Y. Luo, *Chinese Phys. Lett.* **28**, 057301 (2011).

[57] B. AlOtaibi, H.P.T. Nguyen, S. Zhao, M.G. Kibria, S. Fan, and Z. Mi, *Nano Lett.* **13**, 4356 (2013).

[58] K. Fujii, S. Nakamura, S. Yokojima, T. Goto, T. Yao, M. Sugiyama, and Y. Nakano, *J. Phys. Chem. C* **115**, 25165 (2011).

[59] L. a. Vilbois, a. Cheknane, a. Bensaoula, C. Boney, and T. Benouaz, *Energy Procedia* **18**, 795 (2012).

[60] R.-S. Chen, H.-Y. Chen, C.-Y. Lu, K.-H. Chen, C.-P. Chen, L.-C. Chen, and Y.-J. Yang, *Appl. Phys. Lett.* **91**, 223106 (2007).

[61] M. Li, W. Luo, B. Liu, X. Zhao, Z. Li, D. Chen, T. Yu, Z. Xie, R. Zhang, and Z. Zou, *Appl. Phys. Lett.* **99**, 112108 (2011).

[62] K. Aryal, B.N. Pantha, J. Li, J.Y. Lin, and H.X. Jiang, *Appl. Phys. Lett.* **96**, 052110 (2010).

Chapter 5

NiO Nanoparticles on GaN Nanorods for Reduced Etching

Complementary materials have been added to various material systems for solar hydrogen production with the aim being to either increase photocurrent or hydrogen evolution rate. In this chapter, by means of depositing transparent nickel oxide nano-particles on the nanorod array structure, a significant reduction in photo-electrochemical etching effects has been achieved on an InGaN/GaN nanorod array structure used as a photoelectrode in a NaOH electrolyte. In the meantime, the addition of the nickel oxide nano-particles has also led to an increase in photocurrent, thus enhancing the energy conversion efficiency. The mechanisms for the enhanced photocurrent and minimising the photochemical etching effect of GaN in NaOH have been systematically investigated.

5.1 Cocatalysts in Water Splitting

In order to improve the efficiency of photocatalysis the addition of cocatalysts has become a relatively common practice.[1] Due to noble metals (Pt, Pd) demonstrating a high level of activity for hydrogen reduction, the inclusion on the surface of other photocatalysts (TiO_2, Fe_2O_3) can increase the overall hydrogen generation rate. Cocatalysts provide reaction sites and decrease the activation energy for gas generation.[2] Traditionally noble metals

(Pt, Rh) are utilised due to their high reaction rates in promoting the H_2 evolution reaction.[3] These cocatalysts are typically added to metal oxide photocatalysts as a result of their insufficient conduction band position. Noble metals also catalyse the reverse reaction, forming water from the generated hydrogen and oxygen. As a result of this there is a limit as to their potential in water splitting. In order to prevent this competitive reaction occurring a core/shell structure is commonly utilised (Figure 5-1). The design of the structure allows the promotion of the hydrogen reaction at the noble/metal core with an effective transfer of electrons. The shell prevents the penetration of oxygen to the core, effectively minimising the formation of water. As with the standard formation of hydrogen, the reaction proceeds via a number of steps. Initially hydrogen ions permeate the shell and adsorb onto the core. A transfer of electrons between the photoelectrode material and core metal occurs prior to the reduction of the hydrogen ions at the metal core surface. Due to the close proximity of multiple individual hydrogen ions on the core surface, adhered molecular hydrogen is formed. Finally desorption occurs releasing gaseous molecular hydrogen as demonstrated in Figure 5-1.

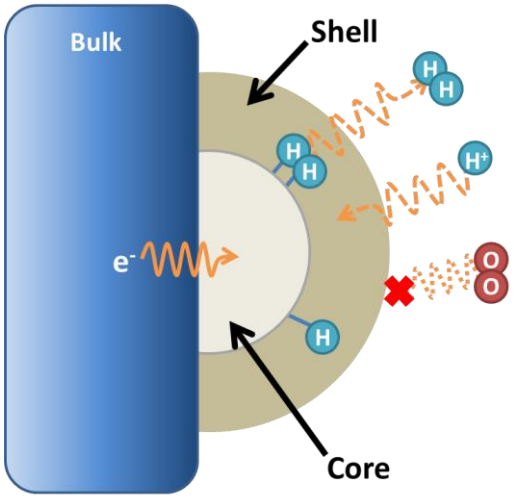

Figure 5-1 – Illustration of hydrogen and oxygen evolution on a core/shell structure on a bulk photoelectrode material. Adapted from Maeda, 2010.[2]

Detailed studies have been confirmed that without the core/shell structure the evolution of gases is prevented due to the effective backward reaction caused by the noble metal cocatalysts.[4] The cocatalyst used is

dependent on the bulk photocatalyst with Pt showing a good performance in sulphide based devices.[5] For oxide photocatalysis, common materials include Rh or NiO_x materials. A recent review by Kuda illustrates the various cocatalysts used on different photocatalysts.[3] The NiO_x cocatalyst is formed from a nickel core with a nickel oxide shell and is utilised for the promotion of the hydrogen reaction as illustrated in Figure 5-1.[6,7]

Another function of cocatalysts is to engineer band structures in order to enhance carrier transfer (Figure 5-2). Wide band gap semiconductors, for example GaN, have the correct band structures to straddle the two redox levels of water. Loading the material with a complementary cocatalyst can enhance the electron transfer from the wide band gap semiconductor conduction band into the conduction band of the cocatalyst promoting the hydrogen reaction at this site. This has been demonstrated in various tanatalate systems.[3,8]

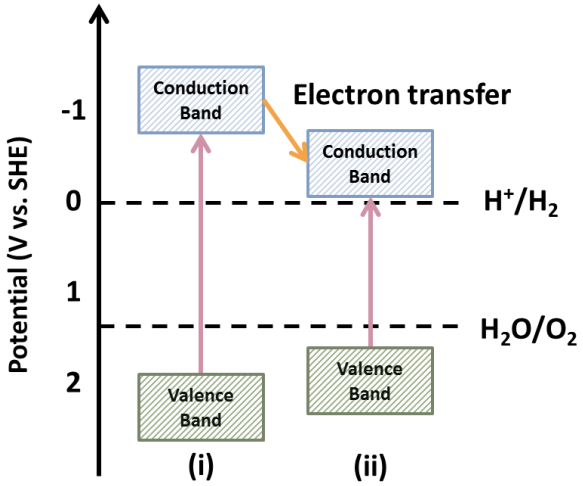

Figure 5-2 - Band structures of wide band gap semiconductor (i) and cocatalyst (ii)

Control over the deposition procedure and method is required in order to achieve the desired enhancement. The approaches to the deposition of cocatalysts include photodeposition (PD) and impregnation techniques. Photodeposition involves the use of selective chemical solutions and an irradiation source. As a result of the use of an irradiation source there is some selectivity regarding the position of the deposited cocatalysts.[9,10] Impregnation involves the chemical deposition of a solution onto the

photocatalyst followed by calcination of the cocatalyst. As a result the particles are more randomly dispersed over the surface over the main photoelectrode. Changing the loading of the catalyst can alter the overall effectiveness of the device.[11] It is therefore important to obtain proper deposition techniques in order to effectively enhance device performance.

5.1.1 Cocatalysts on GaN

Despite the widely accepted requirement of cocatalysts for effective water splitting the research into materials complementary to GaN is limited. Wang *et al.* photodeposited a ruthenium and chromium oxide core/shell structure onto MBE grown GaN nanowires.[12] The core/shell structure aided the overall photocatalytic reaction on the GaN nanowires in pure water increasing the activity of the device. Stable evolution of stoichiometric amounts of hydrogen and oxygen for 18 hours has been achieved. In addition to Rh/Cr_2O_3 structure, the deposition of NiO on GaN has increased the stability of the device.[13] Ohkawa *et.al* proposed that NiO could lead to the oxidation reaction occurring at the interface between NiO and electrolyte instead of the GaN/electrolyte interface. This resulted in a stable photocurrent for 500 hours indicating the significant reduction in the corrosion of GaN in hydroxide solutions. However, further study into the mechanism is necessary. In this chapter, a significant improvement in the performance of GaN based devices is observed with the utilisation of NiO nanoparticles deposited on GaN in terms of efficiency and minimising corrosion. After our report on the utilisation of NiO nanoparticles on GaN nanostructures, another group has also employed NiO nanoparticles on planar GaN and achieved excellent results, further supporting the current findings of this thesis.[14]

5.2 GaN/InGaN Devices

In order to effectively assess the optimum technique for the fabrication of NiO nanoparticles on GaN based devices initial tests were conducted on planar and nanorod *n*-type GaN. As illustrated in Figure 2-16, there are many semiconductors that have the proper band structure, which

can straddle the two redox levels for water splitting. Ideally for a multi semiconductor device the second semiconductor would be of a smaller band gap to increase the amount of visible light available. If this is the case, then the conduction and valence band positions of the semiconductors have to be in a suitable position to allow effective charge transfer. As discussed, cocatalysts can aid the hydrogen evolution reaction promoting electron transfer to the cocatalyst. Alternatively the cocatalyst can aid the separation of the photogenerated carriers. The use of NiO promotes the latter function due to the positions of the conduction and valence bands compared to GaN (Figure 5-3). As the band gap of NiO is larger than that of GaN, it doesn't provide any sensitization however is transparent to the wavelengths required to promote carriers in GaN. This allows both semiconductors to become active upon irradiation.

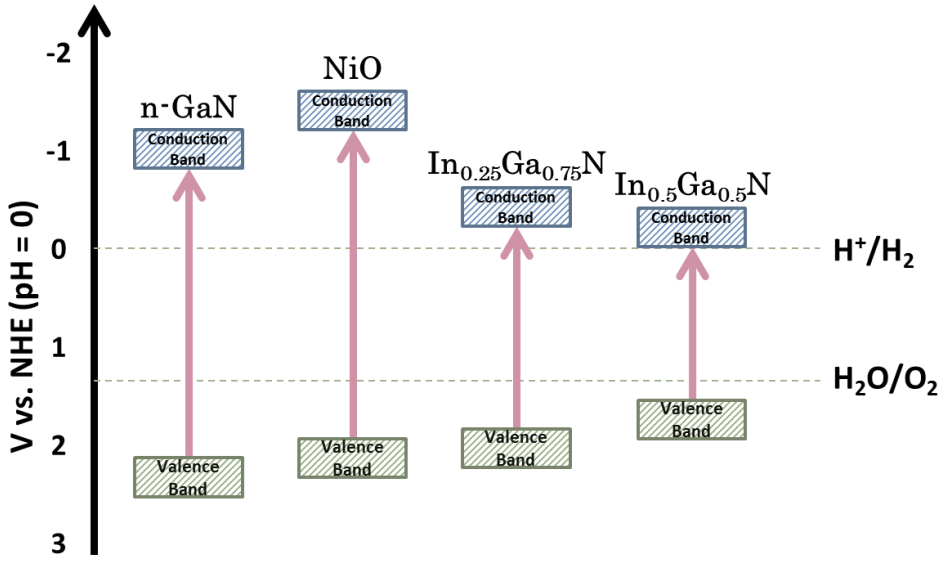

Figure 5-3 – Relative conduction and valence band positions of NiO and GaN based semiconductors

5.2.1 Fabrication

A typical *n*-type GaN wafer described in Chapter 4 and three InGaN/GaN MQW wafers of different indium contents were utilised. For the *n*-type GaN a high temperature (1200 °C) AlN buffer layer is grown on a (0001) sapphire substrate under low pressure conditions after thermal substrate cleaning in flowing hydrogen. An un-doped GaN layer is then grown

upon the flat AlN layer. Following this an *n*-type GaN layer of ~1.5 µm is grown via the introduction of di-silane to the MOCVD reactor. GaN nanorods were also fabricated via the same method identified in Chapter 4 in which a two stage etch mask is utilised to fabricate controlled nanorods via inductively coupled plasma etching. For the InGaN/GaN MQW wafers the structure is similar to that used in the initial nanorod study described in Chapter 4. Essentially a 1.4 µm undoped GaN buffer, followed by 2.8 µm silicon doped GaN (*n*-GaN) is grown on a c-plane sapphire substrate. Following this a thin $In_{0.05}Ga_{0.95}N$ strain release layer and 10 periods of InGaN/GaN (2.5 nm/13.4 nm) multiple quantum wells (MQWs) are grown. A typical AlGaN layer of ~20nm was used as an electron blocking layer (EBL) before being finally capped with 200nm of magnesium doped GaN (*p*-GaN). Nanorods were fabricated by the method previously described in Chapter 4.

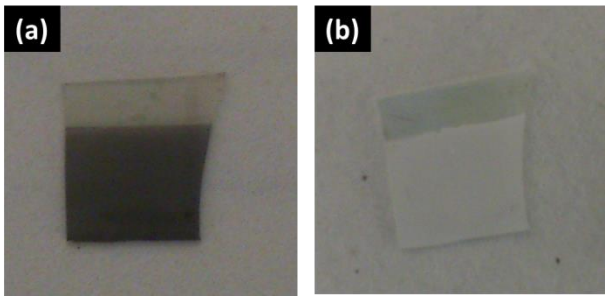

Figure 5-4 – Examples of NiO fabrication (a) after nickel deposition (b) after annealing

The preparation of the NiO nano-particle films on the samples is then performed. Initially the contact area of the sample is masked off via standard photolithographic techniques. Following this a thin layer of nickel (2-8 nm) is deposited onto the surface of the sample via a standard thermal evaporation approach. The samples then undergo an annealing process at 850 °C for 1 minute in a nitrogen atmosphere in order to form self-organised Ni nanoparticles. This technique is similar to that used in the formation of the nickel nanomasks developed by our group for the nanorod fabrication. The major difference between them is the thickness of nickel film, which determines the final diameter of the nanoparticles as discussed in Chapter 4. The final preparation of the cocatalyst proceeds via a secondary annealing

process in an oxygen and nitrogen atmosphere (20:80 ratio) at a temperature of 520 °C for approximately 25 minutes until the film becomes completely transparent as shown in Figure 5-4, indicating the formation of NiO nanoparticles.

5.2.2 Characterisation

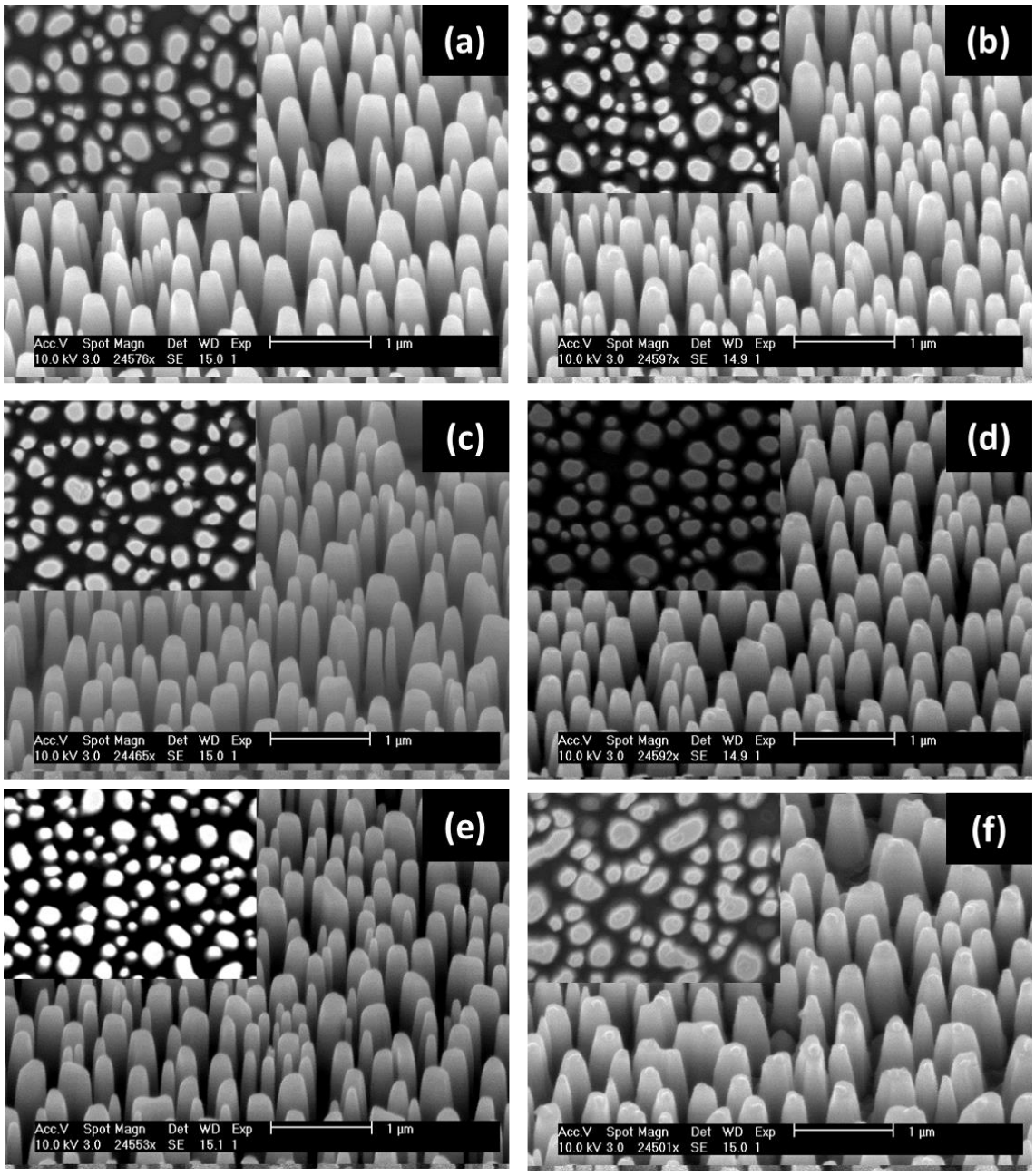

Figure 5-5 – SEM images of InGaN/GaN MQW with and without NiO. Insets display plan view of nanorods. (a) from wafer A (b) from wafer A w/NiO (c) from wafer B (d) from wafer B w/NiO (e) from wafer C (f) from wafer C w/NiO

Photoluminescence and scanning electron microscopy (SEM) measurements were conducted on the GaN and InGaN/GaN samples. SEM

images of the samples were taken after initial fabrication of the nanorods with and without the nickel oxide as shown in Figure 5-5. It is clear that the fabricated nanorods have similar structures and uniformities across the three InGaN/GaN wafers utilised. Plan view images shown in the inset of Figure 5-5 illustrate the adhesion of the nickel oxide nanoparticles to the tops of the nanorods. As a result of the fabrication technique, the majority of the as deposited nickel is distributed on the tops of the nanorods and the gaps between nanorods rather than the side walls. However, we believe that there is still a high chance for the partial coverage of nickel on the sidewall of nanorods. The nanorods were formed with an 8 nm nickel mask which has resulted in a density of ~10^8 cm^{-2} and a diameter of ~240 nm. For the NiO particles, unlike the Ni nanoislands used as the etch mask as described in Chapter 4, the cocatalyst nanoparticles form after nanorod fabrication can only coalesce from a smaller area. As a result, the NiO cocatalyst nanoparticles are approximately 50 nm in diameter, but vary based on the nanorod in which it formed.

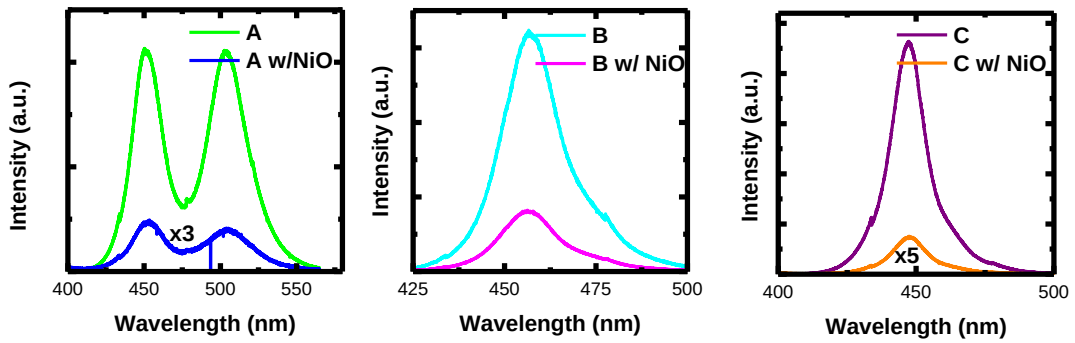

Figure 5-6 – Room temperature photoluminescence of InGaN/GaN MQW wafers with and without NiO

Room temperature PL using a 375 nm diode laser of the fabricated nanorods with and without the NiO indicates a clear change as a result of formation (Figure 5-6). Due to differences in the indium content of the quantum wells the peak emission is different across the three wafers. Wafer A demonstrates two peaks at 449 and 503 nm, wafer B has emission at 456 nm and wafer C at 447 nm. The different indium contents will result in slightly different conduction and valence bands which could ultimately

change the effect the NiO has on the photocurrent. In all cases, the photoluminescence of the wafers with the NiO nanoparticles has been severely reduced. With a band gap of 3.6 eV, the nanoparticles are transparent to the 375 nm laser. As the reference devices and devices with the NiO cocatalyst underwent identical annealing conditions this suggests the reduction in PL is attributed to a change in the recombination kinetics of the system. It is possible that upon carrier generation, the addition of the NiO promotes carrier separation and prevents recombination within the quantum wells, quenching the emission.

5.2.3 Step Photocurrent Measurements

Standard photocurrent measurements were conducted at 0.2 V intervals from -1 to 2 V in a 1 M NaOH solution. As previously discussed, despite the wide scale use of HCl as an electrolyte, the reaction can result in the formation of both chlorine and oxygen. As an alternative, NaOH can be utilised, however previous work has demonstrated the poor stability of planar GaN in NaOH through the discussed photocorrosion mechanism.[15] Due to the issue experienced with as-grown GaN, the effect on InGaN/GaN nanorods is likely to be more pronounced. Figure 5-7 demonstrates the photocurrent measurements of the three InGaN/GaN nanostructures coated with and without NiO under one sun illumination. As a reference, planar *n*-type GaN has also been measured. The formation of a planar film on the surface had no significant effect on photocurrent. Despite the larger band gap of the NiO allowing penetration of light into the GaN there is an increase in the required diffusion to the surface resulting in the potential for increased recombination within the bulk GaN film with the NiO coating. However, the use of nanoparticles enhances photocurrent as it still allows for the interaction of the GaN with the electrolyte. There is also a notable change in the turn on voltage of the NiO nanoparticle coated GaN device, at -0.9 V compared to -0.6 V observed. This is due to the change in device structure and band alignments due to the interface between the NiO and the GaN.

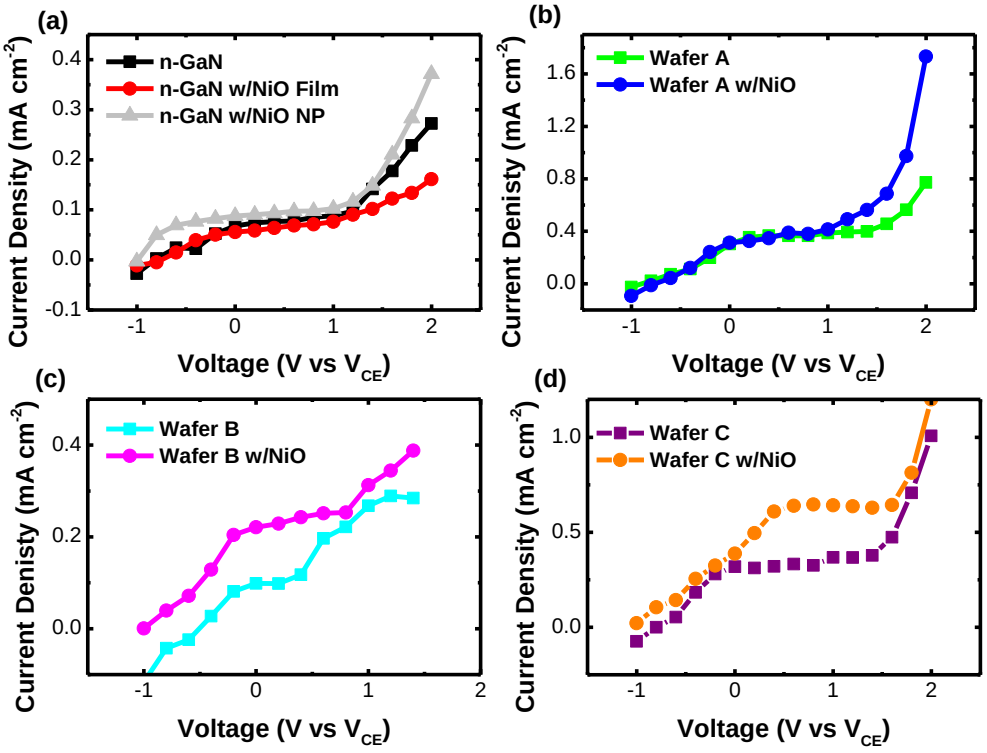

Figure 5-7 – Photocurrent measurements at 100 mW cm-2 irradiation in a 1 M NaOH electrolyte at biases from -1 to 2 V (a) planar *n*-type GaN (b) InGaN/GaN nano structure from wafer A (c) InGaN/GaN nanostructure from wafer B (d) InGaN/GaN nanostructure from wafer C

From Figure 5-7 there are clear differences between the performances of the three InGaN/GaN wafers. Unlike the *n*-GaN, devices from wafer A, which exhibited two emission peaks at both 450 nm and 503 nm (typical for high indium content InGaN as a result of indium segregation due to large miscibility between InN and GaN, which is more severe for high indium content), don't demonstrate significant change in the photocurrent compared to the device without NiO. However, the samples with low indium contents from wafer B and C, with a single 450 nm emission peak, exhibit an improved photocurrent response. As illustrated previously (Figure 5-3), the band positions of NiO are shifted slightly compared to those of GaN. It is as a result of the differences in conduction and valence bands which results in the increased photocurrent. The discontinuity between the conduction bands of NiO and GaN result in the migration of the photogenerated electrons away from the surface and prevent any transfer of electrons to the NiO (Figure 5-8). In addition to this, the variation of the valence band promotes the

migration of holes into the NiO. As a result of this there is an increase in the spatial separation of charges in the device which leads to a reduction in recombination of the carriers. With a decreased recombination there is an increase in carriers participating in the generation of photocurrent.

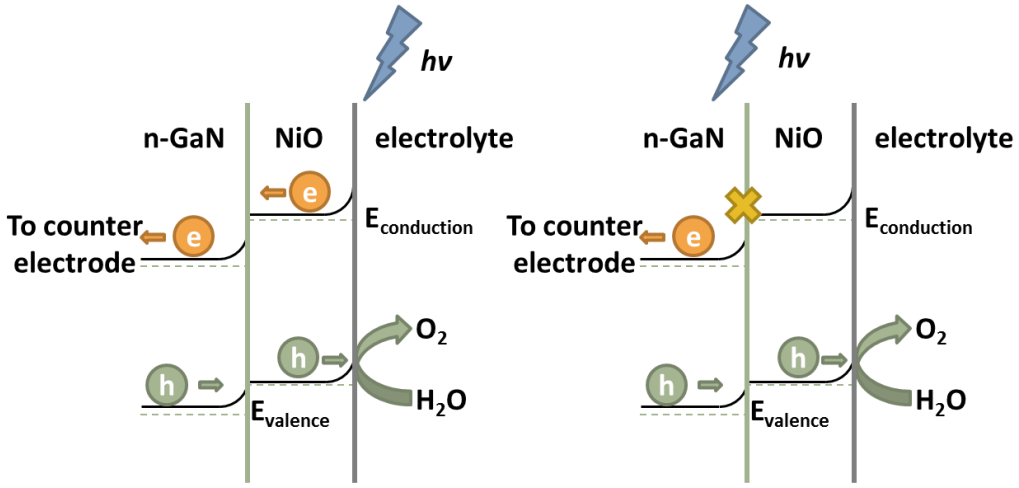

Figure 5-8 – Schematic of the band diagrams and illumination mechanism occurring in GaN/NiO structure when NiO nanoarticles (left) or GaN (right) is illuminated

The difference in the photocurrent of the InGaN/GaN MQW wafers is attributed to the differences in indium content of the quantum wells. This variation will lead to changes in the band structure and electron-hole recombination properties within each system. Alongside this, there is variation in the quality of the material due to defects and strain caused by higher indium contents. Generally, high indium InGaN needs to be grown at fairly low temperatures in order to enhance indium incorporation into GaN. This leads to a severe degradation in crystal quality, such as for wafer A, in which no distinguished enhancement is observed. As the indium content decreases, as in the devices from wafers B and C, an enhancement is observed with the NiO addition. Furthermore, due to the nature of the NiO deposition process, the variation in nanoparticle size may also contribute to the overall effectiveness.

5.2.4 Steady State Measurements

Ideally devices will operate for a significant period of time, preferably in excess of 20 years.[16] Steady state tests have been conducted on the six InGaN/GaN based nanorod devices, measured at a voltage of 0.8 under 100

$mWcm^{-2}$ of AM 1.5 filtered illumination for a period of 180 minutes. Periodic intervals (15, 45, 105 and 180 minutes) were taken during the test to assess the extent of corrosion on the device via SEM analysis. Figure 5-9 shows the photocurrent as a function of testing time for the device fabricated from wafer B. In order to clearly demonstrate the enhancement in device performance in terms of photocurrent, a performance index has been introduced, defined as the ratio of photocurrent from the device with the NiO nanoparticles to that from the device without the NiO nanoparticles. The enhanced performance has been observed throughout the length of the test. In detail, the enhancement factor of the photocurrent, namely, the performance index increases from 136 % to 152 % with an increase in testing time, as shown in Figure 5-9.

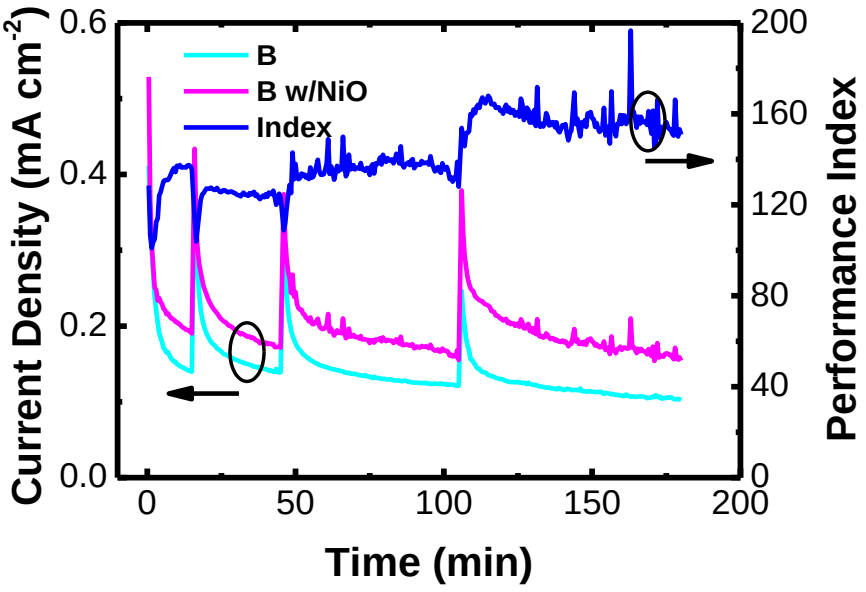

Figure 5-9 – Steady state photocurrent measurements of the device fabricated from wafer B with and without NiO. Performance enhancement over the device without NiO nanoparticles as a reference sample over time also illustrated.

Careful examination of Figure 5-9 indicates that a reduction in photocurrent with increasing time has been observed on both the samples with and without the NiO which suggests that anodic etching is still occurring. However, the reduction of the photocurrent from the device coated with NiO nanoparticles is less severe than that of the device without NiO nanoparticles. For example, a decrease of 30 % and 15 % in photocurrent has been observed

from the start of the test for the reference device without NiO nanoparticles and the device with NiO nanoparticles respectively. The significant decrease in photocurrent reduction is attributed to the separation of the photogenerated holes migrating to the NiO. As a result, there are a decreased number of holes reacting at the GaN surface reducing the potential for photocorrosion to occur.

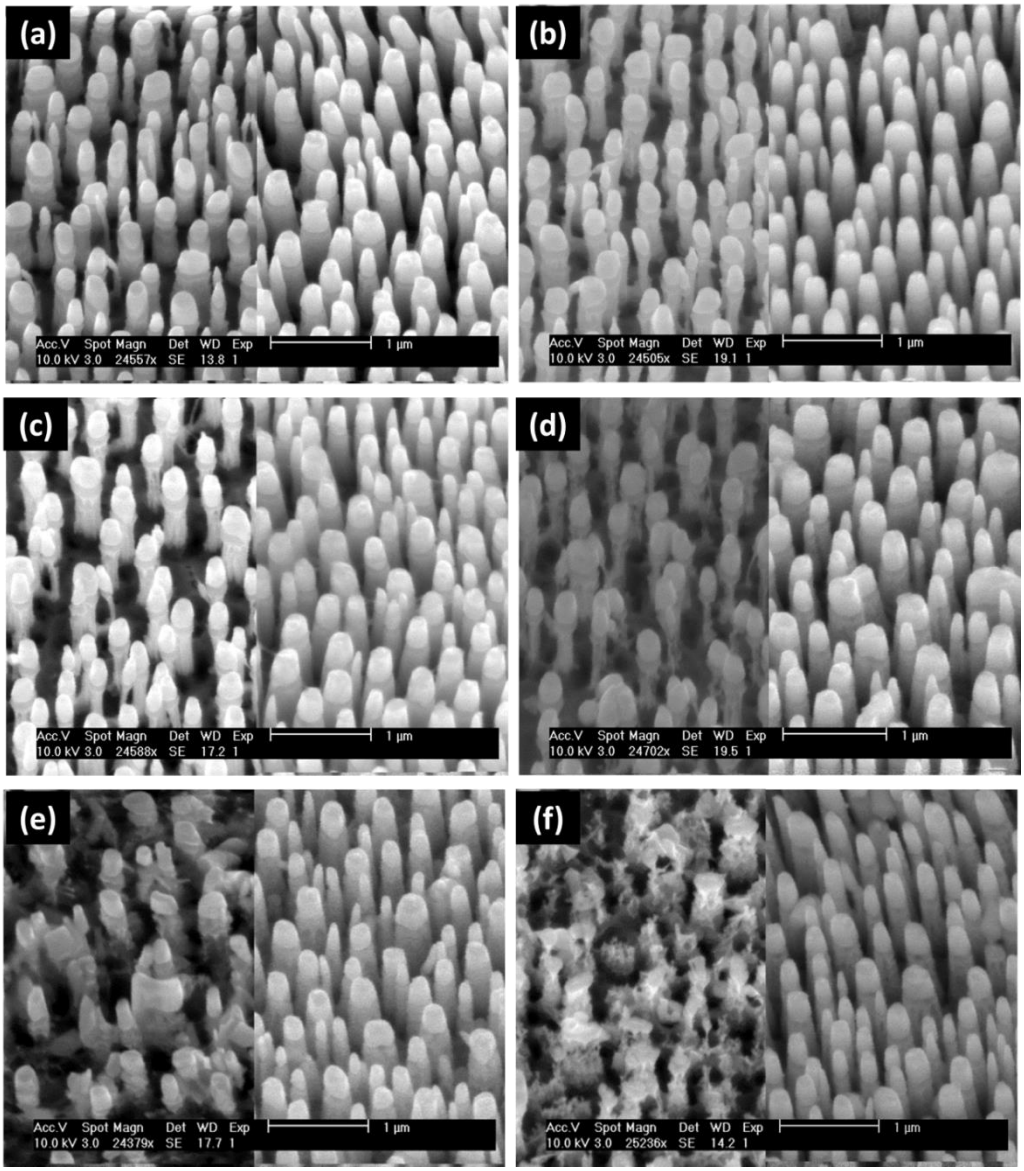

Figure 5-10 – SEM images of nanorods over time after photocurrent measurements. Left Hand Side: reference nanorods, Right Hand Side: nanorods with NiO (a)-(d) devices from wafer B at 15 minutes, 50 minutes, 105 minutes and 180 minutes (e) devices from wafer A at 180 minutes (f) devices from Wafer C at 180 minutes

Scanning electron microscopy images have been taken on the three sets of samples (with and without NiO nanoparticles, fabricated from wafer A,

B, and C, respectively) throughout the three hour test period to study the corrosion issue, illustrated in Figure 5-10. As demonstrated, all three devices with the NiO nanoparticles show an improved resistance to corrosion compared to their individual references. Severe corrosion has been observed by the NaOH solution on all the devices fabricated without NiO cocatalyst, independent of indium content. It is very interesting to highlight the stability of the upper *p*-type GaN on the nanorods. As previously discussed the migration of electrons in *p*-type GaN to the surface prevents oxidation due to the requirement of holes,[17] leading to a reduction or elimination of corrosion on *p*-GaN.[18]

Below the *p*-type layers are InGaN/GaN MQWs and *n*-GaN. Figure 5-10(b) shows a clear etching of the parts below the *p*-type layers after 50 minutes testing, in particular, the InGaN/GaN MQWs, which is just below the *p*-type layers. This is potentially due to increased reactions occurring in the indium rich reasons, agreeing with the previous results based on PL measurements on bulk InGaN films.[19] After the total test time of 180 minutes, the reference devices without NiO show severe corrosion, leading to significantly thinned nanorods. The mechanism of the photochemical etching of GaN in NaOH under UV illumination has been discussed in Chapter 2, which can be described by the equations below in more detail,

$$2GaN + 6h^+ \rightarrow 2Ga^{3+} + N_2 \uparrow \quad (1)$$

$$2Ga^{3+} + 6OH^- \rightarrow 2Ga_2O_3 + 6H^+ \quad (2)$$

$$Ga_2O_3 + 6OH^- \rightarrow 2GaO_3{}^{3-} + 3H_2O \quad (3)$$

Incident photons, with energy above the band gap of GaN generate electrons and holes. The migration of the holes to the surface of the GaN can result in the formation of Ga ions (Equation 1). The resulting ions can then react with the hydroxide ions in the solution forming an oxide layer on the surface of nitride and the generation of hydrogen ions in solution (Equation 2). The formed oxide is then soluble in the presence of hydroxide ions resulting in dissolution (Equation 3). This is the mechanism for the

photochemical etching of GaN in NaOH solution. Following this, a fresh GaN layer is visible and the process can repeat resulting in the potential for continual corrosion of GaN.

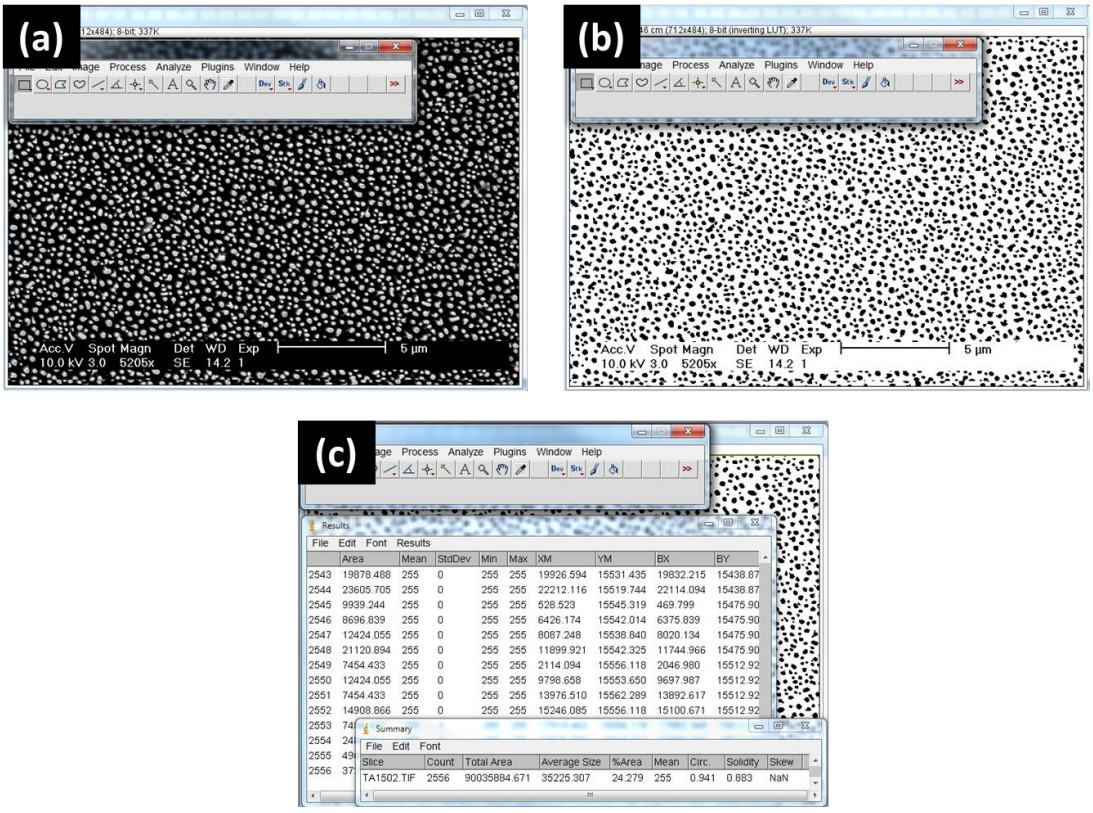

Figure 5-11 – Analysis process when using ImageJ (a) Initial loading of the image (b) binary conversion of the image (c) detailed analysis of each particle

The combination of the plan-view SEM images and open source image analysis software provides a greater insight into the corrosion observed during the etching of the nanorods. The analysis software produced by the US National Institute of Health (ImageJ) was utilised to assess the coverage area, distribution and size of the nanorods. The software has been used in literature for particle analysis across a range of topics.[20–22] A selection of high contrast plan-view SEM images with 5000x magnification were used to gather the data. The process involves loading each image into the software and setting the pixel scale based on the scale of the SEM images (Figure 5-11 (a)). This allows for the accurate calculations of black areas and sizes provided by the SEM images, which are the nanorods. Following this the images are converted into digital signals for further processing (Figure 5-11 (b)). A high contrast image makes this easier however settings on the software allow

control over the contrast in order to accurately calculate the sizes. Half particles are removed prior to processing to increase the accuracy of the results for which analysis of each particle is presented in a tabulated format as illustrated in Figure 5-11 (c).

Comparison of the overall nanorod coverages from the SEM images obtained with different testing time provides accurate information of the corrosion as a result of photochemical etching. Figure 5-12 illustrates the overall nanorod coverages as a function of testing time for the three sets of devices. A clear downward trend in nanorod coverage is observable for the samples without NiO, reducing by a value of 15 %, 15.7 % and 15.6 % for the devices fabricated from wafers A, B and C respectively. In a remarkable contrast, the counterparts coated with NiO cocatalyst demonstrate a decrease of 0 %, 4.9 % and 3.1 % in nanorod coverage. Based on the SEM images, the tops of the nanorods remain relatively intact throughout the etching suggesting that the 15 % decrease in coverage observed for the devices without NiO is a conservative estimate for the degradation suggesting an even greater performance of the devices with NiO cocatalysts.

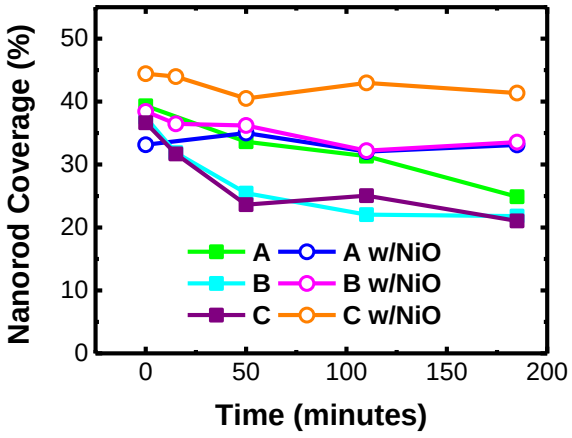

Figure 5-12 – Nanorod coverage of all six devices with and without NiO based on ImageJ analysis of top-down SEMS, representative errors are illustrated for devices from wafer B

Further to the analysis of the nanorod coverage, an investigation into the change in nanorod radius has also been carried out. The radius was calculated assuming circular nanorods by the equation πr^2. Thousands of

data points were analysed for each step providing good reliability in regards to results. Based on the analysis of each image a histogram of the data was collected to group the data into proper categories, based on distribution in terms of nanorod sizes. These were, <20 nm, 20>x<50 nm, 50>x<70 nm, 70>x<90 nm, 90>x<110 nm, 110>x<130 nm, 130>x<150 nm, 150>x<170 nm, 170>x<200 nm and 200>x<250 nm. Figure 5-13 illustrates the difference between the devices with and without coated NiO nanoparticles, fabricated from wafer B as an example. The initial maximum abundance peak is exhibited at 130/150 nm for both wafers indicating a reasonable level of uniformity in the samples prior to photoelectrochemical reactions. Figure 5-13 indicates that the distribution of the nanorod radii remains largely unchanged for the sample with NiO nanoparticles, while a clear shift to a smaller size in terms of maximum radius has been demonstrated for the reference device without NiO. In detail, the maximum radius decreases from 140 nm to 110 nm after the 3 hour photoelectrochemical tests.

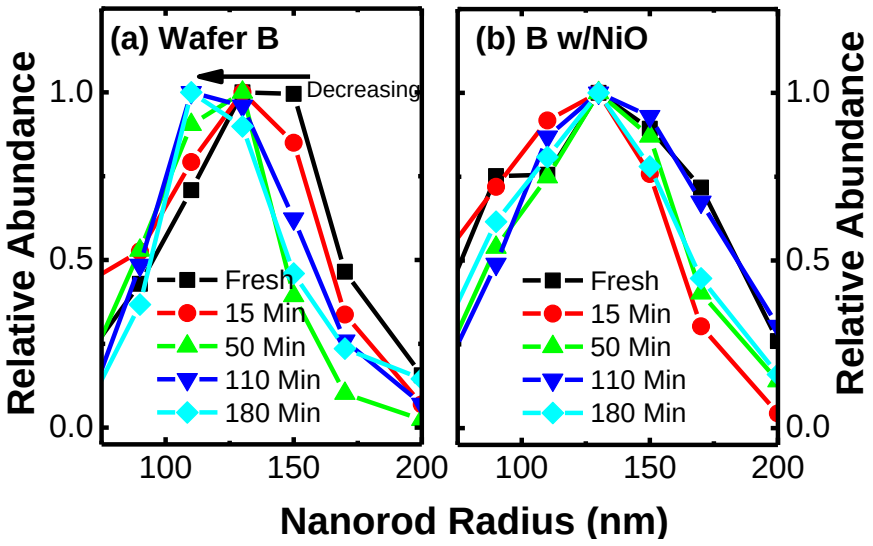

Figure 5-13 – Distribution of nanorod sizes for (a) Wafer B and (b) Wafer B w/NiO

The addition of NiO has effectively protected the nanorods from etching. The coverage of the nanorods for the samples with NiO remains largely unchanged compared to the reference device without NiO in which a 40 % reduction from the initial coverage is observed, as shown in Figure 5-12. Furthermore for the device with NiO nanoparticles, the radii remains similar

during the three hour test It is worth highlighting that the InGaN/GaN is significantly protected from anodic corrosion as a result of the movement of the oxidation reaction to the NiO nanoparticles

5.3 Conclusions

In summary, a considerable reduction in photoelectrochemical etching and a significant enhancement in photocurrent have been achieved as a result of the addition of the NiO nanoparticles to InGaN/GaN nanorod based photoelectrodes for solar power water splitting in a NaOH electrolyte. The increase in photocurrent is attributed to the band gap overlap of the NiO nanoparticles with the device resulting in an increase in electron-hole separation, aiding migration and then reducing recombination. Due to the promotion of the oxidation reaction on the NiO surface as opposed to the device surface, a reduction in the oxidative etching caused by the photogenerated holes accumulated at the GaN/electrolyte interface has been achieved. Thus the photoelectrochemical etching on the device is reduced. Currently, the deposition technique results in the majority of NiO forming on the tops of the nanorods. Altering the deposition method to either a photodeposition technique or a calcination of solution deposited nickel could lead to greater coverage on the nanorod sidewalls. As visible in the SEM images, the sidewalls are etched faster than the tops of the nanorods, therefore improving the coverage could potentially result in further improvements in device lifetimes.

Bibliography

[1] F.E. Osterloh, *Chem. Soc. Rev.* **42**, 2294 (2013).

[2] K. Maeda and K. Domen, *J. Phys. Chem. Lett.* **1**, 2655 (2010).

[3] A. Kudo and Y. Miseki, *Chem. Soc. Rev.* **38**, 253 (2009).

[4] K. Maeda, K. Teramura, D. Lu, N. Saito, Y. Inoue, and K. Domen, *Angew. Chem. Int. Ed. Engl.* **45**, 7806 (2006).

[5] X. Wang, G. Liu, L. Wang, Z.-G. Chen, G.Q.M. Lu, and H.-M. Cheng, *Adv. Energy Mater.* **2**, 42 (2012).

[6] T. Hisatomi, J. Kubota, and K. Domen, *Chem. Soc. Rev.* (2014).

[7] K. Maeda and K. Domen, *J. Phys. Chem. C* **111**, 7851 (2007).

[8] H. Kato, K. Asakura, and A. Kudo, *J. Am. Chem. Soc.* **125**, 3082 (2003).

[9] R. Li, F. Zhang, D. Wang, J. Yang, M. Li, J. Zhu, X. Zhou, H. Han, and C. Li, *Nat. Commun.* **4**, 1432 (2013).

[10] K. Maeda, A. Xiong, T. Yoshinaga, T. Ikeda, N. Sakamoto, T. Hisatomi, M. Takashima, D. Lu, M. Kanehara, T. Setoyama, T. Teranishi, and K. Domen, *Angew. Chemie* **122**, 4190 (2010).

[11] X. Zong, H. Yan, G. Wu, G. Ma, F. Wen, L. Wang, and C. Li, *J. Am. Chem. Soc.* **130**, 7176 (2008).

[12] D. Wang, A. Pierre, M.G. Kibria, K. Cui, X. Han, K.H. Bevan, H. Guo, S. Paradis, A.-R. Hakima, and Z. Mi, *Nano Lett.* **11**, 2353 (2011).

[13] K. Ohkawa, W. Ohara, D. Uchida, and M. Deura, *Jpn. J. Appl. Phys.* **52**, 08JH04 (2013).

[14] S.H. Kim, M. Ebaid, J.-H. Kang, and S.-W. Ryu, *Appl. Surf. Sci.* **305**, 638 (2014).

[15] M. Ono, K. Fujii, T. Ito, Y. Iwaki, A. Hirako, T. Yao, and K. Ohkawa, *J. Chem. Phys.* **126**, 054708 (2007).

[16] M. Grätzel, *Nature* **414**, 338 (2001).

[17] K. Fujii and K. Ohkawa, *Jpn. J. Appl. Phys.* **44**, L909 LP (2005).

[18] K. Aryal, B.N. Pantha, J. Li, J.Y. Lin, and H.X. Jiang, *Appl. Phys. Lett.* **96**, 052110 (2010).

[19] M. Li, W. Luo, B. Liu, X. Zhao, Z. Li, D. Chen, T. Yu, Z. Xie, R. Zhang, and Z. Zou, *Appl. Phys. Lett.* **99**, 112108 (2011).

[20] Z. Cai, K.A. Vallis, and R.M. Reilly, *Int. J. Radiat. Biol.* **85**, 262 (2009).

[21] T. Collins, *Biotechniques* **43**, S25 (2007).

[22] C. a Schneider, W.S. Rasband, and K.W. Eliceiri, *Nat. Methods* **9**, 671 (2012).

Chapter 6

Nanoporous GaN for Enhanced Photoelectrochemical Activity

Porous semiconductor materials have been widely investigated for a variety of applications.[1] The history of porous semiconductors is a long one with their properties investigated as early as 1952.[2] The opportunity they offer is still far from being realised however the potential of porous materials is vast.[1,3] By means of a simple photoelectrochemical etching approach in a KOH solution GaN nanoporous structures with controllable pore sizes have been successfully fabricated. An enhancement in both photocurrent and hydrogen generation has been achieved across all samples with the nanoporous structure compared to their reference un-etched counterparts. A significant enhancement in incident photon conversion efficiency (IPCE) at the GaN band edge, 355 nm, has been achieved.

6.1 Porous Semiconductors in Water Splitting

A variety of porous semiconductors have been studied in water splitting,[4–7] including TiO_2,[8] WO_3[9] and Fe_2O_3.[10] The method of fabrication has been shown to have a significant effect on photocurrent with a factor of 10x change in efficiency for two porous TiO_2 samples fabricated by different techniques.[8] The use of porous materials have been widely explored[11–13] due to their nano structure. As discussed in Chapter 4, the use of nanostructures

can lead to increases in device efficiency as a result of a variety of mechanisms. A porous structure is expected to lead to an increase in surface area of the semiconductor, increased light absorption and the potential for reduced electron-hole recombination. Additionally the porous structures are also expected to enhance the adsorption and desorption of reactants and products.[12] As a result, the turnover of reactions on the surface of a porous device can be significantly higher than those observed in planar structures.

It is worth highlighting another advantage of a nanoporous structure compared to the nanorod structures discussed in Chapter 4. With a porous film, the pore size of the system can be engineering to a size complimentary to that of the minority carrier diffusion length of the semiconductor.[9] In addition, porous structures have been shown to be more effective at absorption of longer wavelengths by controlling the pore size of the structure.[10] It is therefore important to exhibit control over the fabrication technique to produce porous devices with suitable pore sizes and networks. For oxide semiconductors common methods include sol-gel synthesis in which a mixture of precursors is prepared before deposition and heat treatments results in the formation of the porous structure. Alternatively, chemical etching or templating techniques have been utilised.[3] The fabrication technique varies across different material groups with etching and anodization methods utilised in III-V semiconductors.[14,15]

6.2 History of Porous GaN & InGaN

In principle, GaN exhibits remarkable resistance to standard wet chemical solutions,[16] similar to that of diamond and sapphire. Recently, photoelectrochemical (PEC) etching under ultraviolet (UV) illumination, where the photon energy is above the GaN band gap, could be implemented on GaN.[17–19] In 1996, it was found that porous GaN could be fabricated via an photochemical etching technique.[20] The initial method proceeded via the anodization of a hydride vapour phase epitaxial grown GaN wafer in hydrofluoric acid under UV illumination. The pores were found to permeate through the wafer close to the [0001] direction and formed by corrosion of

the *n*-type material. It was suggested that the etching occurs at irregularities in the surface of the material such as defects leading to the reaction of the electrolyte at these areas, resulting in the formation of the pores.[21] Further investigation revealed a reduction in residual stress of the porous layer due to the pore formation at the boundaries of the GaN crystallites. Figure 6-1 illustrates an AFM image of the early porous structures, with pores in the region of 150 nm.

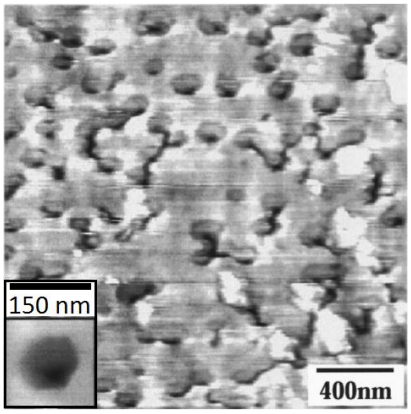

Figure 6-1 - AFM image of early porous GaN layer, inset image displays an enlarged single pit, greyscale of image corresponds to height variation of 150 nm. Adapted from (Mynbaeva, 2000)[21] and permission obtained from copyright holder © AIP Publishing

Alternate methods in the fabrication of porous GaN have been via electrochemical and photoelectrochemical etching and metal assisted electroless etching. The solutions used in each case are varied, but are typically acids or bases.[22] In each case control over the pore size and properties can be controlled by altering the fabrication conditions. Li *et al.* utilised a metal assisted approach in an ethanol, HF and hydrogen peroxide solution and a UV illumination source.[23] Control over the structure was exhibited with respect to etching time and position of the deposited metal. In electrochemical and photoelectrochemical etching, all variables have an effect on the fabrication of the porous structure.[24–27] Youtsey has investigated the effects of PEC etching with potassium hydroxide in which a great degree of control has been exhibited.[17,28–31] The variation in illumination intensity and electrolyte concentration can result in diffusion or carrier limitations. High illumination intensity creates a surplus of carriers leading to

the diffusion of carriers to the electrolyte limiting the reaction. Alternatively, if illumination intensity is low the number of carriers limits the overall rate of reaction. Porous InGaN has been formed by etching in HF and more recently via UV assisted electrochemical (PEC) etching.[32] Relatively small pores were formed in the InGaN with the KOH solution due to the short etching time. Currently, there are no published reports on porous GaN nanorod structures however porous nanowires have been grown by thermal chemical vapour deposition with pore sizes in the range of 5-20 nm on 10-80 nm nanowires.[33]

Nanoporous GaN has wide applications. Porous structures have been utilised as growth templates,[26,34,35] upper layers on LED devices[36–38] and in gas sensing applications.[39–41] In the case of porous GaN for use as growth templates, lateral overgrowth techniques on the porous templates has resulted in strain relaxation of the bulk material leading to improved chemical and optical properties.[21,42–44] For LED devices, roughening of the structure and partial strain relaxation have been identified as reasons behind the improved device performances.[37]

6.2.1 Etching Process

Photoelectrochemical etching of GaN is essentially the same process as anodic etching which was described in Chapter 2 and 5. PEC etching in a basic medium proceeds via the following reactions.

$$2GaN + 6h^+ \rightarrow 2Ga^{3+} + N_2 \uparrow \quad \text{(i)}$$

$$2\mathrm{GaN} + 6\mathrm{OH}^- + 6\mathrm{h}^+ \rightarrow 2\mathrm{Ga_2O_3} + 3\mathrm{H_2O} + \mathrm{N_2} \uparrow \quad \text{(ii)}$$

$$\mathrm{Ga_2O_3} + 6\mathrm{OH}^- \rightarrow 2\mathrm{GaO_3}^{3-} + \mathrm{H_2O} \quad \text{(ii)}$$

Equation 6-1 – Photoelectrochemical etching mechanism of GaN

It is therefore possible to control the reaction through the hydroxide ion concentration and the number of photogenerated holes under illumination. Variation in either of these can therefore alter the nature of the reaction. There is also a dependence on crystal orientation in regards to GaN, with the N and Ga terminated faces behaving differently in different

conditions.[22] The etching proceeds via the formation of an oxide layer on the GaN surface which is dissolvable in a hydroxide solution. As a result, the formed oxide is continually formed and then dissolved throughout the duration of the reaction. Without the presence of photogenerated holes at the surface the reaction cannot proceed. Therefore without a source of illumination or if *p*-GaN is utilised no etching will be observed.[17] As alluded to previously, the etching proceeds via recombination centres. Defects within the GaN surface can serve as traps for electrons and holes leading to the recombination of the carriers preventing etching. As a result, typically the centre of the GaN crystal structures are attacked as opposed to the threading dislocations in the epitaxial layer.[26,45] After the initial layers are etched, successive growth layers beneath the surface layer can be attacked resulting in the formation in a network of pores in the structure.

6.2.2 Etched GaN/InGaN in Water Splitting

PEC etching has been utilised for the formation of highly smooth surfaces,[30] defect idetification[46] and enhanced LED light output.[47] However, despite the long history in the fabrication of porous GaN it has been hardly implemented in its application in water splitting. Guo *et al.* prepared porous GaN via a platinum assisted electroless etch which resulted in an enhanced UV photocurrent response.[48] The increased response was attributed to the change in conductive area. This report demonstrated the potential for an increase in photocurrent of porous GaN however did not investigate the potential in water splitting. Ryu *et al.* reported both electrochemical etching and photoelectrochemical etching of GaN for water splitting.[49] In their report, the nanoporous GaN was fabricated in a 0.3 M oxalic acid solution with a supplied voltage of 15 V for 10 minutes. The pores were approximately 30 nm in diameter with a density of 2.9 $x10^{10}$ cm^{-2}. The response of the electrochemically etched device was higher than the planar sample which was attributed to an increase in surface area and enhanced hole transport. Interesting to note in their report is due to the enhanced formation of defects as a result of their photoelectrochemical etching, a detrimental effect on photocurrent is observed.[50]

There are other etching techniques reported, where improvements in photocurrent have been achieved. In these cases, the etching has been utilised as a surface treatment to remove defects as opposed to the fabrication of nanoporous GaN.[51,52] Basilio *et al.* utilised a PEC etch in KOH and a hot H_3PO_4 treatment. After the initial PEC process the photocurrent of the system had reduced significantly with a delayed turn-on compared to the pristine sample.[51] This was attributed to an increase in localised carrier concentrations at the surface of the semiconductor and the formation of non c-plane facets causing the delayed turn-on. Li *et al.* have reported the only use of an etch treatment on an InGaN based device.[52] An electrochemical treatment was conducted in 1 M HCl leading to an enhanced photocurrent and incident photon conversion efficiency. Due to the growth of bulk InGaN, indium rich regions were present at the surface leading to recombination centres. It was posed that the etch process removes these allowing for better separation of the electron and holes resulting in an increase in the photocurrent of the device.[52]

6.3 Nanoporous GaN

The benefits observed in oxide semiconductors due to the fabrication of porous structures have not yet been fully explored in III-nitride based devices. Current reports indicate the potential for electrochemical etching of GaN however this has not gone further than simple porous structures. Alongside this, porous InGaN devices have not yet been investigated for water splitting.

6.3.1 Fabrication

Planar Porous GaN

A typical as-grown wafer is prepared via MOCVD growth technique as previously described in Chapter 4. Following this a photoelectrochemical etch is utilized as the process to form the nanoporous devices. The photoelectrochemical etch follows a similar procedure to typical photoelectrochemical device assessment. GaN samples with an insulated Ti/Au ohmic contact acts as the working electrode in a photoelectrochemical

cell comprised of a UV fused silica optical window, electrolyte and counter electrode. A platinum wire acts as the counter electrode and a potassium hydroxide solution as the electrolyte. A Keithley 2401 source measure unit (SMU) acted as bias voltage source and ammeter. The illumination source was a 300 W ozone free Xe lamp with a solar filter applied. Seven samples were fabricated labelled as A-G. The conditions for fabrication are listed in Table 6-1. Sample A is a typical as-grown sample used as a reference for comparison while samples B-G are the fabricated nanoporous structures.

Table 6-1 – Fabrication conditions of planar porous structures

Sample No.	KOH (wt. %)	Etch Time (min)	Voltage (V)	Avg. Pore Size (nm)
A	-	-	-	-
B	1	30	10	50
C	0.5	30	10	40
D	0.1	30	10	25
E	0.5	30	5	35
F	0.5	30	20	60
G	1	30	0	20

Porous Nanostructure GaN

The fabrication of the nanostructured porous GaN followed the same procedure as described in Chapter 4. A Ti/Au contact was deposited onto the preformed contact area of the nanorod device before a wire was bonded and insulated. PEC etching of the nanorods for the creation of the nanoporous structure followed using the same technique described above. Six samples were fabricated, labelled as samples H-L. Sample H is the reference nanorod sample while samples I-L are the nanoporous structures. Conditions for the fabrication are listed in Table 6-2. Samples H, I, J and K have a typical nanorod diameter of 220 nm while sample L has been deliberately fabricated with a wider nanorod size of ~300 nm.

Table 6-2 – Fabrication conditions of nanorod porous structures

Sample No.	KOH (wt. %)	Etch Time (min)	Voltage (V)	Avg. Pore Size (nm)
H	-	-	-	-
I	1	15	20	50
J	0.1	15	20	35
K	0.1	15	10	30
L	0.1	20	20	35

6.3.2 Characterisation

As discussed the fabrication conditions are vitally important in the fabrication of a nanoporous structure in GaN. It is however very easy to alter the concentration and voltage supplied during PEC etching to obtain the necessary control. A set of as-grown and nanorod samples were fabricated from a set of GaN wafers that were grown in the same growth run. Hall measurements were conducted on the sample indicating a doping level of 1.3 $x10^{18}$ cm^{-3}. The doping level plays a role within the etching of the material due to its conductivty.[28] The *n*-type layer has a thickness of 1.8 µm. For the fabrication of nanoporous structure, the influence of the applied voltage and etchant concentrations have been systematically studied. Two sets of nanoporous structures have been fabricated, (1) nanostructures fabricated from the planar as-grown wafer; (2) nanostructure fabricated from the prepared nanorod arrays (the detailed fabrication of nanorod array structures can be found in Chapter 4). Table 6-1 and Table 6-2 provide fabrication summaries of the nanostructures fabricated from the planar as-grown structures and nanorod structures respectively. A concentration gradient of 0.1-1 wt % was utilised as well as voltages ranging from 0 to 20 V for the planar structures. Etch times were set at a maximum of 30 minutes and the measured illumination intensity ~200 mA cm^{-2}. The conditions were similar for the nanorods however the etch time was reduced to take into account the considerably larger active surface area of the fabricated nanorods.

Photoluminescence

Photoluminescence (PL) was performed using a 325 nm He-Cd laser dispersed by a 0.75 m monochromator and detected by an ultraviolet enhanced CCD detector for all samples. The normalised spectrum for the planar porous samples is presented in Figure 6-2. For all the samples, a red shift in emission wavelength has been observed. In detail, a red shift of 1.2 nm for samples B, C and D has been observed, and 1.7 nm for sample E, 1.9 nm for sample F and 1 nm for sample G, respectively. In agreement with Yam[53] there is no clear correlation between shift in emission wavelength and pore size.

However, interesting to note is a potential relationship between peak shift and etch voltage. Looking at samples G, E and F with etch voltages of 0, 5 and 20 V respectively, the peak shift increases from 1 to 1.9 nm. This is likely related to the degree of etching that has occurred relating to the level of relaxation in the bulk GaN.

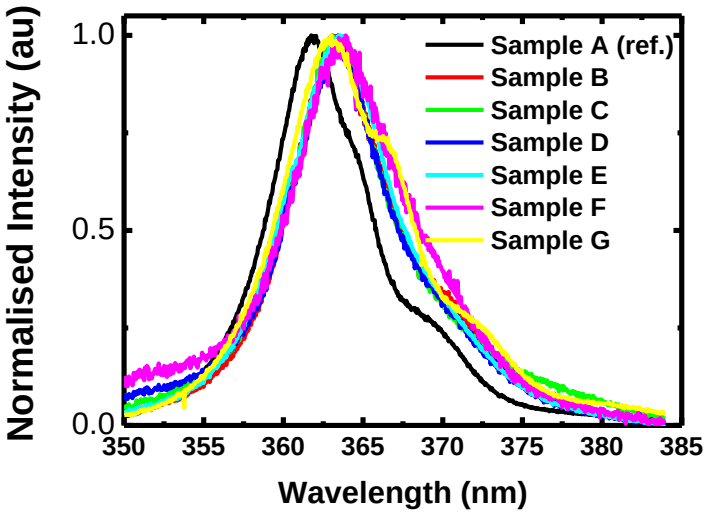

Figure 6-2 – Normalised room temperature PL spectra of nano porous structures fabricated from a planar as-grown wafer

Due to a large lattice-mismatch of ~16% between GaN and sapphire substrate, GaN epitaxial layers on sapphire suffer from a great compressive strain. Under fully strained conditions the compressive strain present within a GaN substrate grown on an AlN buffer layer on sapphire is approximately 0.2 GPa for the GaN and 1.77 GPa for the AlN.[54] As a result of the formation of the nanoporous structures the strain can be largely relaxed, leading to the red shift observed in PL emission peak. The extent of red-shift depends on the degree of relaxation. From the data, the level of strain relief can be estimated using the proportionality factor (K), where K=21.2±3.2 meV/GPa for GaN.[54] From the least to most severe peak shift, total strain relief is from 0.43 meV to 0.85 meV which indicates a significant reduction in total compressive strain. The data shown in Figure 6-2 is comparable to the previous reports on porous GaN where the relaxation has been confirmed by Raman spectroscopy.[24,44]

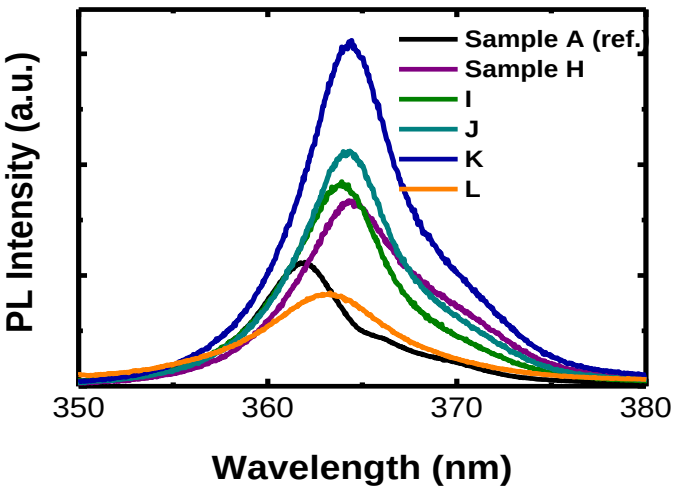

Figure 6-3 – Room temperature PL for nanoporous nanorod samples H-M. The as-grown sample A has been included as a reference.

Room temperature PL of the nanoporous structures fabricated from the prepared nanorod samples was also conducted. As previously discussed, the formation of a nanorod array causes a reduction in strain compared to the as-grown sample. This leads to a red shift as observed in Figure 6-3. For the fabricated nanorods the shift observed is 2.4 nm or a strain relief of ~1 GPa, which indicates an almost complete release in compressive strain. The peak shifts of the porous samples vary from 1-2.4 nm with samples etched under a lower concentration (K and L) exhibiting the largest peak shift compared to the as-grown sample. The difference in peak shift of the porous samples is attributed to the changing etching conditions resulting in varied porous structures.

Full width half maximum measurements of the room temperature PL reveal values of 5.75 nm for the as-grown reference sample (A) and 8, 6.1, 6.2, 6.3 and 8.3 nm for samples H-L respectively. This suggests that the relative contribution of the nanorods and porous structure towards the strain relief changes dependent on the level of etching. The change in intensity observed for each sample also varies depending on the etch conditions. The enhancement in PL emission for the porous nanorod samples can be attributed to an enhancement in extraction and also in absorption due to scattering between and within the nanopores of the nanorods and an

increase in surface area resulting in an increase in greater number of excited carriers.[24,25,55]

SEM Measurements

The morphology of the nanoporous samples was investigated by scanning electron microscopy. Figure 6-4 illustrates a typical cross sectional image and plan view images of each etched sample. In Figure 6-4(a) two layers are clearly visible. One is a nominally doped GaN layer and an AlN buffer with a total thickness of 0.8 μm for the lower part (see sample preparation section), and another is an *n*-doped GaN with a thickness of 1 μm for the upper part. It is clear that the nanopores are formed in the *n*-doped GaN layer only, confirmed by observing a visible termination of the pores at the boundary between the doped and undoped layer. Compared to the initial *n*-GaN layer thickness a decrease of over 500 nm is observed. The pores also follow a linear structure through the wafer indicating that the etching occurs at the grain centres as previously discussed. The termination of the etching is attributed to the significant difference in carrier concentration between the intrinsic and doped GaN. As a result, the resistivity of the intrinsic GaN is considerably higher than *n*-doped GaN preventing effective carrier flow, thereby preventing the etching of the lower wafers. This indicates that a level of control by varying dopant concentration could be achieved.[28]

The sizes of nanopores has been examined through measuring the top-down SEM images, which are given in Figure 6-4b, c, d, e, f and g, corresponding to sample B, C, D, E, F and G respectively. Sample B, C and D form one group, where the samples were fabricated as a function of KOH concentration under an identical voltage. Another group of samples, consisting of sample E, C and F, were fabricated as a function of a supplied voltage from 5 to 20 V but using the same KOH concentration. Sample G is comparable to sample B due to identical etchant concentrations however the applied voltage has been reduced to 0 V to assess the etchant rate due solely to illumination. As a result of hydroxide ion consumption in both the formation and dissolution reactions (refer to Equations 2 and 3), the concentration of the KOH etchant is essential in controlling whether the

reaction is carried out under a mechanism due to diffusion (low concentration, high illumination) or carrier (high concentration, low illumination) limitations.

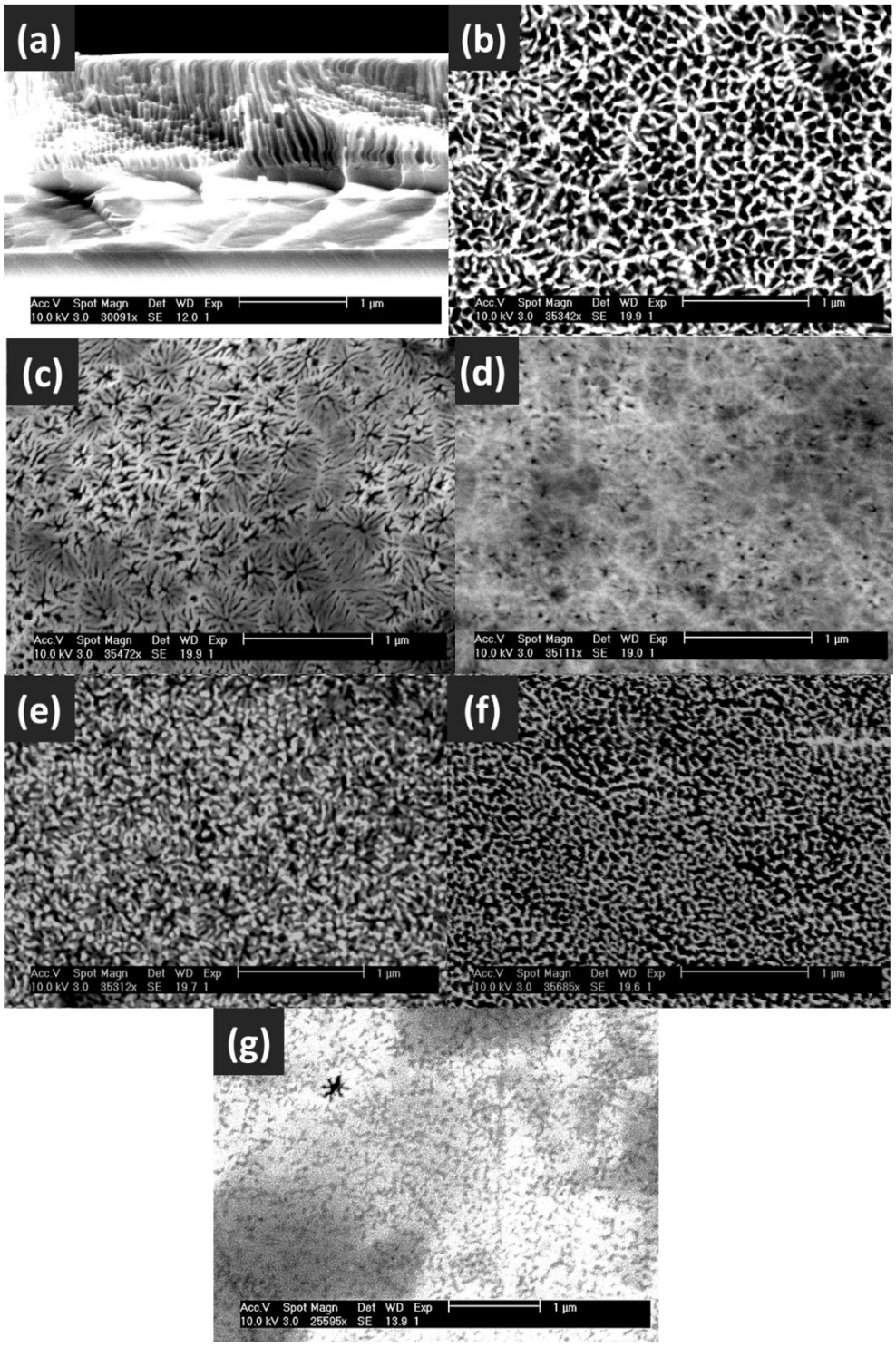

Figure 6-4 – SEM images of porous GaN samples. (a) typical cross section of porous samples obtained from sample C. (b)-(g) top down SEM images of samples B-G respectively

With an increase in KOH solution an increase in pore size has been obtained (Samples B, C and D) as altering the KOH concentration ultimately changes the concentration of the total ions in the reaction, increasing the availability of hydroxyl ions and therefore generating a greater number of etch sites across the GaN surface as the hydroxyl ions permeate through the solution. At low ion concentrations (0.1 wt %, Sample D), there is a limit to the number of interactions at the semiconductor-KOH interface and therefore under diffusion controlled scenarios a reduced degree of etching is observed. Altering the bias conditions of the etching also leads to a change in the number of ions in solution, as above the reduction-oxidation potential of water (1.23eV) there is an increase in the dissociation of the electrolyte and therefore an increase in the OH^- concentration. Alongside this, when under bias, the separation of the photogenerated electron-hole pairs is more efficient as a result of the increased conductivity, further increasing the number of potential reactions. Therefore, as observed an increase in the degree of etching occurs at higher biases (Sample F). In agreement with this, the etching of sample G occurs purely from the photogenerated carriers which results in a lesser etch.

Similar observations have been observed in the fabrication of nanoporous structures prepared from the nanorod structures with the more enhanced etch conditions (such as higher concentration of KOH) resulting in a greater degree of etching, which can be observed in Figure 6-5. Comparing samples I, J and K in Figure 6-5(b), (c) and (d) Sample I exhibits a significant degradation as a result of the higher concentration of the KOH etchant used compared to that for samples J and K, leading to a significant reduction in the nanorod structure while samples J and K retain the nanorod structure. FWHM measurements of the room temperature PL provide supporting evidence towards these results. For the reference as-grown and nanorod structures a value of 5.7 nm and 8 nm is obtained. As the etch severity decreases the FWHM of samples I, J and K, increases to values more similar to that of the un-etched nanorod from values of 6.1, 6.2 and 6.3 nm respectively. Furthermore, the nanoporous nanorod sample with a wider diameter

(Sample M) still retains the nanorod structure, visible in Figure 6-5 (e) which results in a FWHM value of 8, comparable to the un-etched nanorods.

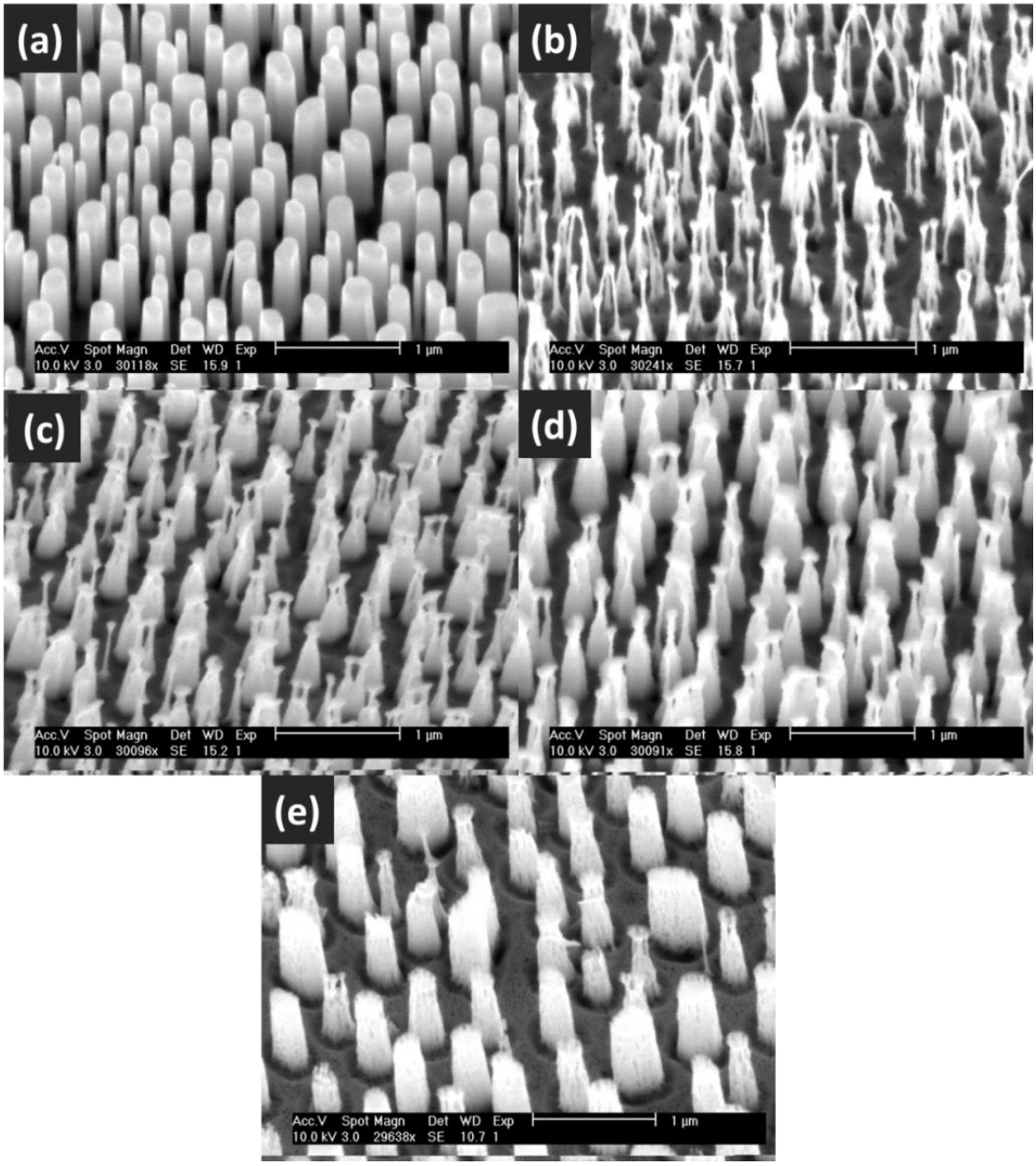

Figure 6-5 – SEM images of porous nanorod samples. (a) reference nanorod sample (b)-(e) porous nanorod samples I-L

Comparing the wider nanorods with the reference nanorod sample also provides interesting results. Sample J and I have similar etch conditions with the etch time altered only, however there is a significant difference in the etched structure as observed in Figure 6-5 (c) and (e). The wider nanorods have become visibly porous in a similar manner to the bulk material whereas a visible thinning of the nanorods has occurred to Sample J. Due to

the differences in surface area, the recombination dynamics of the two samples will be different resulting in the appearance change. This also indicates that a wider structure is required to create similar pores to those observed in the bulk material which may offer performance benefits over the reference sample.

6.3.3 Solar Hydrogen Performance

Hydrogen generation potential has been assessed by measuring the photocurrent of the devices. These tests were conducted in HCl, a standard electrolyte for water splitting, where GaN exhibits high chemical resistance. The measurements have been conducted in a 1 M solution under solar filtered Xe lamp illumination at 100 mW cm^{-2}. Figure 6-6 (a) shows the typical photocurrent as a function of bias for the different GaN nanoporous structures under both illumination and dark conditions, where the set of GaN nanoporous structures (fabricated from a planar as-grown GaN layer) were fabricated based on the utilisation of KOH with different concentrations, i.e., sample B, C and D, respectively. As a reference, the data for the as-grown GaN structure (labelled as sample A) is included. As demonstrated in the SEM shown in Figure 6-4, an increase in the concentration of the fabrication solution (i.e., KOH) results in larger pores, and as observed from the photocurrent measurements (Figure 6-6 (a)) an enhancement in performance. In fact, nearly all the photoelectrodes fabricated based on the nanoporous structure exhibit an increase in photocurrent compared to the as-grown device. This is thought to be attributed to the increase in surface area gained from the creation of a nanoporous structure. This provides a greater number of active areas for the solution to react with the surface, thus allowing greater current flow between the semiconductor and electrolyte. Not only this, the nanoporous structure will also create cavities in which the incident light can propagate through the sample, leading to significant enhancement in the total amount of radiation absorbed. Without a significant level of etching, as observed in Sample G, an increase in photocurrent is not observed.

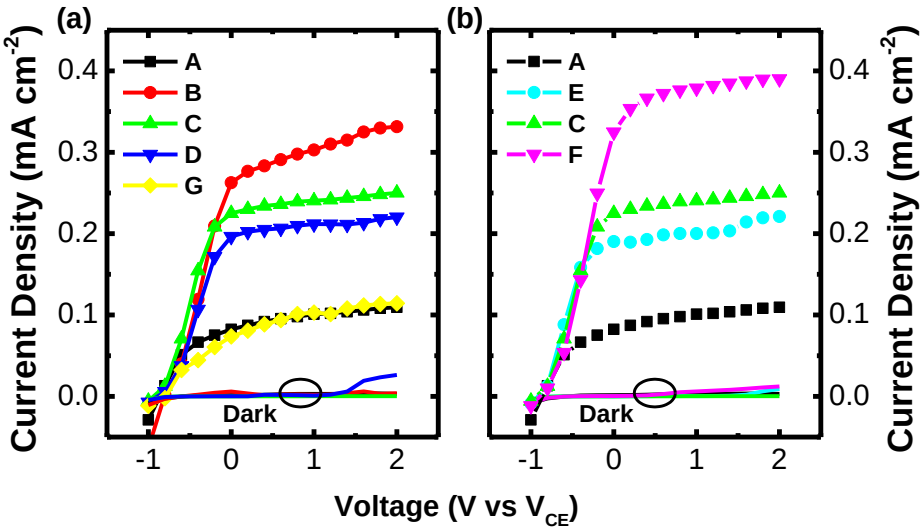

Figure 6-6 – Photocurrent as a function of bias under dark and illuminated conditions for (a) the samples fabricated under difference KOH concentrations; and (b) the samples fabricated under different voltages supplied

Figure 6-6 (b) shows the typical photocurrent as a function of bias under both illumination and dark conditions for the nanoporous structures fabricated using the different supplied voltages but identical KOH concentrations, i.e., sample E, C and F, respectively. As shown in Figure 6-4, an increase in voltage supplied results in a rise in pore size. Consequently, it leads to significant enhancement in photocurrent for assessing the solar hydrogen performance, which is similar to Figure 6-6 In comparison to the un-etched as-grown sample across the potential working voltages (0-1V) the increase in photocurrent for samples B, C and D are 308 %, 253 % and 222 % respectively, where the pore sizes of sample D, C and B are in an increasing order. This suggests that the fabrication of nanoporous GaN used as a photoelectrode is a very efficient and cost-effective approach to achieving significant improvement in energy conversion efficiency. Comparison of the two GaN sets of samples suggests that it is more efficient to fabricate the nanoporous structures with larger pore size through increasing the supplied voltage. For instance, Sample F, which was fabricated using 20 V, the highest voltage used in the present study, demonstrates the highest enhancement in photocurrent, which is 390 % higher over the aforementioned working voltages than that for the as-grown sample (i.e., sample A). Comparing the

efficiency of the as-grown device and sample F, the performances increases from 0.1 % to 0.43 % when no bias is applied, a factor of 4 improvement.

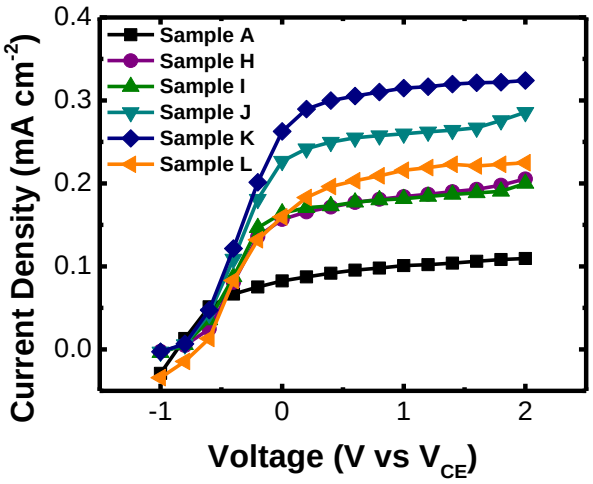

Figure 6-7 – Photocurrent as a function of bias for the reference as grown device (Sample A), reference nanorod device(Sample H) and porous nanorod devices (Samples I-L)

Similar results have also been observed in the nanoporous structures fabricated from nanorod templates. As discussed in Chapter 4, the fabrication of a nanorod structure can increase the performance of a device significantly over an as-grown device. The reference nanorod device (Sample H) fabricated in this sample set results in a two-fold increase compared to the as-grown device (Sample A). Photocurrent measurements at biases from -1 V to 2 V are illustrated in Figure 6-7. In contrast to the planar porous structures, a reverse relationship between etch severity and photocurrent is observed with Sample K demonstrating the greatest improvement in photocurrent compared to the reference nanorod device. Compared to non-porous reference nanorod device the averaged change in photocurrent over 0 – 1 V is 102 %, 142 %, 168 % and 110 % for samples I-L, respectively. Sample I has a similar response to the reference nanorod device. Based on the severe etching of the nanorods visible in Figure 6-5 a decrease in photocurrent would've been expected due to the enhanced damage of the device. However, the photocurrent remains unchanged which is attributed to the fabrication of the porous bulk GaN layer beneath the fabricated nanorods which has been shown to increase photocurrent. With a decrease in etch severity, the

combined benefits of a nanorod and porous structure can be obtained, as demonstrated in samples J-L. Despite this, Sample L, with obvious pores within the nanorods does not generate the greatest change in photocurrent. Based on the room temperature PL FWHM measurement, Sample L indicates a value closest to the reference nanorod structure (Sample H); this suggests that the bulk layer is not as severely etched as samples I-K which indicates that the total surface area may not have increased to the same extent as Samples J and K.

Hydrogen Generation

Assessment of the hydrogen generation performance was conducted for selected comparative samples and is detailed in Figure 6-8. The volume of hydrogen was collected via the use of an upturned burette over the platinum electrode allowing bubbles to displace a small volume of water. Theoretical volumes of hydrogen were calculated from the obtained photocurrent values using Equation 4,

$$\frac{dN_{H_2}}{dt} = \frac{i}{nF} \qquad (4)$$

where *i* is the number of current, *n* is the number of electrons required, *F* is the Faraday constant and N_{H_2} is the moles of hydrogen produced. This can be converted into millilitres assuming a volume of 22.4 dm^3 mol^{-1} for hydrogen gas under standard temperature and pressure. All samples show a good agreement with the theoretical values, with slight discrepancies attributed to the visual inspection of the burette. The nanoporous GaN samples in Figure 6-8 all had a planar area prior to porous fabrication within 0.02 cm^{-2} of each other based on detailed measurements on the sample surface and are therefore comparable. In good agreement with the previous photocurrent results, the ability of the porous samples for hydrogen generation is increased with Sample D demonstrating a two fold increase and Sample K a threefold increase over the reference as-grown sample (Sample A). As discussed, this is attributed to the increase in surface

area of the samples allowing for improved charge-transfer and the better adsorption and desorption properties of the nanoporous structure.

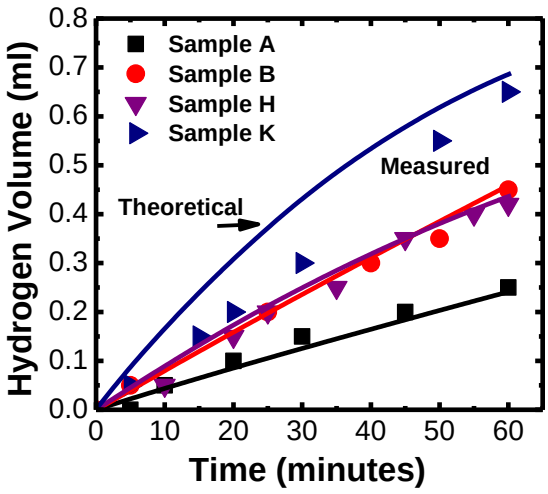

Figure 6-8 – Measured (points) and theoretical (solid lines) hydrogen values for porous samples at 0.8 V bias in HCl under 500 mW cm^{-2} illumination for as-grown GaN (A), porous GaN (D), nanorod GaN (H) porous nanorod GaN (K)

Incident Photon Conversion Efficiency

The wavelength dependent performance, namely, incident photon conversion efficiency (IPCE), an important performance indicator, can be calculated using Equation 4 below,

$$IPCE(\%) = 1240 \times \frac{J(mAcm^{-2})}{\lambda(nm) \times I(mWcm^{-2})} \times 100\% \qquad (5)$$

where J is the photocurrent density, λ the wavelength of incident light and I the incident power density. The IPCE of all samples except G and L have been measured using a 75 W xenon lamp over a wavelength range of 320-600 nm, which are shown in Figure 6-9. All the GaN nanoporous samples, as expected, demonstrate a significant increase in IPCE compared with the reference as-grown sample (Sample A).

The response from the GaN samples extends from the deep UV until a sharp decline after the band edge emission at 355 nm. This is as a result of the band gap of GaN at 3.6 eV, therefore due to the low availability of solar energy it is vital to increase the efficiency at the available wavelengths. The porous planar samples shown in Figure 6-9(a) indicate a similar trend to

those observed from the photocurrents with Sample F performing better than all other samples. Comparatively, the performance of the reference as-grown sample at the GaN band edge of 355 nm is 20.7 % comparable with other reports for GaN[56,57] while the efficiency of Sample F is 43.4 % over twice that of the reference as-grown structure indicating that the porous structure has significantly enhanced the utilisation of the photo generated carriers. Alongside this the efficiency of the reference nanorod structure is 49 % while the porous nanorod, Sample K, has a peak efficiency of 69.3 % at 355 nm. The decrease in distance for the minority carriers to diffuse, along with the reduction in recombination centres due to the creation of the porous structures causes the enhancement in IPCE observed in the nanoporous planar and nanoporous nanorod samples.

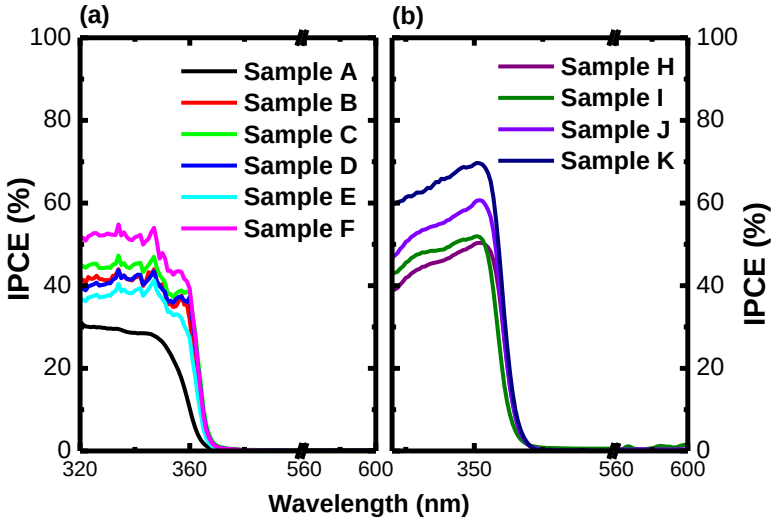

Figure 6-9 – Incident Photon Conversion Efficiency (IPCE) as a function of wavelength for (a) GaN based nanoporous structures and (b) the porous nanorod structures

6.3.4 Summary

The fabrication of porous structures via photoelectrochemical etching in a potassium hydroxide solution has resulted in an improvement in the performance of planar and nanorod devices. Control over the severity of the etch has been obtained through altering the concentration, voltage and etch time. This has resulted in a specific control in pore size in which larger pores have resulted in the greatest enhancement in the planar devices.

Comparatively, the nanorod structure requires milder etch conditions to prevent the complete degradation of the nanorod structure and generate a porous structure. Altering the diameter of the nanorod leads to a decrease in total etch of the bulk GaN indicating further etching is required to achieve the optimum increase with larger nanorods. Photocurrent measurements increase by a factor of four for the planar porous device compared to the reference as-grown device while the porous nanorods demonstrate a two fold increase over the reference nanorod device.

The nanoporous structure increases the surface area of the device as well as providing benefits for hydrogen generation due to improving the adsorption and desorption properties of the GaN. Alongside this, the porous structure decreases the distance required for the photo generated carriers to migrate to the semiconductor-electrolyte interface. The work conducted is also one of the only reports on porous nanostructured GaN and demonstrates the potential of a KOH etch for enhanced photocurrents.

6.4 NiO Nanoparticles on Nanoporous GaN

Due to the potential issue of corrosion arising with the creation of a nanostructure, as observed in Chapter 5, methods to quell this reaction are required. As observed with the nanorod structures, the addition of NiO resulted in a marked improvement in both photocurrent and corrosion prevention.

6.4.1 Fabrication

A reference as grown *n*-GaN wafer with a doping density of 1.7 x 10^{18} cm^{-3} was utilised for the fabrication of a nanoporous device. A typical Ti/Au ohmic contact was thermally deposited onto the sample prior to the bonding of a copper wire with conductive epoxy. The contact was then insulated before testing occurred. As with the samples previously fabricated, a PEC etch method was implemented using a 1 wt % KOH etchant solution, 20 V bias and an etch time of 30 minutes. The GaN acted as the working electrode while a platinum rod acted as the counter electrode. Following porous fabrication, the contact was lifted off from the device leaving an un-etched

contact area and a nanoporous area on the device. The NiO formation followed the same method discussed in Chapter 5. Namely, the deposition of an 8 nm nickel film, annealing at 820 °C in a nitrogen atmosphere to form nickel nanoislands and finally an oxidation stage at 520 °C for 30 minutes leading to the formation of NiO nanoparticles on the surface of the device. An ohmic contact was then re-deposited and insulated for device characterisation.

6.4.2 Characterisation

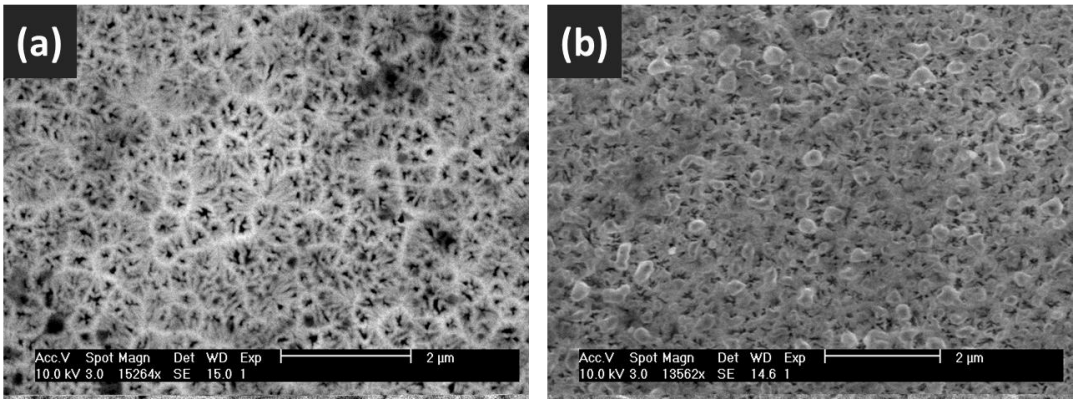

Figure 6-10 – SEM images of (a) nanoporous sample (b) nanoporous sample with NiO nanoparticles

SEM images of the device were taken before and after the NiO deposition. As visible in Figure 6-10 the nanoporous sample has a network of pores averaging 70 nm in diameter. The pores have formed within the grain centres as observed in previous samples with an almost circular shape. After the deposition and formation of the NiO, the NiO particles are observable across the sample with a relatively uniform diameter of 200 nm.

6.4.3 Solar Hydrogen Performance

Photocurrent measurements for the two samples were taken under one sun illumination in a 1 M HCl solution. Measurements were conducted as a function of voltage and versus a prolonged time period to assess the effect of the NiO on the porous GaN. As demonstrated in Figure 6-11, the addition of the NiO causes a delayed turn-on voltage when compared to the porous structure due to the difference in band alignments of the device due to the NiO addition. Despite the delayed turn-on, at applied biases, as observed

previously, the NiO nanoparticles provide an enhancement in the photocurrent of the device due to the enhanced separation of the electrons and holes due to the discontinuity in the conduction and valence bands of the GaN and NiO. Assessment of the stability of the device was conducted over a three hour period (Figure 6-11(b)). The photocurrent of the device is relatively stable indicating that no etching of the device is occurring.

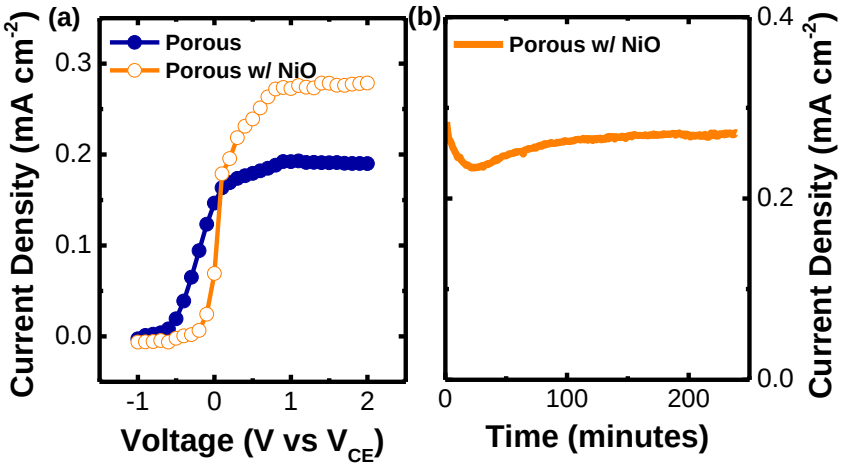

Figure 6-11 – Photocurrent measurements under one sun illumination in 1 M HCl (a) photocurrent as a function of voltage for porous and porous w/ NiO (b) photocurrent versus time for the porous NiO sample at 0.8 V bias

6.4.4 Summary

Addition of NiO nanoparticles onto porous GaN has been demonstrated as feasible resulting in the same enhancements and benefits observed in the nanorod samples. As previously seen in the nanorod samples, the enhanced activity of a device can result in an increase in the anodic corrosion of the nitride material. It is therefore essential that this is prevented in order to realise the potential benefits the fabricated nanostructure can offer. Therefore, the combination of a porous structure with NiO nanoparticles has the benefits of an increased surface area, enhanced migration of carriers to the surface of the electrode due to the porous structure while further etching is prevented due to the preference for holes to migrate to the NiO particles. Optimisation of the fabrication conditions to complement both techniques has the potential to create a uniform heterostructure with performances above and beyond those currently achieved.

6.5 Nanoporous InGaN/GaN MQW

There are very few reports on porous InGaN samples[32,58,59] and therefore they have not yet been investigated for water splitting. As with other nanostructures, if the fabrication of a porous InGaN sample can be fabricated there is the potential for significant improvements in photocurrent. With the short diffusion length of InGaN[60] compared to GaN a network of pores with controlled sizes has the potential to allow for improved carrier separation and reduced recombination.

6.5.1 Fabrication

A InGaN/GaN multi-quantum well (MQW) wafer was utilised in the fabrication of the porous devices. The wafer consisted is grown on c-plane sapphire with a 1.4 μm undoped GaN buffer, followed by 2.8 μm silicon doped GaN (*n*-GaN), a thin $In_{0.05}Ga_{0.95}N$ strain release layer, and 10 periods ($In_{0.15}Ga_{0.85}N$: 2.5nm/GaN: 13.4 nm) multiple quantum wells (MQWs). A typical AlGaN layer with ~20 nm is used as an electron blocking layer (EBL). Finally, the sample is capped with 230 nm *p*-doped GaN. Four samples were fabricated. These consisted of two nanorod samples fabricated by the same method described previously with a diameter of 220 nm and a density of 10^8 cm^{-2} and two planar samples. One sample of each set was utilised in the creation of a porous structure. As with the GaN devices, the porous samples were fabricated via the use of a KOH solution under illumination from a 300 W Xe lamp. The concentration and applied biases were 1 wt% and 20 V for both planar and nanorod samples. The etch time was set at 15 and 10 minutes for each device respectively (Table 6-3).

Table 6-3 – Fabrication conditions and pore sizes of InGaN/GaN MQW samples. A is planar sample, B is porous planar sample, C reference nanorod sample and D porous nanorod sample.

Sample No.	KOH (wt. %)	Etch Time (min)	Voltage (V)	Avg. Pore Size (nm)
A	-	-	-	-
B	1	15	20	30-120
C	-	-	-	-
D	1	10	20	25

6.5.2 Characterisation

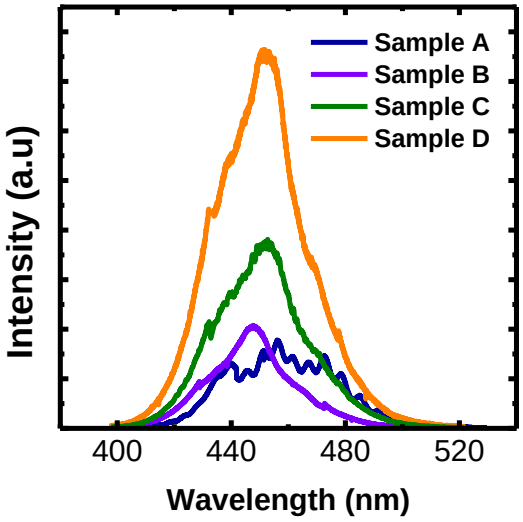

Figure 6-12 – Room temperature PL measurements of InGaN/GaN MQW devices. A = planar reference B = porous planar C = nanorod reference D = porous nanorod

Photoluminescence was performed using a 375 nm diode laser for the InGaN/GaN samples with the luminescence dispersed by a 0.75 m monochromator and detected by a Jobin Yvon CCD. The InGaN/GaN MQW device however it is a blue shift in the InGaN/GaN peak that occurs (Figure 6-4). Compared to the as-grown device, a blue shift of 8.5 nm, 3.3 nm and 4.3 nm is observed for the porous, nanorod and porous nanorod samples respectively. In both cases, the fabrication of a nano structure in the device partially relieves some of the strain as a result of the lattice mismatch of both the substrate and GaN and the InGaN and GaN. The reduction in strain leads to a decrease in the in-built piezoelectric field of the quantum wells leading to the blue shift. The change in the strain is also partially responsible for the increase in emission observed from the porous sample.[37] The enhancement in PL of the nanorod InGaN/GaN device is attributed to the increase in IQE of the sample as previously reported.[61,62] With the addition of a porous structure, as with the GaN device, light can easily propagate through the sample and the enhanced surface area of the device also results in an increase in emission.

Scanning electron microscopy of the fabricated porous InGaN/GaN samples were investigated to determine the extent of the etch. The porous

InGaN/GaN MQW sample shown in Figure 6-11 (a) & (b) clearly shows some variation in the extent of etching across the surface. Due to the structure of the wafer, with an upper *p*-GaN layer, the etching across the surface takes longer to occur than with *n*-GaN. This causes considerably smaller pores in the upper layer compared to planar *n*-GaN as observed in Figure 6-4 despite similar etch conditions. However, once an area is etched, the underlying layers comprised of the InGaN/GaN MQW layers are etched at a faster rate, resulting in the larger pores visible in Figure 6-11 (b). The distribution of the more severe etching is sporadic, resulting in partial exposure of the quantum wells. Despite this, the porous structure observed will still result in increased contact of the quantum wells with the electrolyte solution decreasing the required carrier diffusion length.

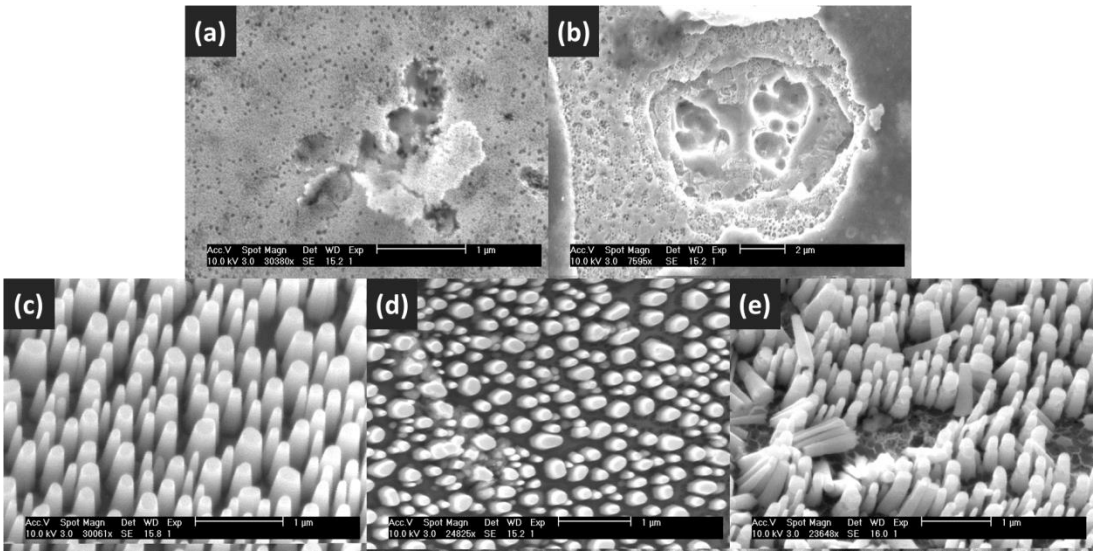

Figure 6-13 – SEM images of porous InGaN/GaN MQW structures (a) & (b) porous InGaN/GaN, Sample B (c) Reference InGaN/GaN nanorods, Sample C (d) & (e) porous InGaN/GaN nanorods, Sample D

The nanorod samples are shown in Figure 6-11 (c)-(e). The nanorods have a diameter of 200 nm and a density of 10^8 cm^{-2}. After the nanorods are PEC etched, the SEM only indicates a partial etching of the nanorods, however the base of the sample is quite severely etched. As with the planar device and observed in the nanorods in Chapter 5, the quantum wells in the nanorods are partially etched. The variation in etch is due to the migration of

the carriers within the nanorod and planar structure resulting in the oxidation occurring at the QW and *n*-GaN.

6.5.3 Solar Hydrogen Performance

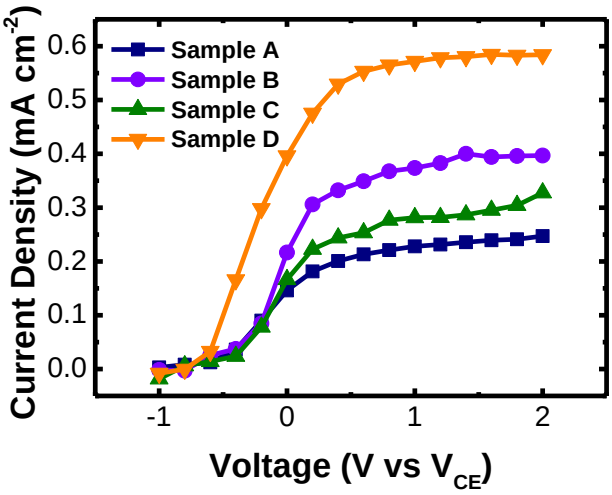

Figure 6-14 – Photocurrent measurements as a function of bias for InGaN/GaN MQW samples in 1M HCl and 1 sun illumination

The performances of the InGaN/GaN devices were investigated in a 1 M HCl solution and 1 sun illumination (Figure 6-12). As observed with previous devices, the fabrication of the nanorod structure leads to an increase in the photocurrent of the device in comparison to the as-grown device. The nanorod structure results in a photocurrent increase of 22 % after a bias is applied. The porous structure however causes a significantly greater change in photocurrent in both the planar and nanorod porous devices. As visible from the SEM (Figure 6-11) the porous device exposes a significantly larger area to the electrolyte resulting in the remarkable increase in photocurrent observed from Sample B and Sample D. Device performance increases from 0.18 % for the as-grown to 0.26 % and 0.48 % for Sample B and D respectively.

Hydrogen Measurements

Assessment of the Sample A and B for hydrogen performance was conducted under standard conditions (Figure 6-13). Theoretical and measured values for the planar and porous sample illustrate a high faradic efficiency with a strong agreement between the measurements. As expected based on the photocurrent measurements the porous sample produces a

significantly higher volume of hydrogen than the planar device. Hydrogen volumes for each sample are 0.25 ml hour^{-1} and 0.7 ml hour^{-1} for the reference and nanoporous samples respectively, over a two fold increase in production. This increase is due to the improved device efficiency and the better adsorption and desorption properties of the porous structure.

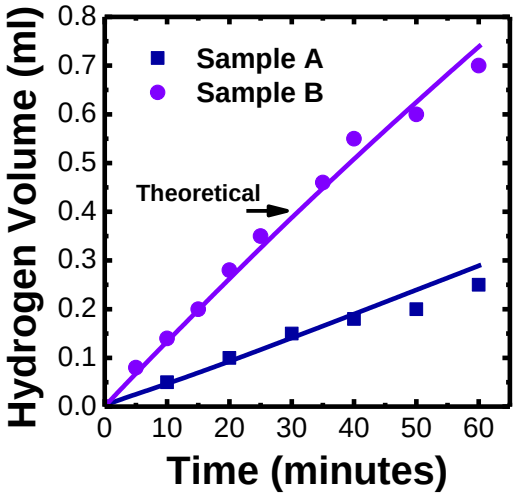

Figure 6-15 – Hydrogen generation measurements of reference InGaN/GaN sample (A) and porous InGaN/GaN sample (B) in 1 M HCl at 0.8 V and 500 mW cm^{-2} Xe lamp illumination. Lines indicate theorectical maximum.

Incident Photon Conversion Efficiency

IPCE measurements under standard conditions for the four samples are presented in Figure 6-14. Compared to the *n*-GaN data in Figure 6-9, as a result of the quantum wells the absorption of the device is extended to 440 nm with the peak efficiency of 11.9 % around the GaN band edge of 358 nm. Fabrication of the nanorod structure enhances the emission across all wavelengths with a peak of 42 % at 356 nm. The nanorod structure allows for a better absorption of light within the quantum wells and enhances the extraction of carriers due to the improved contact with the electrolyte. Comparatively, the porous devices, B and D, have a better efficiency within the GaN, with peak performance at the band edge of 46.6 % and 56.5 % respectively. However, due to the etching of the InGaN quantum wells, the efficiency at extended wavelengths is reduced when compared to the unetched counterparts. This is as a result of the removal of areas with high indium contents observed in other samples.[52]

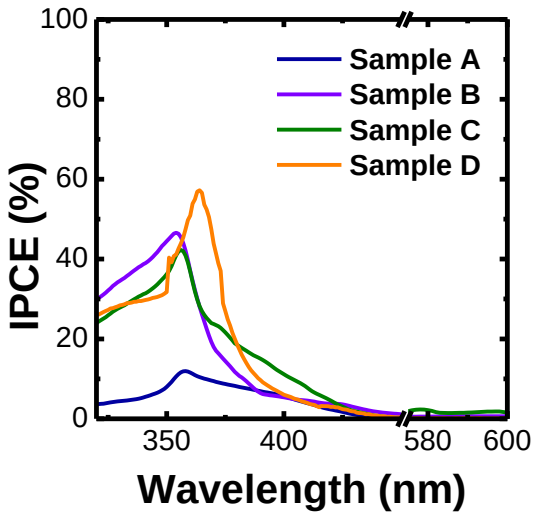

Figure 6-16 – Incident Photon Conversion Efficiency of InGaN/GaN reference Samples A and C and porous InGaN/GaN devices Samples B and D

6.5.4 Summary

As with the GaN samples, porous structures have been fabricated via a PEC etch on InGaN/GaN wafers. As a result of the increased separation of the charge carriers and greater surface area the photocurrent of the device is enhanced. The novel structure also increases the hydrogen generation rate of the device. Optimisation of the fabrication conditions could lead to further improvements in the performance of the device. The minority carrier diffusion length of indium gallium nitride can be as small as 30 nm. If the pore structure of the MQW device can be optimised to allow for maximum diffusion of carriers, recombination can be reduced enhancing the performance of the device. Furthermore, specific control of the etch needs to be conducted to minimise the loss of the indium in the quantum wells and the reduction in IPCE at longer wavelengths visible in these samples.

6.6 Conclusions

Utilising a simple photoelectrochemical etch, porous devices have been fabricated on III-nitride devices. Control over the etch can be achieved by altering the concentration and voltage during the etch. Porous nanostructures of GaN based devices have also been fabricated for the first time resulting to an increase in the solar hydrogen performance of the devices. IPCE measurements also show increases in the fabricated porous

structures with quantum well structures extending the optical absorption compared to GaN. The use of nanostructures enhances the absorption of the quantum wells increasing the potential performance of devices with higher indium content quantum wells. Furthermore, the addition of NiO on the porous samples has also been demonstrated as a potential solution for further enhancements in photocurrent and as a preventative measure to prolong the life of the device.

Bibliography

[1] V. Kochergin and H. Foll, *Porous Semiconductors: Optical Properties and Applications*, Illustrate (Springer-Verlag, London, UK, 2009), p. 216.

[2] E.B. Hensley, *J. Appl. Phys.* **23**, 1122 (1952).

[3] H. Föll, J. Carstensen, and S. Frey, *J. Nanomater.* **2006**, 1 (2006).

[4] K. Sayama, A. Nomura, T. Arai, T. Sugita, R. Abe, M. Yanagida, T. Oi, Y. Iwasaki, Y. Abe, and H. Sugihara, *J. Phys. Chem. B* **110**, 11352 (2006).

[5] Y. Ling, G. Wang, D. a Wheeler, J.Z. Zhang, and Y. Li, *Nano Lett.* **11**, 2119 (2011).

[6] M. Sathish, B. Viswanathan, and R. Viswanath, *Int. J. Hydrogen Energy* **31**, 891 (2006).

[7] Y.H. Ng, A. Iwase, A. Kudo, and R. Amal, *J. Phys. Chem. Lett.* **1**, 2607 (2010).

[8] P. Hartmann, D.-K. Lee, B.M. Smarsly, and J. Janek, *ACS Nano* **4**, 3147 (2010).

[9] B.D. Alexander, P.J. Kulesza, I. Rutkowska, R. Solarska, and J. Augustynski, *J. Mater. Chem.* **18**, 2298 (2008).

[10] J. Brillet, M. Grätzel, and K. Sivula, *Nano Lett.* **10**, 4155 (2010).

[11] H.M. Chen, C.K. Chen, R.-S. Liu, L. Zhang, J. Zhang, and D.P. Wilkinson, *Chem. Soc. Rev.* **41**, 5654 (2012).

[12] J. Zhu and M. Zäch, *Curr. Opin. Colloid Interface Sci.* **14**, 260 (2009).

[13] Y. Lin, G. Yuan, R. Liu, S. Zhou, S.W. Sheehan, and D. Wang, *Chem. Phys. Lett.* **507**, 209 (2011).

[14] H. Föll, S. Langa, J. Carstensen, M. Christophersen, and I.M. Tiginyanu, *Adv. Mater.* **15**, 183 (2003).

[15] S. Chattopadhyay, A. Ganguly, K.-H. Chen, and L.-C. Chen, *Crit. Rev. Solid State Mater. Sci.* **34**, 224 (2009).

[16] D. Zhuang and J.H. Edgar, *Mater. Sci. Eng. R Reports* **48**, 1 (2005).

[17] C. Youtsey, I. Adesida, and G. Bulman, *Electron. Lett.* **33**, 245 (1997).

[18] J.E. Borton, C. Cai, M.I. Nathan, P. Chow, J.M. Van Hove, A. Wowchak, and H. Morkoç, *Appl. Phys. Lett.* **77**, 1227 (2000).

[19] P. Visconti, K.M. Jones, M. a. Reshchikov, R. Cingolani, H. Morkoc, and R.J. Molnar, *Appl. Phys. Lett.* **77**, 3532 (2000).

[20] M. Mynbaeva and D. V. Tsvetkov, *Institue Phys. Conf. Ser.* **155**, 365 (1997).

[21] M. Mynbaeva, a. Titkov, a. Kryganovskii, V. Ratnikov, K. Mynbaev, H. Huhtinen, R. Laiho, and V. Dmitriev, *Appl. Phys. Lett.* **76**, 1113 (2000).

[22] I.M. Huygens, K. Strubbe, and W.P. Gomes, *J. Electrochem. Soc.* **147**, 1797 (2000).

[23] X. Li, Y.-W. Kim, P.W. Bohn, and I. Adesida, *Appl. Phys. Lett.* **80**, 980 (2002).

[24] F.K. Yam, Z. Hassan, L.S. Chuah, and Y.P. Ali, *Appl. Surf. Sci.* **253**, 7429 (2007).

[25] K. Al-Heuseen, M.R. Hashim, and N.K. Ali, *Appl. Surf. Sci.* **257**, 6197 (2011).

[26] H. Hartono, C.B. Soh, S.J. Chua, and E. a. Fitzgerald, *Phys. Stat. Sol (B)* **244**, 1793 (2007).

[27] S.F. Cheah, S.C. Lee, S.S. Ng, F.K. Yam, H. Abu Hassan, and Z. Hassan, *Appl. Phys. Lett.* **102**, 101601 (2013).

[28] C. Youtsey, G. Bulman, and I. Adesida, *J. Electron. Mater.* **27**, 282 (1998).

[29] C. Youtsey, I. Adesida, and G. Bulman, *Appl. Phys. Lett.* **71**, 2151 (1997).

[30] C. Youtsey, I. Adesida, L.T. Romano, and G. Bulman, *Appl. Phys. Lett.* **72**, 560 (1998).

[31] C. Youtsey, L.T. Romano, and I. Adesida, *Appl. Phys. Lett.* **73**, 797 (1998).

[32] R. Radzali, N. Zainal, F.K. Yam, and Z. Hassan, *Mater. Sci. Semicond. Process.* **16**, 2051 (2013).

[33] S.Y. Bae, H.W. Seo, J. Park, H. Yang, and B. Kim, *Chem. Phys. Lett.* **376**, 445 (2003).

[34] C.B. Soh, C.B. Tay, R.J.N. Tan, A.P. Vajpeyi, I.P. Seetoh, K.K. Ansah-Antwi, and S.J. Chua, *J. Phys. D. Appl. Phys.* **46**, 365102 (2013).

[35] M. Ali, O. Svensk, L. Riuttanen, M. Kruse, S. Suihkonen, A.E. Romanov, P.T. Törmä, M. Sopanen, H. Lipsanen, M.A. Odnoblyudov, and V.E. Bougrov, *Semicond. Sci. Technol.* **27**, 082002 (2012).

[36] H.-W. Huang, J.T. Chu, C.C. Kao, T.H. Hseuh, T.C. Lu, H.C. Kuo, S.C. Wang, and C.C. Yu, *Nanotechnology* **16**, 1844 (2005).

[37] C.-F. Lin, J.-H. Zheng, Z.-J. Yang, J.-J. Dai, D.-Y. Lin, C.-Y. Chang, Z.-X. Lai, and C.S. Hong, *Appl. Phys. Lett.* **88**, 083121 (2006).

[38] K. Kim, J. Choi, T.S. Bae, M. Jung, and D.H. Woo, *Jpn. J. Appl. Phys.* **46**, 6682 (2007).

[39] A. Ramizy, Z. Hassan, and K. Omar, *Sensors Actuators B Chem.* **155**, 699 (2011).

[40] F.K. Yam, Z. Hassan, and A.Y. Hudeish, *Thin Solid Films* **515**, 7337 (2007).

[41] K. Al-Heuseen and M.R. Hashim, *Sensors Actuators B Chem.* **163**, 159 (2012).

[42] C.K. Inoki, T.S. Kuan, C.D. Lee, A. Sagar, R.M. Feenstra, D.D. Koleske, D.J. Díaz, P.W. Bohn, and I. Adesida, *J. Electron. Mater.* **32**, 855 (2003).

[43] R.S.Q. Fareed, V. Adivarahan, C.Q. Chen, S. Rai, E. Kuokstis, J.W. Yang, M.A. Khan, J. Caissie, and R.J. Molnar, *Appl. Phys. Lett.* **84**, 696 (2004).

[44] A.P. Vajpeyi, S. Tripathy, S.J. Chua, and E. a. Fitzgerald, *Phys. E Low-Dimensional Syst. Nanostructures* **28**, 141 (2005).

[45] J. a. Bardwell, J.B. Webb, H. Tang, J. Fraser, and S. Moisa, *J. Appl. Phys.* **89**, 4142 (2001).

[46] J.L. Weyher, L. Macht, F.D. Tichelaar, H.W. Zandbergen, P.R. Hageman, and P.K. Larsen, *Mater. Sci. Eng. B* **91-92**, 280 (2002).

[47] H.-Y. Lee, X.-Y. Huang, and C.-T. Lee, *J. Electrochem. Soc.* **155**, H707 (2008).

[48] X.Y. Guo, T.L. Williamson, and P.W. Bohn, *Solid State Commun.* **140**, 159 (2006).

[49] S.-W. Ryu, Y. Zhang, B. Leung, C. Yerino, and J. Han, *Semicond. Sci. Technol.* **27**, 015014 (2012).

[50] J.L. Weyher, F.D. Tichelaar, H.W. Zandbergen, L. Macht, and P.R. Hageman, *J. Appl. Phys.* **90**, 6105 (2001).

[51] A.M. Basilio, Y.-K. Hsu, W.-H. Tu, C.-H. Yen, G.-M. Hsu, O. Chyan, Y. Chyan, J.-S. Hwang, Y.-T. Chen, L.-C. Chen, and K.-H. Chen, *J. Mater. Chem.* **20**, 8118 (2010).

[52] M. Li, W. Luo, B. Liu, X. Zhao, Z. Li, D. Chen, T. Yu, Z. Xie, R. Zhang, and Z. Zou, *Appl. Phys. Lett.* **99**, 112108 (2011).

[53] F.K. Yam, Z. Hassan, and S.S. Ng, *Thin Solid Films* **515**, 3469 (2007).

[54] D.G. Zhao, S.J. Xu, M.H. Xie, S.Y. Tong, and H. Yang, *Appl. Phys. Lett.* **83**, 677 (2003).

[55] K. Al-heuseen, M.R. Hashim, and N.K. Ali, *Phys. B Condens. Matter* **405**, 3176 (2010).

[56] W.-H. Tu, Y.-K. Hsu, C.-H. Yen, C.-I. Wu, J.-S. Hwang, L.-C. Chen, and K.-H. Chen, *Electrochem. Commun.* **13**, 530 (2011).

[57] B. AlOtaibi, M. Harati, S. Fan, S. Zhao, H.P.T. Nguyen, M.G. Kibria, and Z. Mi, *Nanotechnology* **24**, 175401 (2013).

[58] S.H. Abud, Z. Hassan, and F.K. Yam, *Int. J. Electrochem. Sci.* **7**, 10038 (2012).

[59] S.H. Abud, Z. Hassan, and F.K. Yam, *Mater. Lett.* **107**, 367 (2013).

[60] M. Godlewski, E. Łusakowska, E.. Goldys, M.. Phillips, T. Böttcher, S. Figge, D. Hommel, P. Prystawko, M. Leszczynski, I. Grzegory, and S. Porowski, *Appl. Surf. Sci.* **223**, 294 (2004).

[61] Q. Wang, J. Bai, Y.P. Gong, and T. Wang, *J. Phys. D. Appl. Phys.* **44**, 395102 (2011).

[62] J. Bai, Q. Wang, and T. Wang, *Phys. Stat. Sol (A)* **209**, 477 (2012).

Chapter 7

Conclusion

The fabrication of III-nitrides for solar hydrogen production is an area of growing interest. In the previous chapters I have undertaken a progressive approach to create novel nanostructures of GaN and InGaN/GaN wafers to further enhance and improve upon the research surrounding this topic.

7.1 Overview

The effects of climate change are being felt globally and the restrictions on governments and industries to curb carbon emissions means that green technologies are required. The use of hydrogen as a fuel source and fuel store is not new, however current production methods are unsatisfactory if the positive benefits of hydrogen as a clean fuel is to be realised. Solar production of hydrogen is a viable technology to produce the vast quantities of hydrogen that will be required if wide scale change is to occur.[1] Current material systems do not achieve the required lifetime or efficiency required to achieve commercialisation. For effective water splitting, the material is required to have specific properties, including the band gap, band positions and stability under operating conditions. III-nitride materials have the potential to achieve all three due to the tuneable band gap of the alloys, the correct conduction and valence band positions and a strong

resistance to corrosion in chemical solutions. Despite this, prior to the start of this research, the number of studies on III-nitride materials for photoelectrochemical water splitting were limited.

The focus of previous research was mainly on as-grown planar materials or intensively grown nanostructures limiting their practical applicability. Over the course of this research, there has been an increased focus on the possibility of using III-nitrides for water splitting and other photoelectrochemical reactions. The aim of this thesis was to develop novel approaches to the fabrication of III-nitride devices for solar hydrogen production to increase the efficiency and overall performance of the material. Throughout the previous chapters, examples on how this can be achieved have been demonstrated though novel techniques previously unused within the III-nitride material class for water splitting applications.

Chapter 4 demonstrated the fabrication of nanorods via the use of a simple post growth fabrication technique which resulted in a significant enhancement in photocurrent and hydrogen production. This was the first time a nanorod structure had been fabricated from an MOCVD grown wafer and investigated for its potential in water splitting. The method was demonstrated to work with GaN and InGaN materials with enhancement factors up to 6 achieved. This is due to the increased surface area obtained through the creation of a nanorod array as well as reduced carrier recombination due to the decrease in required path lengths. Optimisation of the fabrication method has resulted in a high level of control over the nanorods, creating structures that allow for the diffusion lengths of the electrons and holes within the material. Due to the differences in diffusion lengths of the III-nitride materials, the ability to control the nanorod size effectively is important to achieve the optimum results for each alloy utilised. Measurements of hydrogen evolution of the nanorod array also validated the improved device performance with a strong faradaic performance and significant increase over the reference planar device.

Realisation into the potential for increased corrosion of the nanorod device due to the device structure prompted the research discussed in Chapter 5. Device longevity is essential for it to be cost effective and commercial viable. The use of cocatalysts is widespread in the desire to achieve high rates of hydrogen evolution however the work on GaN was limited. NiO nanoparticles had been utilised on planar devices, however the mechanism and understanding behind their positive effect was not well understood. Through the deposition of NiO nanoparticles onto the nanorod array structures that had been developed in Chapter 4 a significant enhancement in their lifetime and photocurrent has been achieved. Further to this, the investigation into the understanding of process in regards to reaction sites and band positions has added to the previous research and knowledge of the community. The enhancement in photocurrent is attributed to the conduction and valence band positions of the NiO. Due to their complementary position compared to GaN and III-nitride materials the separation of photogenerated carriers is enhanced. The higher conduction band of NiO prevents electron flow to the surface while the valence band position promotes hole flow. As a result, recombination within the bulk material is reduced increasing photocurrent. The improvement in device lifetime is a result of the hole migration. Due to the corrosion of GaN through the reaction of holes at the surface reducing the number of surface reactions prevents the rate of corrosion of the electrode. The NiO acts as the reaction site for oxygen evolution preventing photocorrosion.

Identification of photocorrosion of GaN resulted in the work conducted in Chapter 6. Nanostructures had already been identified as a positive technique to enhance the performance of a device and therefore the creation of a porous structure could further improve this. Previous research had identified the use of etching techniques and surface treatments to improve photocurrents however photoelectrochemical etching of GaN had only yielded detrimental effects. The use of a potassium hydroxide solution, voltage and illumination source have been shown to create a porous structure in the GaN and InGaN/GaN materials. By varying the conditions of

the technique a level of control in regards to pore size and etch depth has been achieved. An enhancement in photocurrent was observed for all porous devices which contradicted previous research. The chemical treatment created a network of pores that increased the total surface area of the device as well as reducing the distances required for minority diffusion. The use of the porous structure demonstrated similar benefits to that of the nanorod array due to the properties of nanostructured semiconductors. Optimum fabrication conditions for porous GaN were achieved and investigated through SEM and photocurrent measurements. Alongside the development of porous GaN, porous InGaN/GaN quantum well devices were fabricated and studied. Prior to this work, the use of porous InGaN/GaN had not been identified as a potential option for water splitting.

Further to this, the individual techniques developed during this thesis were combined to create a highly ordered nanorod array with porous cavities and porous devices with NiO nanoparticles. Control over both techniques resulted in further enhancements to the photocurrent and hydrogen evolution. The addition of NiO nanoparticles to the porous devices also resulted in a similar enhancement and improvement in corrosion prevention demonstrated with the nanorod array. By combining each of the techniques developed in this research an enhancement in photocurrent, hydrogen production and device lifetime has been achieved. These three areas are significant requirements for the development of high quality electrodes for water splitting.

7.2 Future Research

The focus of this thesis has been on GaN and InGaN/GaN quantum well devices. Enhancements in performance through the fabrication of novel nanostructures has been achieved however there is the potential for further work to be conducted to attain the high photocurrents required for commercial application. Due to the nature of GaN and InGaN, the techniques utilised in this work can potentially be applied to the entire alloy range of the III-nitride materials.

7.2.1 InGaN bulk films

The incorporation of indium into gallium nitride is essential if the band gap is to be reduced to the required level of 1.8 eV.[2] Although the use of quantum wells allows the growth of high indium content films there are potential issues. In order to achieve sufficient absorption of visible radiation a film thickness of at least 100 nm is required. Typical quantum wells are <10 nm and therefore the majority of input energy will be lost. The use of bulk InGaN wafers can increase the amount of solar radiation available significantly from the 2 % of GaN. Bulk InGaN films and MBE grown InGaN nanostructures have been investigated,[3,4] however there are currently no studies in which the fabrication techniques developed in this thesis are utilised to create InGaN nanostructures from MOCVD grown material. Due to the extensive development of the technique on GaN, implementation into a bulk InGaN should be easily obtainable which could potentially result in device efficiencies higher than currently reported.

7.2.2 Intermediate Bands

Another potential opportunity to expand the absorption of GaN based devices is through the incorporation of intermediate bands.[5] Some preliminary work on manganese doped GaN on top of *n*-type GaN have identified the potential of intermediate bands in III-nitrides for water splitting.[6] The principle behind intermediate bands is the addition of a band within the main band of the bulk material. The addition of this band allows for absorption of sub band gap photons resulting in the potential for two photon absorption. This could be specifically useful for GaN in which the absorption of visible light is the main factor contributing to the lower performance. Due to ability to create semiconductors with band gaps varying from 0.7 eV through to 3.4 eV by alloying different types of indium with GaN, it is possible to create a complementary system with of the same material type. This means that the requirements of crystal matching to prevent low quality growth is minimised. If multiple intermediate bands are located within the GaN band it is possible that the absorption can be shifted significantly from the UV through to the infrared. Combining intermediate bands with the

nanostructures could significantly enhance the efficiency of the photoelectrode.

7.2.3 Device Properties

The fabrication of the device is only one aspect that plays a role in the overall performance. The extraction of carriers from the device is essential if high photocurrents are to be achieved. One method in which this could be achieved is through the optimisation of the ohmic contact on the device. Through the use of multiple finger contacts as opposed to a single contact improvements in photocurrents have been observed for both *n*- & *p*-type GaN.[7,8] The fabrication of these structures is relatively straight forward for planar devices however, due to the use of nanostructured GaN and InGaN, increasing the complexity of the contact can cause additional problems. Therefore, optimisation of the fabrication of more complex contacts for increased majority carrier extraction is required for the nanostructured devices fabricated in this thesis.

7.2.4 Summary

The potential for the furthering of this research is relatively vast. Due to the early nature of the research on III-nitrides for water splitting there is the opportunity to develop the variety of approaches discussed. Each technique could potentially increase the efficiency of the device and through the implementation of the fabrication techniques to create nanostructures. Due to the nature of the fabrication methods, the main requirement for improvement in GaN based devices is through the optimisation of the growth techniques to achieve high quality wafers. If this is achieved, the implementation of the techniques developed in this research can be easily applied leading to substantial gains in device efficiencies for implementation in green technology.

Bibliography

[1] M. Grätzel, *Nature* **414**, 338 (2001).

[2] P.G. Moses and C.G. Van de Walle, *Appl. Phys. Lett.* **96**, 021908 (2010).

[3] K. Aryal, B.N. Pantha, J. Li, J.Y. Lin, and H.X. Jiang, *Appl. Phys. Lett.* **96**, 052110 (2010).

[4] W. Luo, B. Liu, Z. Li, Z. Xie, D. Chen, Z. Zou, and R. Zhang, *Appl. Phys. Lett.* **92**, 262110 (2008).

[5] L. Cuadra, a Martí, and a Luque, *Thin Solid Films* **451-452**, 593 (2004).

[6] S.-Y. Liu, J.K. Sheu, Y.-C. Lin, S.J. Tu, F.W. Huang, M.L. Lee, and W.C. Lai, *Opt. Express* **20 Suppl 5**, A678 (2012).

[7] S.-Y. Liu, J.K. Sheu, M.L. Lee, Y.-C. Lin, S.J. Tu, F.W. Huang, and W.C. Lai, *Opt. Express* **20 Suppl 2**, A190 (2012).

[8] S.-Y. Liu, J.K. Sheu, C.-K. Tseng, J.-C. Ye, K.H. Chang, M.L. Lee, and W.C. Lai, *J. Electrochem. Soc.* **157**, B266 (2010).